Jets in proton-proton, proton-lead and lead-lead collisions at the CERN Large Hadron Collider

By

SUMIT KUMAR SAHA

PHYS04201504008

Variable Energy Cyclotron Centre, Kolkata

A thesis submitted to

The Board of Studies in Physical Sciences

In partial fulfillment of requirements

For the Degree of

DOCTOR OF PHILOSOPHY

of

HOMI BHABHA NATIONAL INSTITUTE

February, 2022

Homi Bhabha National Institute

Recommendations of the Viva Voce Committee

As members of the Viva Voce Committee, we certify that we have read the dissertation prepared by Sumit Kumar Saha entitled "Jets in proton-proton, proton-lead and lead-lead collisions at the CERN Large Hadron Collider" and recommend that it may be accepted as fulfilling the thesis requirement for the award of Degree of Doctor of Philosophy.

Chairman–(Prof. Jane Alam)		Date:	8.2.2022
Guide/Convener–(Prof. Subhasis Chattopadhyay)		Date:	8.2.2022
Examiner–(Prof. Manas Maity)		Date:	8.2.2022
Member 1–(Prof. Anand Dubey)		Date:	8.2.2022
Member 2–(Prof. Sourav Sarkar)		Date:	8.2.2022
Member 3–(Prof. Munshi Golam Mustafa)		Date:	8.2.2022

Final approval and acceptance of this thesis is contingent upon the candidate's submission of the final copies of the thesis to HBNI.

I hereby certify that I/we have read this thesis prepared under my direction and recommend that it may be accepted as fulfilling the thesis requirement.

Date: 8.2.2022

Guide 8/2/2022

Place: VECC (Dr. Subhasis Chattopadhyay)

[1] This page is to be included only for final submission after successful completion of viva voce.

STATEMENT BY AUTHOR

This dissertation has been submitted in partial fulfillment of requirements for an advanced degree at Homi Bhabha National Institute (HBNI) and is deposited in the Library to be made available to borrowers under rules of the HBNI.

Brief quotations from this dissertation are allowable without special permission, provided that accurate acknowledgement of source is made. Requests for permission for extended quotation from or reproduction of this manuscript in whole or in part may be granted by the Competent Authority of HBNI when in his or her judgment the proposed use of the material is in the interests of scholarship. In all other instances, however, permission must be obtained from the author.

Sumit Kumar Saha

DECLARATION

I, hereby declare that the investigation presented in the thesis has been carried out by me. The work is original and has not been submitted earlier as a whole or in part for a degree / diploma at this or any other Institution / University.

Sumit Kumar Saha

List of Publications

List of published and communicated journals

1. S. K. Saha, D. Sarkar, S. Chattopadhyay, A. I. Sheikh and S. K. Prasad, Nucl. Phys. A **1006** (2021), 122064 doi:10.1016/j.nuclphysa.2020.122064 [arXiv:2101.02685 [hep-ph]].

2. S. Thakur, S. K. Saha, P. Dasgupta, R. Chatterjee and S. Chattopadhyay, Nucl. Phys. A **1014** (2021), 122263 doi:10.1016/j.nuclphysa.2021.122263 [arXiv:2101.09998 [nucl-th]].

3. S. Thakur, S. K. Saha, S. N. Alam, R. Chatterjee and S. Chattopadhyay, [arXiv:2109.07225 [nucl-th]] (Accepted for publication in EPJA).

4. S. Muhuri, S. Mukhopadhyay, V. B. Chandratre, T. K. Nayak, S. K. Saha, S. Thakur, R. N. Singaraju, J. Saini, A. van den Brink and T. Chujo, *et al.* JINST **15** (2020) no.03, P03015 doi:10.1088/1748-0221/15/03/P03015 [arXiv:1911.00743 [physics.ins-det]].

5. Measurements of the groomed and ungroomed jet angularities in pp collisions at 5.02 TeV ([arXiv:2107.11303 [nucl-ex]].)

List of conferences and symposia

1. S. K. Saha, S. Basu, S. P. Adhya, R. Biswas, S. Das, T. K. Nayak and S. K. Prasad, DAE Symp. Nucl. Phys. **61** (2016), 850-851

2. S. Muhuri, S. Mukhopadhay, S. K. Saha, S. Thakur, V. B. Chandratre, S. A. Khan, T. K. Nayak, J. Saini, R. N. Singaraju and M. Sukhwani, DAE Symp. Nucl. Phys. **61** (2016), 748-749

3. Correlation between initial spatial anisotropy and final momentum anisotropies in relativistic heavy ion collisions, PoS(LHCP2021)204 (LHCP 2021, Proceedings)

4. Study of medium modified jet shape observables in Pb-Pb collisions at $\sqrt{s_{NN}}$=2.76 TeV using EPOS and JEWEL event generators (ISMD 2021)

5. S. Thakur, S. K. Saha, Sk. N. Alam, R. Chatterjee and S. Chattopadhyay, Proceedings of the DAE Symp. on Nucl. Phys. 65 (2021)

Sumit Kumar Saha

Dedicated to my parents and my teachers

ACKNOWLEDGEMENTS

I would like to thank my supervisor Dr. Subhasis Chattopadhyay for his support and encouragement. I am thankful to Leticia Cunqueiro Mendez the convenor of the ALICE Physics Working Group of Jets for her constant help in my analysis work. They helped me in every step whenever I faced any problem. I thank my senior Dr. Noor Alam, Dr. Subikash Choudhury, Dr. Debojit Sarkar and Dr. Sumit Basu for their help and useful discussions. I am thankful to my senior Dr. Arghya Chatterjee and Dr. Rajendra Nath Patra for their helpful discussions, suggestions, support and encouragement. I am very much thankful to Dr. Sidharth Kumar Prasad and Rathijit Biswas for their constant help and suggestions and I am really very fortunate to have worked with them. I am grateful to VECC grid for helping me in my work. I specially thank Mr. Abhisek Seal and Mr. Prasun Singha Roy for their constant help in my work. I would like to thank Prof. Tapan K. Nayak for useful physics discussions and suggestions. I thank Dr. Tilak Kumar Ghosh for motivating and helping students. I thank Dr. Jane Alam, Dr. Sourav Sarkar ,Dr. Zubayer Ahmed, Dr. Anand Kumar Dubey, Dr. Premomoy Ghosh for useful discussions. I also like to thank my doctoral committee members. I thank my seniors Dr. Nachiketa Sarkar, Dr. Ashik Ikbal, Dr. Samranjy Sadhu, my friends Shreyasi Acharya, Mitali Mondal, Soumen Nandi, Santanu Pathak, Mahfuzur Rahman, Sinjini Chandra and my juniors Dipen Paul,Vivek Kumar Sing, Sudipta Mohsat with whom I enjoyed a lot to work and spend many memorable moments. I also thank my school friends Rahul, Apu, Arnab, Rajib for motivating me to do research. Finally, I thank Sanchari and my parents for being the source of continuous, endless support, encouragement and inspiration over years and giving me motivation at every step.

Sumit Kumar Saha

Contents

Synopsis

0.1 Introduction

According to the Quantum ChromoDynamics (QCD), the theory of strong interaction, there are two important properties that partons posses known as asymptotic freedom and confinement[1]. As per the confinement property, in the limit of low momentum transfer or increase in the distance between the quarks, the strength of the interaction among the quarks becomes very high. As a consequence, free or isolated quarks cannot exist in nature. They are always found to be bound inside hadrons. On the other hand, the asymptotic freedom [2, 3] states that in the limit of high momentum transfer or high energy density, the interaction strength among the quarks becomes so weak that the quarks almost behave like free particles. They are no longer confined to hadrons. This deconfined state of quarks and gluons are called Quark Gluon Plasma known to prevail in the early universe about a micro-second after the Big Bang when the temperature was very high [4, 5]. The universe was then filled with a hot and dense soup of quark gluon plasma. At about 10^{-6} sec after the Big Bang, when the temperature of the expanding universe decreases, the quarks and gluons fragment to form hadrons and a transition from the phase of quark-gluon-plasma to hadronic matter happened. The transition, depicted by the diagram of baryonic chemical potential (μ_B) vs. temperature (T) commonly known as the phase diagram of the strongly interacting matter is expected to be of first order at low temperature $\sim 50MeV$ and high μ_B , whereas, at very

high temperature $\sim 150MeV$ and very low μ_B, the transition is a smooth crossover. The critical point is expected to lie at the junction between these two types of transitions. In the laboratory, the QGP state is formed by creating regions of high energy density ($> 1GeV/fm^3$) by colliding $Pb + Pb$ nuclei at Large Hadron Collider (LHC), CERN and $Au + Au$ nuclei at Relativistic Heavy Ion Collider (RHIC), BNL. ALICE at LHC-CERN and STAR, PHENIX at RHIC-BNL are the major experiments to study the formation & properties of the medium and its evolution. Results from the experiments have indicated the formation of a strongly coupled nearly perfect liquid in heavy ion collision. As the nuclei collide, they thermalize and form a hot thermalized medium of deconfined quarks and gluons which then expands, cools down and reaches a density and temperature where the partons get combined to form a hadron gas. After some time, the hadron fractions become fixed. This stage in the evolution process is called the chemical freeze-out [6]. As the medium expands further, the interactions between hadrons stop and hadrons reach the detectors freely with their final energies and momenta. This stage is called the thermal freeze-out.

Experimentally we cannot observe each stage separately, we observe only the final state observables from the the final state hadrons reaching the detector. Each stage of this evolution has some particular properties and some signals through which the states can be probed. Since the lifetime of QGP is of the order of 10^{-23} second, the signals of QGP are indirect. A nuclear collision is characterized by its centrality, number of produced particles, energy density and pressure of the formed state, the freeze-out temperature and volumes among others. The properties of the particles produced in the collisions provide insight on the production mechanism and the characteristics of the medium created. One of the first measurements in these experiments is the particle multiplicity at the mid-rapidity region which provides information on energy density, entropy and mechanism of particle production. The entropy produced in the early collision time, transforms into particle multiplicities later. Rapidity is the relativistic measure of velocity of a particle. The transverse

momentum spectra of charged particles and identified particles provide information about mean transverse momenta, temperature, radial flow and other observables [7]. The low p_T part of the spectrum exhibits an exponential behaviour having thermal origin, whereas, the high p_T region follows a power law distribution having contribution from the fragmentation of hard parton scattering [8]. The inverse slope of the low p_T spectra gives the effective temperature at freeze-out and the average radial flow velocity can also be obtained from p_T spectra.

One of the signatures of QGP formation is jet-quenching expressed by the Nuclear Modification factor R_{AA} that measures the energy loss of high p_T partons in the QGP medium that are produced at the initial stage of the collision. They are considered to be useful to probe the early stages of the collision as well as that of the entire medium evolution. R_{AA} measures the deviation of the yield in A-A collisions compared to the scaled p-p reference due to the presence of a medium.

Di-hadron correlation is another important observable for the evidence of medium formation. The hard partons fragment into a collimated shower of correlated particles in a conical volume called Jets [9]. If a pair of back to back jets carrying equal amount of energy called dijets is produced near the periphery of the fireball, one escapes directly losing lesser energy compared to the other one that traverses through the medium and loses a sufficient amount of energy by collisions with medium partons, or via gluon bremsstrahlung emission. Di-hadron correlation with high p_T trigger serves as an important evidence of the QGP medium measuring the suppression of the away side correlation peak which indicates the energy loss of the parton in the medium. Modification of the fragmentation functions of partons in heavy ion collision that measures the distribution of the final state hadrons from a hard process as a function of the fraction of parton's momentum carried away by hadron serves as another evidence of medium formation.

Jet-shapes or jet-substructures are among the new observables that probe the properties of the QGP medium. They help to understand the intra-jet broadening or collimation as a result of jet

quenching. The substructures are expected to be modified in heavy ion collisions at RHIC and LHC energies with respect to the pp collisions. Some of the variables representing the substructures are Angularity (g), Dispersion ($p_T D$), Lesub, jet differential shape ($\rho(r)$) [10, 6]. g increases if the jet is broadened by the medium and g decreases if the jet is collimated. $p_T D$ measures how hard or soft the fragmentation is. LeSub describes the hardest splitting and therefore it is not sensitive to the background.

Measurement of jets in proton-proton collisions allows to test pQCD and hadronization models. Also, these measurements provide the baseline for the heavy-ion studies like the modification in jet structures and production rates in heavy-ion collisions through the medium interaction.

0.2 Study of jet shapes in pp collisions at 5.02 TeV

In this thesis, the substructure of charged jet has been studied in p+p collision at $\sqrt{s_{NN}} = 5.02$ TeV with the ALICE experiment at CERN, Geneva. Charged particles of jets are measured using the Time Projection Chamber (TPC) and the Inner Tracking System (ITS). FastJet package [11, 12, 13, 14, 15] is used to use the final state particle to obtain the inital parton information i.e jet finding. $Anti - K_T$ algorithm is used to reconstruct jets with resolution parameter R=0.2, 0.4 and E-scheme. Minimum track p_T of 0.15 GeV/c and $|\eta|$ <0.9 are used as constituents cut and jet acceptance is considered as $|\eta| < 0.7$ for R=0.2 and $|\eta| < 0.5$ for R=0.4. Three jet shape observables i.e. Angularity (g), Dispersion ($p_T D$), LeSub have been studied in this analysis. The angularity that measures the radial energy profile of the jet, signifies whether jets are collimated or broadened. The dispersion tells how hard or soft the fragmentation is. LeSub describes the hardest splitting, therefore it should not be sensitive to the background [6, 10, 16].

For a conical jet, the resolution parameter in a jet finding algorithm represents the radius of a jet and it is defined by, $R = \sqrt{\Delta\phi^2 + \Delta\eta^2}$, where $\Delta\phi$ and $\Delta\eta$ are the distances of the particle from

the jet axis in ϕ and η. The most commonly used jet algorithm is anti-k_T that reconstructs conical jets and has been used in this analysis.

Raw distributions of jet shape variables have been studied for R=0.2 and R=0.4. At higher jet p_T, jets are collimated for $R = 0.2$. It is seen that when the jet radius is increased, jets are broadened for a particular jet p_T. To compare the measurements to theoretical calculations or other measurements, the results must be corrected for the fluctuations due to the finite detector resolution. Two dimensional Bayesian unfolding [17] has been used in an iterative way to remove the detector effects on the jet shape variables and to get the corrected observables. To unfold the shape variables, a 4D response matrix [16] has been constructed using PYTHIA. The correlation between the shapes at particle and detector level has been studied. After that, the jet shape resolution has also been obtained for the three observables. Then the unfolded solutions for different iterations are compared to the raw distribution. It is seen that the unfolding changes the shape significantly and solution converge above four iterations. The stability of unfolding is checked by refolding the solution back and checking its agreement with the raw distribution. To test the stability of the unfolding procedure, a closure test has also been performed where, the unfolding input is filled with Monte Carlo(MC) information. The MC which is used to fill the input is expected to be statistically independent from the sample that is used to fill the response (typically input contains 3% and response 97% of the MC sample). The performance is validated from the ratio of the unfolded solution to the true MC. The systematic errors are then estimated for different sources and added in quadrature. Finally, the fully corrected results are shown with model comparison.

0.3 Results

Fig. 1 shows the fully corrected jet shapes in p+p collision at $\sqrt{s}$ = 5.02 TeV for two resolution parameters R=0.2 and R=0.4. The angularity distribution gets broader for R=0.4 and the peak shifts towards higher value, whereas, the dispersion slightly shifts towards left for R=0.4 which indicates the jet-broadening at higher radius and the small radius jets are fragmented harder at particular jet p_t. The jet shapes for R=0.2 and R=0.4 are compared with PYTHIA8 [18] and the comparison along with the ratio is shown in Figure. Pythia is used for event generation in high-energy physics emphasizing on multiparticle production in collisions between elementary particles which means hard interactions in ep, pp and e^+e^- collision.

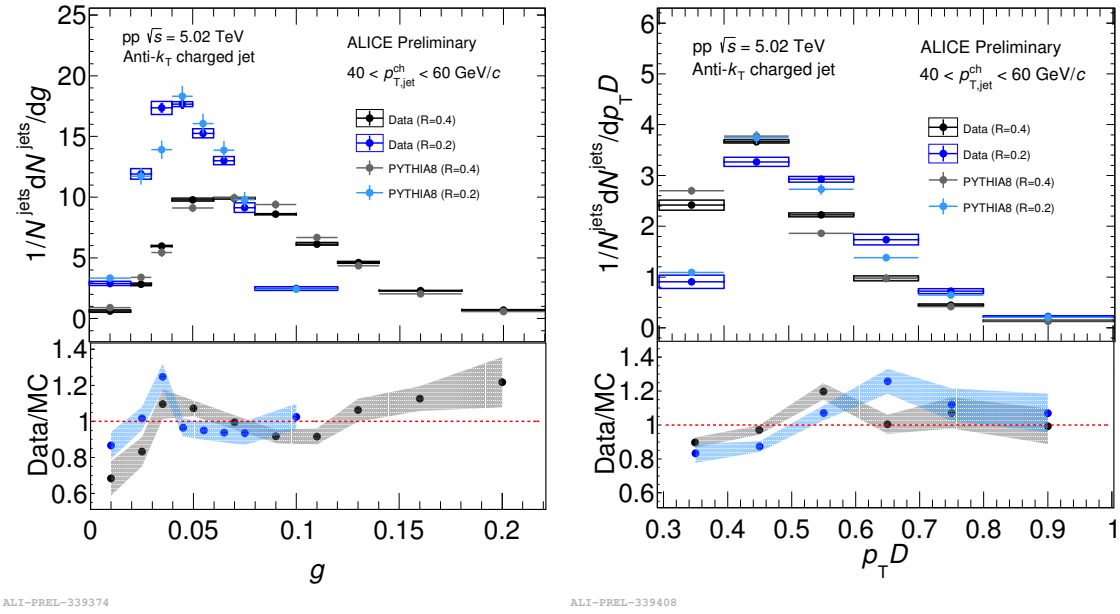

Figure 1: jet shape distributions in pp for R=0.2 and 0.4 in jet p_T 40-60 GeV/c and comparison with Pythia 8 model

0.4 A model study of medium modified jet shape observables in Pb-Pb collisions at $\sqrt{s_{NN}}$=2.76 TeV

As a part of the thesis, a study of the medium modified jet shape observables in Pb-Pb collisions at $\sqrt{s_{NN}}$=2.76 TeV using EPOS-3 [21, 22] and JEWEL [19, 20] event generators has been presented.

The jet-medium interaction in high energy heavy ion collisions is an important phenomena to characterize the hot and dense medium produced in such collisions. Medium-induced modifications to the substructure of inclusive charged jets indicates a redistribution of energy inside the jet cone and provides insight into the energy loss mechanisms of jets in the medium. We investigate the in-medium modification to the two jet shape observables i.e., the differential jet shape ($\rho(r)$) and the angularity (g) in the most central Pb-Pb collisions at 2.76 TeV using two commonly used event generators JEWEL (recoil OFF) and EPOS-3 in the jet-p_T range of 20-40 GeV/c.

JEWEL with recoil OFF has been used primarily as a reference system as that has been found to explain the global jet observables satisfactorily but lacks in jet-shape variables at the higher jet-radii. EPOS-3 that explains the bulk properties in such collisions quite well takes into account a hydrodynamically evolving bulk matter, jets and hard-soft interactions. A comparison between the results from these models shows that while JEWEL (recoil OFF) does not explain the distribution of lost energy at higher radii with respect to the jet-axis, EPOS-3 explains the effect quite well. However, in EPOS-3, the implemented partonic energy loss mechanism and secondary hard-soft interactions during hadronization and hadronic cascade phase are different from the conventional jet energy loss models. The current study can, therefore, provide important new insights on mechanisms regarding the modeling of the medium and hard-soft interactions in heavy ion collisions.

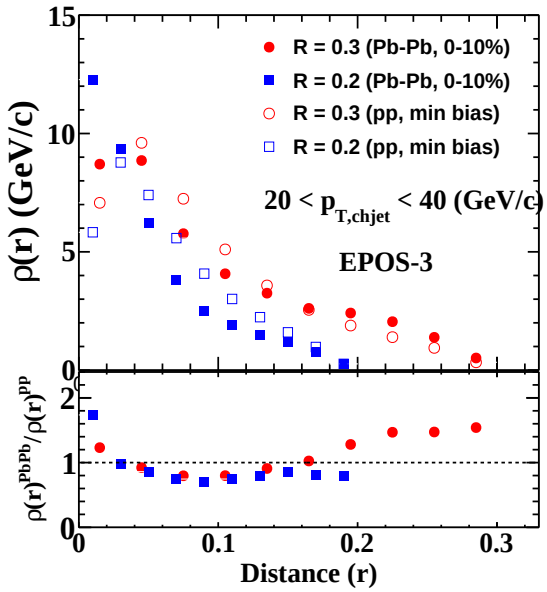

Figure 2: **Upper panel:** Differential jet shape $\rho(r)$ measured as a function of distance from the jet axis for inclusive charged jets in $20 < p_{T,chjet} < 40$ GeV/c with $R = 0.2$ and $R = 0.3$ in 0-10% central Pb-Pb collisions at $\sqrt{s_{NN}} = 2.76$ TeV using the EPOS-3 event generator and compared with the minimum bias pp results. **Lower panel:** The jet shape nuclear modification factor, quantified as $\rho(r)^{PbPb}/\rho(r)^{pp}$

Bibliography

[1] D. Gross, Asymptotic freedom and QCD: A historical perspective, Nucl.Phys.Proc.Suppl. 135 (2004) 193211.

[2] D. J. Gross and F. Wilczek, Phys. Rev. Lett. **30** (1973), 1343-1346 doi:10.1103/PhysRevLett.30.1343

[3] H. D. Politzer, Phys. Rev. Lett. **30** (1973), 1346-1349 doi:10.1103/PhysRevLett.30.1346

[4] P. Braun-Munzinger and J. Stachel, Nature **448**, 302 (2007). doi:10.1038/nature06080

[5] F. Karsch, Nucl. Phys. A **698** (2002), 199-208 doi:10.1016/S0375-9474(01)01365-3 [arXiv:hep-ph/0103314 [hep-ph]].

[6] M. Connors, C. Nattrass, R. Reed and S. Salur, Rev. Mod. Phys. **90** (2018), 025005 doi:10.1103/RevModPhys.90.025005 [arXiv:1705.01974 [nucl-ex]].

[7] N. Armesto et al., e-Print: arXiv:0711.0974.

[8] M. Kliemant, R. Sahoo, T. Schuster and R. Stock, Lect. Notes Phys. **785** (2010), 23-103 doi:10.1007/978-3-642-02286-9_2 [arXiv:0809.2482 [nucl-ex]].

[9] C. Adler *et al.* [STAR], Phys. Rev. Lett. **89** (2002), 202301 doi:10.1103/PhysRevLett.89.202301

[10] Cunqueiro, L. (ALICE) (2016),Proceedings, 25th Interna-tional Conference on Ultra-Relativistic Nucleus-NucleusCollisions (Quark Matter 2015): Kobe, Japan, September27-October 3, 2015, Nucl. Phys.A956, 593.

[11] Cacciari, M., J. Rojo, G. P. Salam, and G. Soyez (2011),Eur.Phys.J.C71, 1539.

[12] Cacciari, M., G. P. Salam, and G. Soyez (2008a), JHEP04,063.

[13] Cacciari, M., G. P. Salam, and G. Soyez (2008b), JHEP0804, 005.

[14] Cacciari, M., G. P. Salam, and G. Soyez (2012), Eur.Phys.J.C72, 1896.

[15] Salam, G. P. (2010), Eur.Phys.J.C67, 637.

[16] S. Acharya *et al.* [ALICE], JHEP **10** (2018), 139 doi:10.1007/JHEP10(2018)139 [arXiv:1807.06854 [nucl-ex]].

[17] D'Agostini, G. (1995), Nucl. Instrum. Meth.A362, 487.

[18] T. Sjostrand, S. Mrenna and P. Z. Skands, Comput. Phys. Commun. **178** (2008), 852-867 doi:10.1016/j.cpc.2008.01.036 [arXiv:0710.3820 [hep-ph]].

[19] K. C. Zapp, JEWEL 2.0.0: directions for use, Eur. Phys. J. C74 (2) (2014) 2762.

[20] Kunnawalkam Elayavalli, R. and Zapp, K.C. J. High Energ. Phys. (2017) 2017: 141. https://doi.org/10.1007/JHEP07(2017)141

[21] K. Werner, Iu. Karpenko, M. Bleicher, T. Pierog, S. Porteboeuf-Houssais Phys. Rev. C 85, 064907 (2012).

[22] K. Werner et al., Phys. Rev. C82 (2010) 044904.

List of Figures

List of Tables

Chapter 1

Introduction

The first set questions that came to our mind are "what is the basic building block of matter", "how is the universe created and evolve to the present condition?" Georges Lemaitres's Big Bang theory of universe was the first conceptual idea of the cosmological origin of the universe. According to the Big Bang theory, the Universe started from a point of infinitesimally small volume (point) with very high temperature and density called the singularity about 13.8 billion years ago. All the matters were compressed into a single point which subsequently exploded and then started expanding [1]. This is considered to be the beginning of space and time. In the early universe, immediately after the Big Bang when the temperature was extremely high [2], all the four forces were united to a single force according to the Grand Unification Theory. After $\sim 10^{-43}$ sec of Big Bang, the separation of the gravitational force occurs first, the strong force decoupled next and finally the electromagnetic and weak forces got separated after $\sim 10^{-11}$ sec after the Big Bang. The universe was so hot that the quarks and gluons, participants in the strong force, were free. At about 10^{-5} sec after the Big Bang, the universe was filled with a hot and dense soup of quarks and gluons called Quark-Gluon plasma (QGP). Collisions between particles were so energetic that it did not allow quarks to combine into hadrons. This stage is known as Quark Epoch. At about

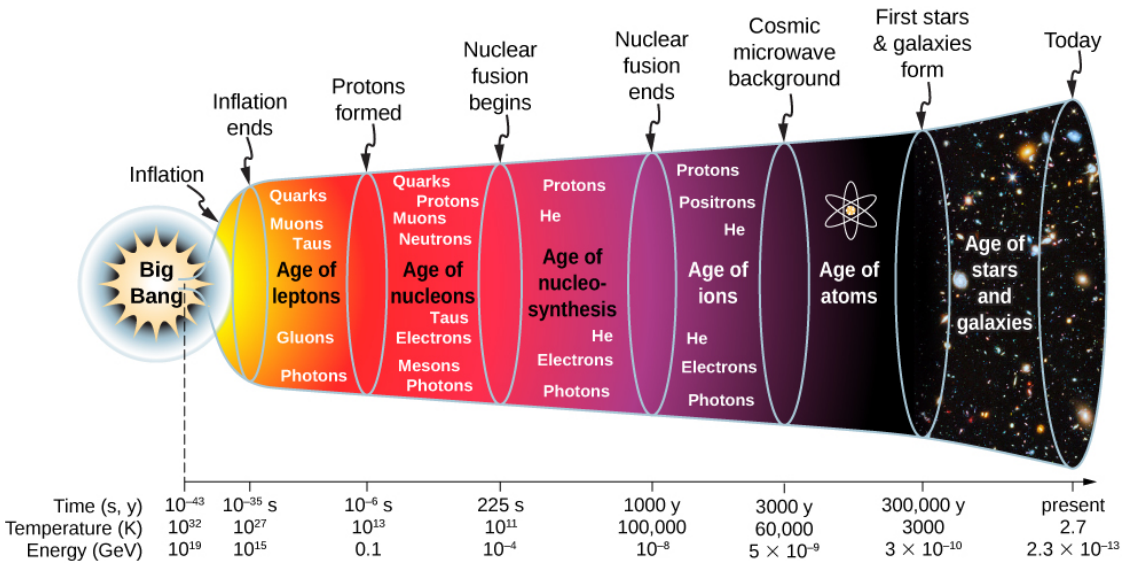

Figure 1.1: The Big Bang picture: creation and evolution of the Universe [3]

10^{-6} sec after the Big Bang when the temperature was about 0.2 GeV, Quark Epoch ended and a transition from the phase of quark-gluon-plasma to hadronic matter happened. This is known as Hadron Epoch. After that, protons and neutrons got combined to form nuclei. The atoms, molecules and the matter were formed subsequently. The different stages are depicted in Fig. 1.1. Deep inelastic scattering experiment suggested that the constituent particles of proton called partons can be probed under the condition of high momentum transfer. It was then thought that similar conditions like the microsecond old universe can be created in the laboratory by colliding two heavy nuclei at ultra relativistic energies [4]. This challenging task was successfully performed by establishing two powerful accelerators: The Relativistic Heavy Ion Collider (RHIC) at Brookhaven National Laboratory (BNL), New York and Large Hadron Collider (LHC) at the European Organization for Nuclear Research (CERN), Geneva. They accelerate charged particles at extremely high energy and make them collide to recreate the state of the matter that existed in the few microsecond old universe.

1.1 The Standard Model: fundamental particles and interactions

The Standard Model is a theoretical model describing the fundamental particles, their interactions and the force-carriers. Matters are made up of atoms and molecules and an atom consists of a nucleus containing protons and neutrons and electrons revolving around the nucleus. By 1932, the electrons, protons and neutrons were known as the elementary particles. In 1964, the existence of the subatomic particles known as quarks was proposed and in 1968, it was found in the Stanford Linear Accelerator Centre (SLAC) that neutrons and protons contain more fundamental particles known as quarks. Subsequent investigations led quarks to be classified as up (u), down (d), charm (c). strange (s), top (t) and bottom (b). The lepton group has electorn (e), electron neutino (ν_e), muon (μ), muon neutino (ν_μ), tau (τ) and tau neutrino (ν_τ). All the elementary particles have their corresponding anti-particles. The strongly interacting particles formed by the elementary particles are called hadrons and are divided into two groups: baryons and mesons. The baryons are made of three quarks and the mesons consist of quark and anti-quark pair. The quarks and the leptons are grouped into three generations. The generation-I consists of the lightest and the stable particles. Generation-II and Generation-III have the heavier and short-lived particles. The quraks and gluons carry a quantum number called "color" similar to the electric charge in electrodynamics. All hadrons must have an integral charge and neutral color. Quarks and leptons are therefore the fundamental building blocks of matter. There are four fundamental forces in nature having different strengths and ranges namely, strong force, weak force, gravitational force and electromagnetic force. The weakest force in the nature is Gravitational force which is a long range attractive force acting between any two objects. The long ranged electromagnetic forces act between any two charged particles and can be attarctive or repulsive depending on the nature of charges. The weak force is a short-range force which is responsible for β decay and neutrino interactions and the strong nuclear force of shortest range holds the neutrons and

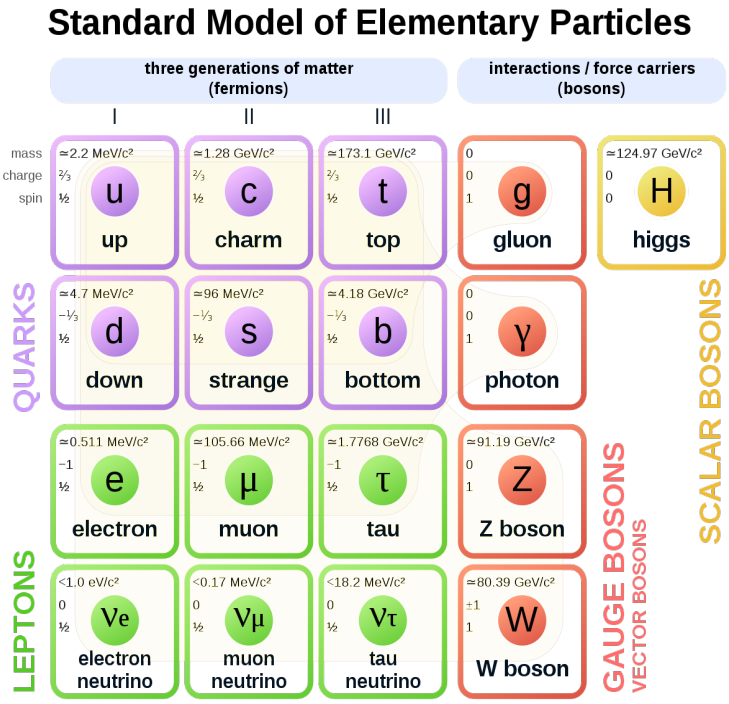

Figure 1.2: Fundamental particles in the Standard Model

protons together inside a nucleus. The Quantum Electrodynamics (QED) is the theory for the electromagnetic interactions. The Electro-Weak theory postulated by Glashow, Weinberg and Salam is a unified theory of electromagnetic and weak interactions [5] and the fundamental theory of strong interactions is given by the Quantum Chromodynamics (QCD) [6] which describes the interactions among quarks. The strong force is mediated by gluons which can interact with other gluons also. Photons are the carriers for the electromagnetic force and the weak interactions are mediated by massive $W^{\pm}$ and Z^0 bosons. The existence of hypothetical mediator particles of gravitational force called gravitons are yet not established. The latest addition to the Standard model of elementary particles is the Higgs boson which has been discovered by the ATLAS and CMS experiments at the LHC (Large Hadron Collider) in CERN, Geneva in 2012 and describes the mass of the elementary particles. The elements of the standard model have been shown in Fig. 1.2.

1.2 QCD: Theory of strong interaction

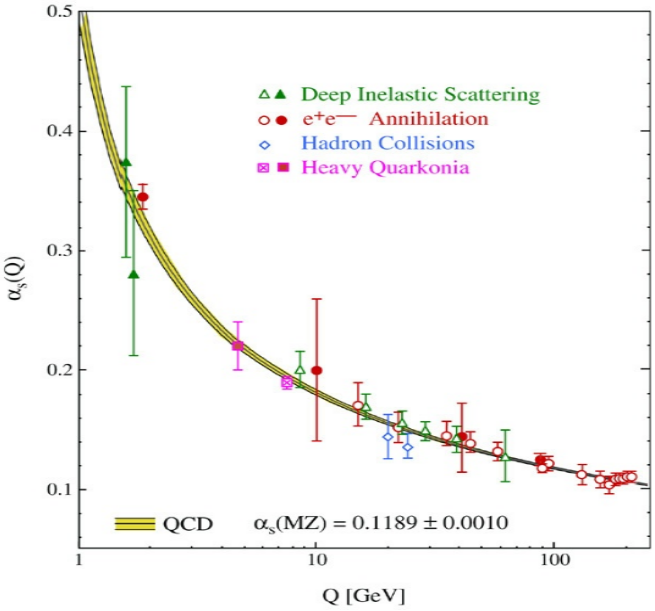

Figure 1.3: The strong coupling constant α_s as a function of the momentum transfer Q [7]

Quantum Chromodynamics (QCD), the theory of the strong interactions between the quarks and the gluons was introduced by Gell-Mann in 1972 [6]. Initially, the particles were classified according to charge, isospin, strangeness and they were grouped in eightfold way depending on their mass and properties which was thought to be explained by the three flavours of quarks. But this could not explain the existence of Ω^- hyperon consisting of three strange quarks with parallel spins as this combination of fermions is not allowed by Pauli's exclusion principle. It could be explained if there exists an additional quantum number of quarks proposed by B. V. Struminsky [8]. Similar contradiction was observed with the Λ^{++} baryon having three up quarks with parallel spins. Greenberg and Han–Nambu independently explained [9, 10] this mystery by introducing an additional quantum number of quarks called the color charge which is analogous to the electrical charges in Quantum Electrodynamics (QED). There are three different color charges namely red, green and blue (R,G,B) unlike two types of electric charge in QED. Due to this color charge,

gluons can interact among themselves unlike neutral photons in QED. Eight different color states are possible for gluons in QCD. The color of the quarks is changed by the gluon exchange, however the flavors of the quarks are not changed. Two important properties of QCD are asymptotic freedom and confinement [11]. The "asymptotic freedom", discovered in 1973 by Gross, Politzer and Wilczek [12, 13] states that the shorter the distance between the quarks are, the weaker is the strength of the interaction among them. This can be explained in terms of momentum transfer. The strong coupling (α_s) is defined as, $\alpha_s(Q^2) = \frac{12\pi}{(33-2n_f)ln(Q^2/\lambda^2_{QCD})}$, where Q^2 is the momentum transfer, n_f is the number of flavors and Λ_{QCD} is the so-called "QCD scale" with a typical value of about 200 MeV. The dependence of α_s on the momentum transfer Q has been depicted in Fig. 1.3. In the limit of large momentum transfer or short inter-quark distances, the coupling i.e. the interaction strength becomes so weak that the quarks almost behave like free particles. This is called asymptotic freedom. As a consequence, inside the hadrons, quarks are almost free. On the other hand, in case of low momentum transfer or if the distance between the quarks increases, the strength of the interaction increases. This is called "confinement". As a consequence, free or isolated quarks cannot exist in nature.

1.3 QCD phase diagram

As per the idea of the asymptotic freedom, if a nuclear matter is subjected to the condition of extremely high temperature or pressure, a state of deconfined quarks and gluons can be created. The Lattice QCD [14, 15] calculations show that the system undergoes a sharp transition beyond a critical temperature on increasing the energy density of the medium. The results are shown [16, 17, 20] in Fig 1.4 for the energy density ϵ normalized by T^4 vs temperature T. The figure shows a steep rise of energy density per T^4 when the temperature approaches a critical value of about $T_C \sim 173 \pm 15 MeV$. This calculation gives the critical energy density $\epsilon_C \sim 0.7\ GeV/fm^3$.

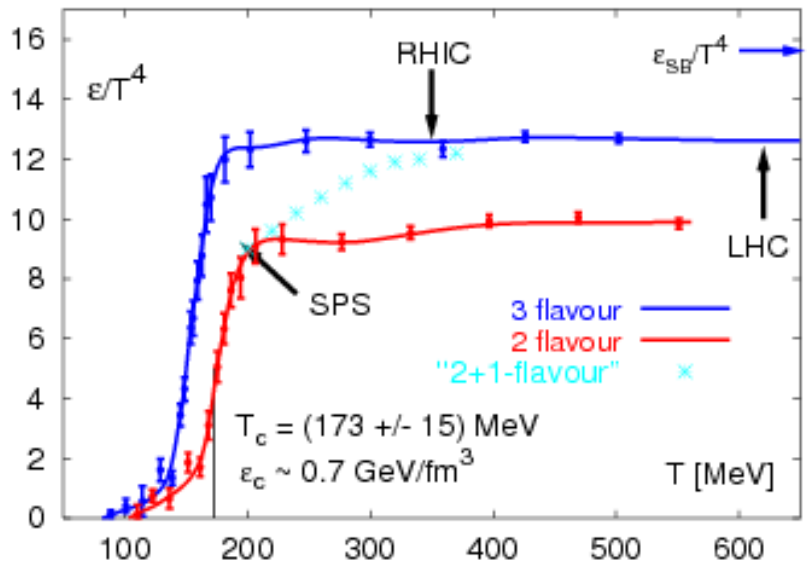

Figure 1.4: The temperature dependence of energy density of QCD medium obtained from Lattice QCD calculation with 2 light quark flavors, 3 light quark flavours and 2+1 (two light quarks and one heavy quark) flavor. The energy density steeply rises as the temperature approaches critical temperature T_C which is an indication of phase transition. Arrows indicate the energy densities reached in the initial stage of heavy ion collisions at the SPS, RHIC & LHC. [17, 18]

This sharp transition is an evident signature of phase transition. In a collision, therefore, if the energy density of nuclear matter is high ($\epsilon \approx 1\ GeV/fm^3$) [21], it is predicted that a state of deconfined quarks and gluons will be formed for a very short time which soon expands, cools down and undergo hadronization. The first search of such a state started at Bevalac at Barkeley National Lab, USA using Au beam at 1 GeV/nucleon hitting a target [19]. Subsequently, a number of experiments were performed in search of QGP at the Alternate Gradient Synchrotron (AGS), BNL, USA and at the Super Proton Synchrotron (SPS), CERN, Geneva like WA80, NA35, NA49, NA61 and others [19]. Then, in 2000, the Relativistic Heavy Ion Collider (RHIC) at BNL started its first run with four experiments BRAHMS, PHENIX, PHOBOS and STAR with Au+Au collisions upto $\sqrt{s_{NN}} = 200$ GeV/nucleon. After that, in 2010, experiments were performed at LHC using high energy beams of Pb ions at $\sqrt{s_{NN}} = 2.76$ TeV. Such a high energy density of above 1 GeV/fm^3 [22, 21], needed for the QGP formation has been achieved in high energy heavy ion col-

lisions at RHIC and LHC. A high energy density of about 12-14 GeV/fm^3 and about 6 GeV/fm^3 have been reached in the heavy ion collisions at LHC and RHIC respectively [23, 24]. A similar transition may also occur when the nuclear medium is compressed to a net baryon density of about 2-3 times the nuclear matter density. Such a transition from hadron phase to QGP phase and back to hadron is represented by a diagram known as the QCD phase diagram shown in Fig.1.5. It

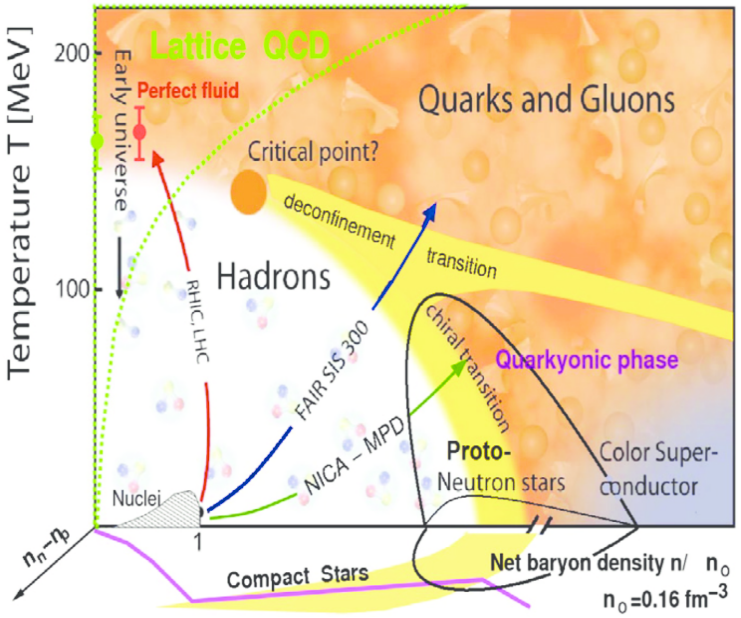

Figure 1.5: A schematic of QCD phase diagram [25]

shows the net baryon density or baryon chemical potential μ_B which is the energy required to add a baryon to the system or to remove a baryon from it versus the temperature of the fireball. The extreme region of high temperature and zero μ_B represents the early universe and has been created at LHC. At low temperature and high μ_B, the matter is expected to be like that of the core of neutron stars. These two extreme regions are represented by a QCD critical point. Lattice QCD predicts a smooth crossover at high T and low μ_B beyond the critical point [27, 28] and below the critical point temperature, the transition is of the first order [29]. At LHC, a cross-over transition is found to be around T_C =160 MeV. The top RHIC and LHC energies fall in the high temperature region and SPS, AGS, FAIR, NICA and low energies at RHIC probe mostly the high

net-baryon density region.

1.4 Evolution of QGP

In the colliders, two Lorentz contracted nuclei collide at the speed of light along the z-axis and move away from the collision zone depositing a large amount of energy in the collision region for a short duration of time in a very small region of high energy-density and small net baryon content. In the central rapidity region, a system of QGP is expected to be formed due to high energy deposition. The evolution of the fireball produced in the heavy ion collisions consisting of several

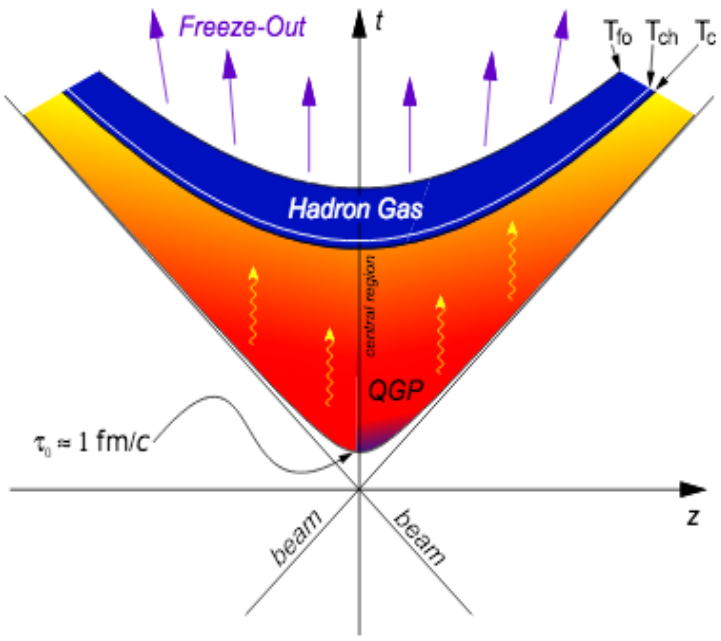

Figure 1.6: Light cone diagram showing the stages of a heavy ion collision [40]

stages has been depicted in Fig 1.6. The stages can affect the state of the final state particle depending on the particle production mechanism. The incoming nuclei are usually described as an independent collection of nucleons by the Glauber model [30] or a wall of gluons called

the Color Glass Condensate [31]. In such initial state models, there is an asymmetric nuclear overlap region due to the impact parameter of the nuclei and fluctuations in the positions of the incoming partons. Some of the incoming nucleons do not take part in the collision and pass away without interacting. These spectator nucleons can be used to measure the impact parameter of the collision. The partons may scatter-off of each other at an early stage before the QGP medium is produced. An interaction between quarks where a large amount of momentum is transferred, is called a hard scattering. The medium evolves and forms a soup of quarks and gluons that reaches a local equilibrium. The lifetime of this QGP phase is expected to be about 1-10 fm/c depending on the collision energies [32]. Then it expands, cools down and reaches a density and temperature where the partons get combined to form hadrons. The formed hadrons are described in the form of hadron-gas. After some time, the compositions of hadrons are frozen. This stage in the evolution process is called the chemical freeze-out [9]. As the medium expands further, the interactions between hadrons stop and hadrons reach the detectors freely with their final energies and momenta. This stage is called the thermal freeze-out and naturally, the thermal freeze-out temperature is lower than the chemical freeze-out temperature. From the ratios of the final state particles, the chemical freeze-out temperature is estimated to be around 160 MeV [33, 34, 35] and the thermal freeze-out temperature is found to be about 100–150 MeV,depending on the collision centrality and energy [36, 37, 38, 39].

1.5 Experimental Signature of QGP

The nuclei collide, thermalize, and form a hot thermalized medium of deconfined quarks and gluons which then expands, cools down and forms hadrons as depicted in Fig 1.7. Experimentally we cannot observe each stage separately, we observe only the final state observables by collecting the final state hadrons reaching the detector. Each stage of this evolution has some specific properties

and some signals through which the states can be probed. Since the lifetime of QGP is of the order of 10^{-23} second, the signals of QGP are mostly indirect.

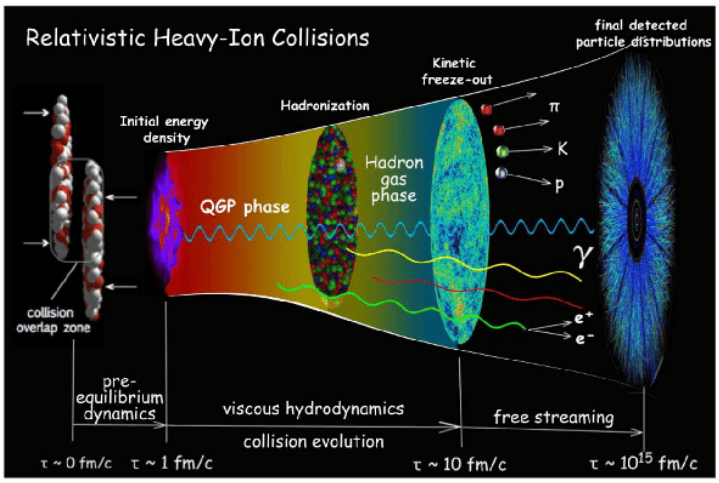

Figure 1.7: Schematic diagram of a collision: two nuclei collide, form the QGP state which expands and hadronizes and finally the hadrons reach freeze-out [26]

1.5.1 Bulk observable

A nuclear collision is characterized by its centrality, number of produced particles, energy density and pressure of the formed state, the freeze-out temperature and volume among others. The first measurement after a collision at any energy is mostly the charged particle multiplicity at the mid-rapidity region. The entropy produced in the early collision time transforms into particle multiplicities at a later stage. Rapidity is the relativistic measure of velocity of a particle defined by, $y = \frac{1}{2} ln \frac{E+p_z}{E-p_z}$, where E and p_z are the total energy & longitudinal momentum of the particle. At very high energy, $p >> m$,

$$y = \frac{1}{2} ln \frac{|p| + p_z}{|p| - p_z} = -ln(tan(\theta/2)) = \eta \tag{1.1}$$

where polar θ is the angle at which particles are emitted with respect to beam axis and η is called the pseudorapidity. Pseudorapidity can be measured easily as θ is a direct measurable quantity.

The pseudorapidity distribution of particles is related to rapidity distribution as,

$$\frac{dN}{d\eta dp_T} = \sqrt{1 - \frac{m^2}{m_T^2 cosh^2 y}} \frac{dN}{dy dp_T} \tag{1.2}$$

For $y \gg 0$, both are almost same, and for $y \approx 0$, a dip in $dN/d\eta$ distribution arises around $\eta \approx 0$ due to the presence of the mass term [40]. Mid-rapidity is important as most of the particles are formed due to the conversion of collision energy into particles in the transverse plane in this region. When two nuclei overlap, the distance between their centres is called the impact parameter of the collision and the number of nucleons in the overlapping zone is called the participant nucleons N_{part}. So, low impact parameter and large N_{part} imply a more central collision where the particle multiplicity in the final state is higher. As seen from the Fig 1.8 (right), the normalized pseudorapidity density

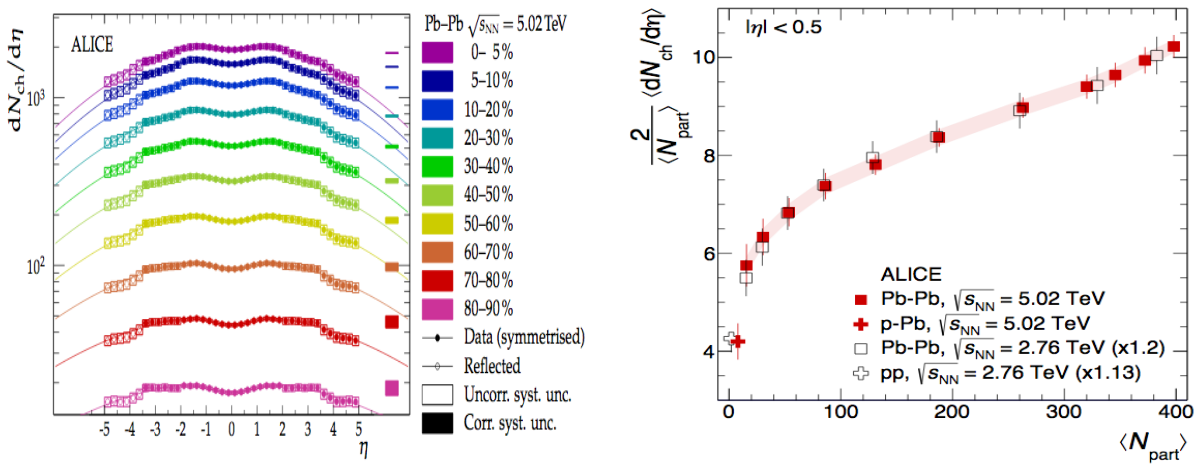

Figure 1.8: Charged particle pseudorapidity (η) distribution as a function of centralities and pseudorapidity density at mid-rapidity vs average number of participant nucleons ($< N_{part} >$) in PbPb collision at LHC energy. [41, 42]

increases with centrality indicating that the multiplicity increases faster than N_{part} at mid-rapidity, probably because of the contribution of the hard process to particle production [45]. As seen in Fig 1.8 (left), most of the particles are produced around mid-rapidity i.e. in the transverse plane around $\theta \approx 90^o$, and the yield decreases as one goes away from the mid-rapidity region. Total produced

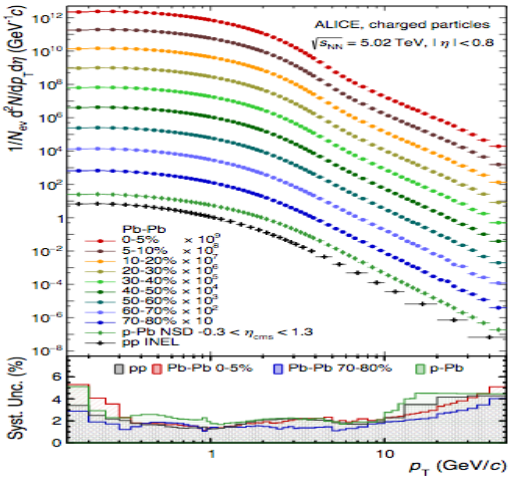

Figure 1.9: Transverse momentum spectra of charged hadrons in PbPb collision. [46]

charged particle multiplicity in a collison can be found from the η-distribution by extrapolating it upto beam rapidity and integrating over the whole range. The pseudorapidity distribution does not require mass identification unlike rapidity distribution. The η-distribution can be used to estimate the Bjorken energy density,

$$\varepsilon(\tau_0) = \frac{1}{\pi R^2 \tau_0}\frac{dE_T}{d\eta} = \frac{< E >}{\pi R^2 \tau_0}\frac{dN}{d\eta}|_{\eta=0} \tag{1.3}$$

where, the volume of the initially produced collision is considered as a cylinder of length $dz = \tau_0 d\eta$,πR^2 is the longitudinally projected overlap area of the colliding nuclei, dN is the number of particles ,$< E >$ is the average energy per particle and τ_0 is the proper time of thermalization taken as 1 fm/c.

The transverse momentum spectra of charged particles (Fig 1.9) and identified particles provide information about mean transverse momenta, temperature, radial flow and other observables [47]. The low p_T part of the spectrum exhibits an exponential behaviour having thermal origin, whereas, the high p_T region follows a power law distribution having contribution from the fragmentation of hard parton scattering. The entire range can be described by a Levy function which has both

an exponential part and a power-law function [40]. The inverse slope of the low p_T spectra gives the effective temperature at freeze-out that has a thermal origin as well as a contribution from collective flow of particles and the average radial flow velocity can also be obtained from the p_T spectra. Interestingly, for pp collisions at 7 TeV, such analysis gives a freeze-out temperature of about 154 MeV and radial flow velocity of about 0.45 c [43] which falls in the range of temperature required for a deconfinement transition. Therefore, high-multiplicity pp events are also candidates to show collectivity as well.

Collective flow

One of the signatures of the collective behaviour of the matter created in the collisions is the collective flow. In the non-central collision (Fig 1.10), the overlapping zone has an almond shape. A particle approaching towards the longer direction of the collision zone is more probable to suffer scattering and to change its direction than a particle approaching towards the shorter direction of the collision zone. Therefore, the density of particles in the short direction is higher resulting in a higher pressure gradient between the centre of the system and the vacuum along the short direction. Therefore, the flow velocity is also higher there and more particles are emitted in that direction[48].

This initial spatial anisotropy gets converted to the momentum anisotropy resulting in asymmetrical particle emission in the perpendicular plane. The presence of these anisotropies in the momentum distribution of the final state hadrons is the evidence of the medium flow and it is expressed as the Fourier expansion of the azimuthal distribution of the emitted particles with respect to the event plane angle Ψ: $E\frac{d^3N}{dp^3} = \frac{d^2N}{2\pi p_T dp_T dy}(1 + 2\sum_{n=1}^{\infty} v_n cos(n(\phi - \psi)))$. The coefficients of expansion are called flow parameters and are defined as, $v_n = \langle cos(n(\phi - \psi_n))\rangle$, ψ is the reaction plane angle. v_1 is directed flow coefficient, v_2 is elliptic flow coefficient and v_3 is triangular flow

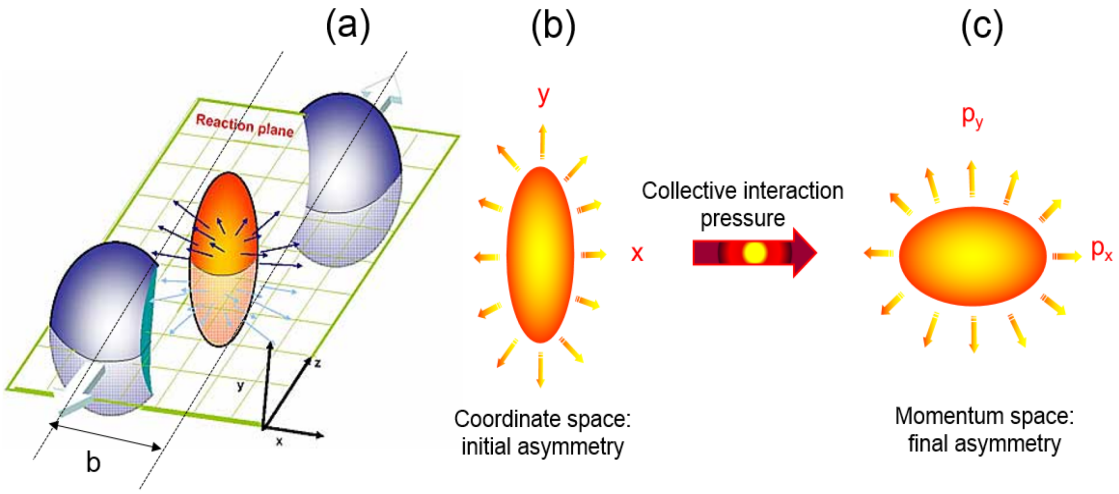

Figure 1.10: A non-central collision produces an almond shaped interaction zone. The initial anisotropy gets converted to momentum anisotropy via pressure gradient [44]

coefficient as shown in Fig 1.11. v_2 arises mainly due to the anisotropies in the overlap region of the incoming nuclei i.e. overall geometry, whereas, v_3 arises mainly from the fluctuations in the nucleon positions within the nucleus. Since, the plane angle is not experimentally measurable, the flow coefficients are measured by correlation between observed particles, for example, for elliptic flow, it is defined by, $\langle\langle e^{2i(\phi_1-\phi_2)}\rangle\rangle = \langle\langle e^{2i(\phi_1-\psi-(\phi_2-\psi))}\rangle\rangle \approx \langle v_2^2\rangle$.

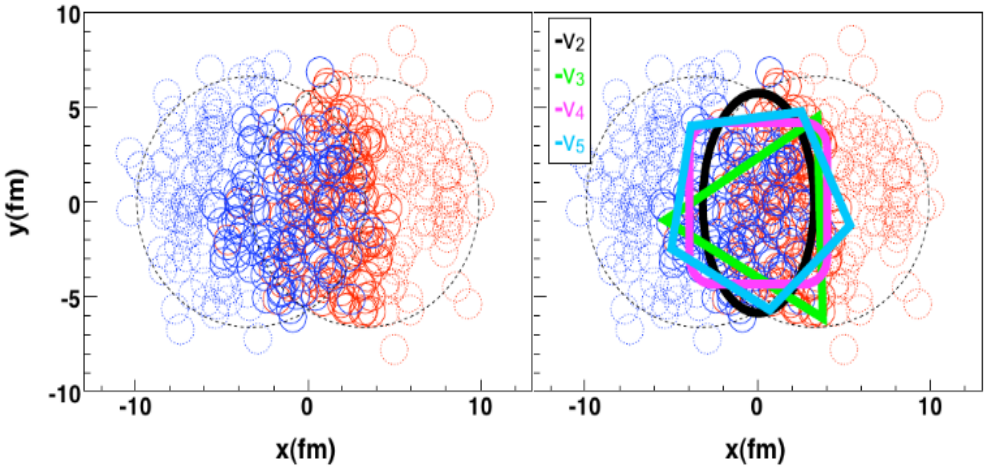

Figure 1.11: Simulation of Pb-Pb collision at $\sqrt{s_{NN}} = 2.76$ TeV with the PHOBOS Glauber Monte Carlo [49].

v_2 and v_3 provide dominant contributions to the azimuthal anisotropy.

A non-zero value of v_2 is produced due to the interactions among the constituents of formed matter in the initially spatially deformed overlap zone. The conversion of this spatial anisotropy to momentum anisotropy serves as a signature of re-interactions in the fireball.

A high value of the elliptic flow coefficients means the rescattering among the particles is large enough to bring the matter to local thermal equilibrium and the early pressure is also high. Since, the spatial anisotropy is highest at the beginning of evolution, therefore,the elliptic flow provides information about the thermalization time scale of the early stage of collision [50]. The earlier the equilibrium, the larger are the anisotropies [51, 52].

The anisotropy coefficients are sensitive to the properties of fluid - its viscosity and the equation of state. The viscosity to entropy ratio can be estimated from the shape and magnitude of these anisotropies, which shows that the QGP at RHIC and LHC is of the lowest viscosity to entropy ratio [34, 53, 38, 54].

Due to the fluctuation in the positions of nucleons in nuclei, thereby fluctuation in the shape of the initial collision region event by event, v_n also fluctuates event by event. The spatial anisotropy is defined by the eccentricity $\varepsilon = \frac{\langle y^2 - x^2 \rangle}{\langle y^2 + x^2 \rangle}$ where x and y are the positions of the participants [51]. v_n is found to be proportional to the eccentricity ε_n of the initial collision region for small n values [55]. For larger n, v_n is more sensitive to the viscosity of the fluid. Fig 1.12 shows the time evolution of the interaction zone where the energy density profile is represented by the contours and it shows how the system evolves from an asymmetric overlap zone to an almost symmetric system.

For a given p_T, the elliptic flow shows a mass ordering. v_2 decreases with increasing particle mass which is a consequence of the effect of the mass-dependent radial flow on the p_T spectrum of single particle[50] which is the radial expansion of the fireball created. It is known that, the radial flow gives a boost to the particles in transverse momentum which depends on the particle

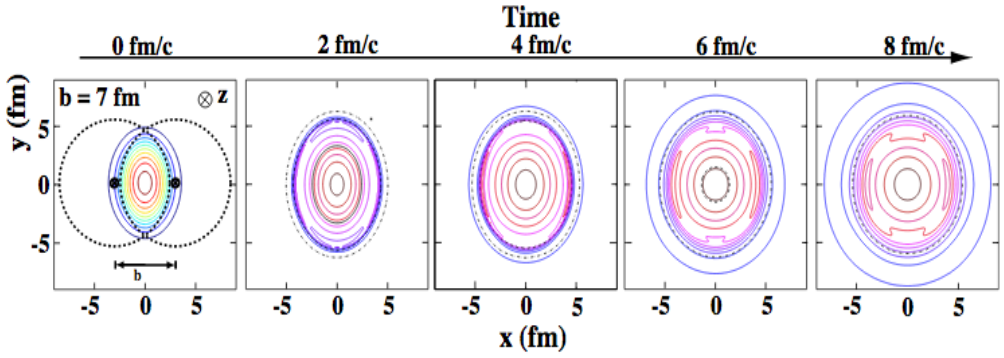

Figure 1.12: Time dependence of the formed initial transverse energy density profile in coordinate space in case of a non-central heavy-ion collision. [52, 51]

mass and flow velocity β of the medium, thereby, shifts the p_T distribution to higher p_T and this effect is more for heavier mass and higher flow velocity. Therefore, there is a suppression in the spectrum at low p_T which along with the range over which this happens increases with particle mass and flow velocity.

Now, as discussed earlier, in case of $v_2 > 0$, radial velocity is higher in x direction than in y direction, so the suppression in the spectrum at low p_T also as mentioned above. Therefore, it reduces the v_2 at low p_T ($p_T < 2$ GeV/c) by preventing the excess of particles with p_T along x direction over y direction. This reduction and the p_T range over which this occurs increases with mass and radial flow $v_{2,\pi}(p_T) > v_{2,K}(p_T) > v_{2,p}(p_T)$ [50].

But, interestingly, this mass ordering is not observed at intermediate $p_T, 2 < p_T < 5$ GeV/c region as shown in Fig. 1.13. The v_2 of baryons is higher than that of mesons in this region which can be explained if it is assumed that the hadronization occurs by the recombination of quarks [75]. The constituent quark number scaling of this observable provides a strong evidence of this quark coalescence [56]. But the situation is not same in LHC. There, the NCQ scaling is violated for $p_T > 3$ GeV/c [57]. Also, v_2 of ϕ-meson at the intermediate p_T shifts towards baryon instead of mesons. All these observations indicates that possibly the mass is responsible for the baryon-meson ordering of v_2 rather than the constituent quark numbers.

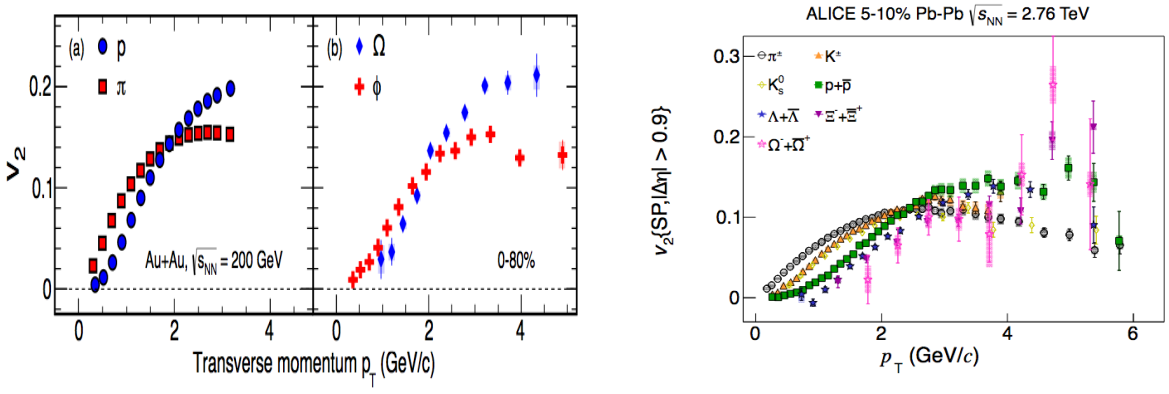

Figure 1.13: The v_2 as function of p_T for π, p and ϕ, Ω from minimum bias Au+Au collisions at $\sqrt{s_{NN}}$ = 200 GeV for 0-80% centrality (left panel) [56] and the p_T-differential v_2 for different particle species, forthe 5–10% centrality interval of Pb–Pb collisions at $\sqrt{s_{NN}}$ = 2.76 TeV. [57]

1.5.2 Electromagnetic probe and dileptons

Electromagnetic probes like photons and dileptons are useful probes of QGP medium as they are emitted from the medium almost without interacting & carrying the undistorted properties of the medium, whereas, hadrons are emitted mostly from the freeze-out surface. The direct photons are all the produced photons except those coming from decay of hadrons in the last stage of collisions. At high p_T, direct photons are produced from initial hard collisions and jet fragmentation. At low p_T, the direct photons are radiated from the thermalized QGP medium by $q\bar{q}$ annihilation and comptopn scattering. The thermal photons carry information about the initial temperature of the medium formed.

The high p_T isolated photon associated with a jet can be used to find the momentum of the associated parton. The prompt photons carrying the initial state information and its modifications in nuclei can be used to probe the gluon saturation.

An excess of photons is observed in heavy ion collision in the thermal region ($1 < p_T < 4$ GeV/c) compared to that in pp collisions as shown in Fig 1.14. But at larger p_T, no such enhancement is observed [58, 59]. The nuclear suppression factor R_{AA} (defined in sec. 1.5.5) of direct photons

is consistent with unity showing no suppresion [60]. Thermal photons reveal that the QGP can

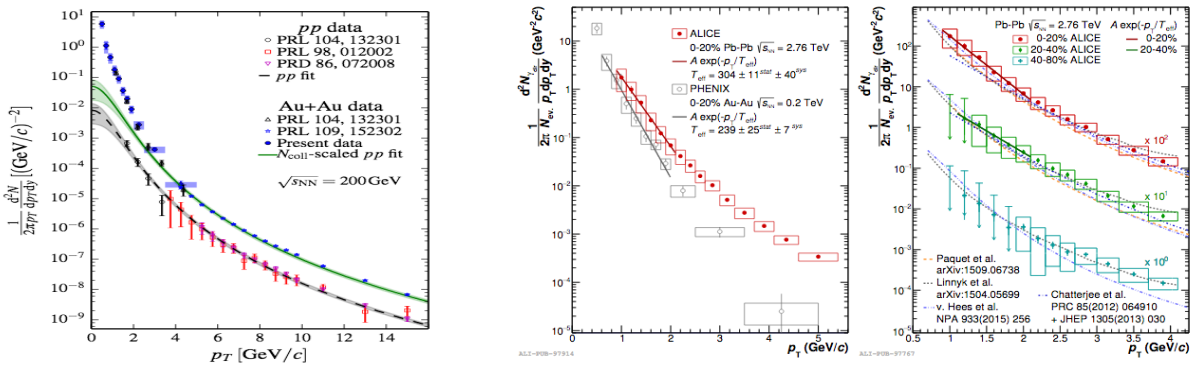

Figure 1.14: Direct photon spectra in AuAu and PbPb collision at 200 GeV and 2.76 TeV[58, 59]

reach a temperature of 300–600 MeV in central collisions at both 200GeV [61] and 2.76 TeV [62].

1.5.3 J/ψ suppression

The heavy quarks - Charm and Bottom quarks are produced at the early stage of the collision. Later, the available energy for particle production decreases which is not enough to create them. Also, as they are heavy, the possibility of formation of these quarks from thermal bath is very low. J/ψ is the bound state of charm and anti-charm quark. In the QGP medium, due to the presence of other quarks, anti-quarks and gluons around a c-quark, a charm quark may not be able to come close to an anti-charm quark to form a bound state, this is called color Debye screening. Due to this screening, interactions between heavy quarks and anti-quarks are diluted and the probability of the formation of J/ψ decreases. On the other hand, the open charms yields $(D^0, D^{\pm}, D_S)$ are enhanced as the charm quarks can combine with other light-flavor quarks around. A strong suppression in the yield of charmonia is observed in heavy ion collisions compared to that in pp collision [63, 64] at SPS energy. However, this suppression is lesser in LHC energies as shown in Fig 1.15, because, at sufficiently high energy, there is possibility of production of plenty of charm, anti-charm quarks resulting in a competition between suppression and regeneration. Also, higher

states of quarkonia can decay to produce more J/ψ.

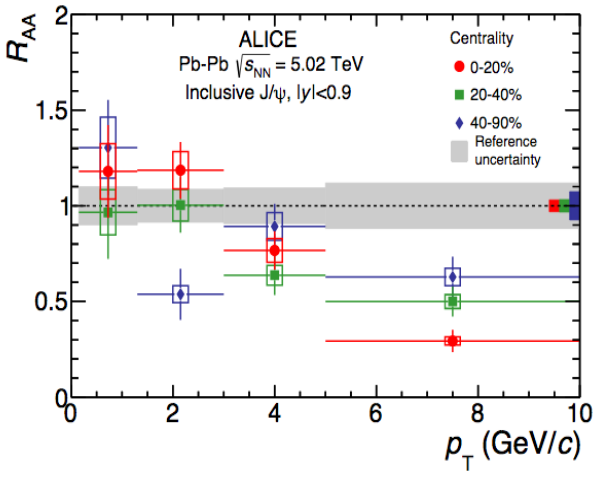

Figure 1.15: R_{AA} of inclusive J/ψ in Pb+Pb collisions at $\sqrt{s_{NN}}$ =5.02 TeV at midrapidity with p_T for different centralities [64]

1.5.4 Strangeness enhancement

Strangement enhancement is a strong signal of QGP [65]. Up (u) and down (d) quarks constitute the colliding nucleons. Strange quarks are not present in the initial state as valence quarks. So, if we get hadrons in the final state with strange quarks as its constituents, then it must have been formed through the inelastic collisions or as a part of the partonic medium via the process of hadronization. The temperature and energy density of the QGP medium in equilibrium produced in high energy collision is higher than the mass of strange quark. Therefore, strange quarks and strange anti-quarks can be abundantly produced in heavy ion collision compared to pp or pA collisions through several processes like flavour creation ($gg \to s\bar{s}, q\bar{q} \to s\bar{s}$) and flavour excitation ($gs \to gs, qs \to qs$) in early stage of the collisions or during the subsequent partonic evolution by gluon splittings ($g \to s\bar{s}$). These processes lead to enhancement of strange particles with respect to pions in heavy-ion collisions. This enhancement does not show a significant dependence on either collision centrality or the collision energy. The ratio of yields of strange particles to pions

decreases for peripheral collisions as the overlap of the colliding nuclei is very small and becomes similar to the observed pp collisions. Recent study has shown a significant enhancement of the strange and multi-strange particles to pions with increasing particle multiplicity in pp collisions at 7 TeV [66]. This enhancement increases with increase in strangeness content rather than mass or baryon number. At high multiplicity, the yield ratios become similar to that observed in Pb–Pb collisions [66] as shown in Fig 1.16.

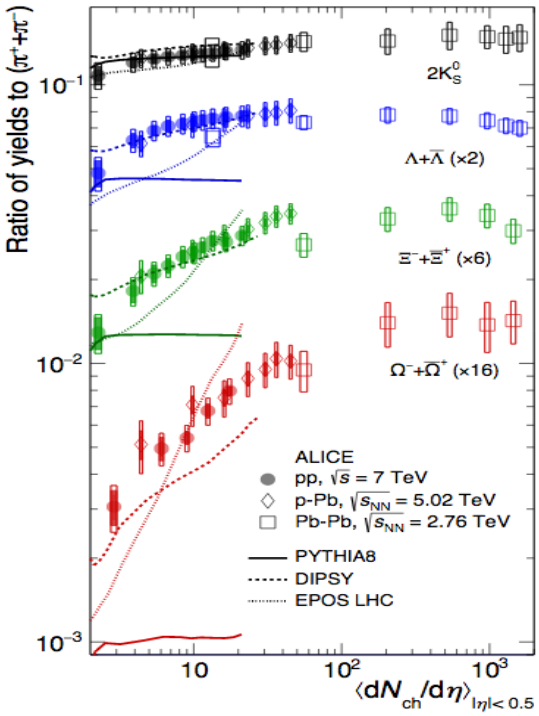

Figure 1.16: p_T-integrated yield ratios of $K^0_S, \lambda, \Xi, \Omega$ to pions $(\pi^+ + \pi^-)$ as a function of $< dN/d\eta >$ measured in mid rapidity [66]

1.5.5 Hard probe: partonic energy loss in medium

Jet Quenching

High p_T partons are produced at the initial stage of the collision prior to the production of QGP and they lose energy as they traverse through the medium. Therefore, they are considered to be useful to probe the early stages of the collision as well as the entire medium evolution. The hard

partons fragment into a collimated shower of correlated particles in a conical volume called Jets [67]. Thus, measurement of Jets can shed light on the energy loss mechanism in the medium. The fragments carry fractions of the original parton momentum. This fragmentation function is modified in AA collision compared to that in pp collision due to the presence of medium in AA collision. If a pair of back to back jets carrying equal amount of energy called di-jets is produced near the periphery of the fireball, one escapes directly losing lesser energy compared to the other one that traverses through the medium and loses a sufficient amount of energy by collisions with medium partons, or via gluon bremsstrahlung process as shown in Fig 1.17. This is known as Jet quenching. This Jet quenching is expressed by Nuclear Modification factor R_{AA} and defined by,

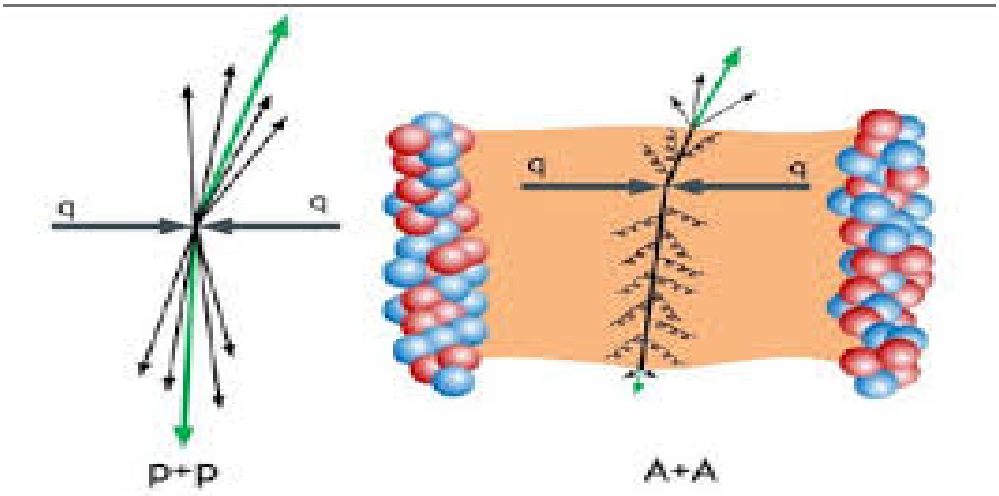

Figure 1.17: Jet-quenching in heavy ion collision. Figure is taken from [71]

$$R_{AA}(p_T) = \frac{d^2N_{AA}/dydp_T}{< N_{coll} > \times d^2N_{pp}/dydp_T} \tag{1.4}$$

where $< N_{coll} >$ is the mean number of binary nucleon-nucleon collisions in a single nucleus-nucleus collision obtained from Glauber model. If there is no medium, the nucleus-nucleus collision will be just the superposition of nucleon-nucleon collisions, the hard processes are then expected to follow the N_{coll} scaling and R_{AA} will be unity. So, this quantity measures the deviation of the yield in

A-A collisions compared to the scaled p-p reference as the high p_T particles are suppressed due to the energy-loss in the medium. Therefore, R_{AA} <1 at high p_T indicates the presence of medium. In central collisions, hadrons suffer a higher energy loss in the medium and are suppressed by a factor of almost 6 at about 7 GeV/c as shown in Fig 1.18. The suppression decreases slowly with increase in p_T. However, at lower p_T, R_{AA} can be >1 which is likely to be due to the cronin effect [68] or the validation of N_{part} scaling rather than N_{coll} scaling. This suppression of high-p_T

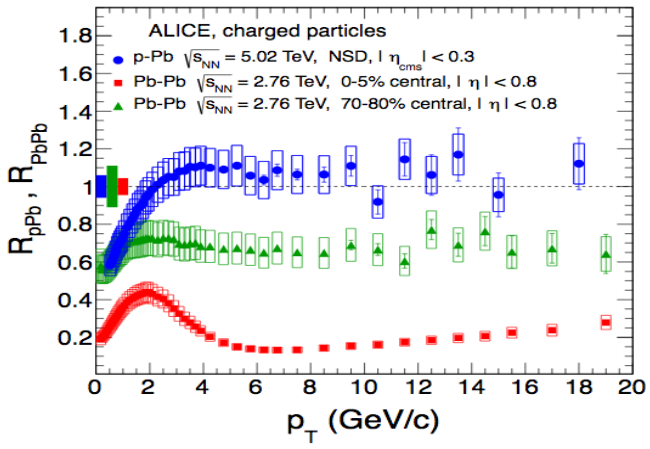

Figure 1.18: The nuclear modification factor of charged particles as a function of transverse momentum [69]

hadrons was seen by the STAR experiment at RHIC using dihadron correlations. The suppression of the away-side peak was seen in AuAu collision, whereas no suppression was observed for dAu and pp collision. This gives the evidence of the formation of a medium in heavy ion collision [70]. Like hadronic R_{AA}, jet p_T spectrum is also suppressed in heavy ion collisions with respect to p+p collisions indicating the energy loss of jets in the medium. This suppression is quantified as Jet-R_{AA}. Jets are studied to understand the energy loss mechanism and its dependence on path length in the medium. The interactions of the jets with the medium results in a modification of their structure, particle composition, fragmentation, splitting functions and redistribution of their energy which have been discussed later. Alternatively, R_{CP} can be measured instead of R_{AA}, where

instead of pp collisions, peripheral heavy ion collisions are used as the reference. This is usually done when the corresponding p+p data are not available for reference. The advantage is that if other nuclear effects are present in the R_{CP} cross-section, it will get cancelled in the ratio and also, the collisions are recorded at the same time thereby having same detector conditions. However, QGP effects can be there in peripheral collisions which can make the interpretation difficult.
Cold nuclear matter effects, which refer to the differences observed in p+A collisions with respect to p+p collisions where medium is likely not to be formed, but the production of the final observable can be influenced by a nucleus present in the initial state, are studied by the measurement of R_{pPb} and it is used to decouple the effects observed in A+A data coming from the medium interactions. R_{pPb} is found to be unity within the uncertainties of the measurements beyond p_T= 2 GeV/c which indicates that the reason of the observed suppression in A+A collisions cannot be cold nuclear matter effects. At low p_T, it is comparable with R_{PbPb} at 70-80% centrality.

Di-hadron correlation

Di-hadron correlation is one of the methods to probe jet-physics. In a hard parton scattering, two back to back partons separated by 180^0 in the transverse plane are produced as depicted in Fig 1.19. A high-p_T hadron called trigger particle is identified whose momentum can be considered as the jet axis of the parent parton. So it is used to define the coordinate system. The other hadrons' momenta are calculated with respect to the momentum of this trigger particle. In the di-hadron correlation with high p_T trigger in $\Delta\eta, \Delta\phi$, the near-side peak around $\Delta\phi$= 0^o arises from associated particles produced by the same parton as the trigger and the away-side peak near 180^o in $\Delta\phi$ arises from the associated particles from the partons opposing the trigger generating one. One of the first measurements of jet quenching through di-hadron correlation was performed by the STAR collaboration at RHIC [72], where the observed disappearance of the away-side peak

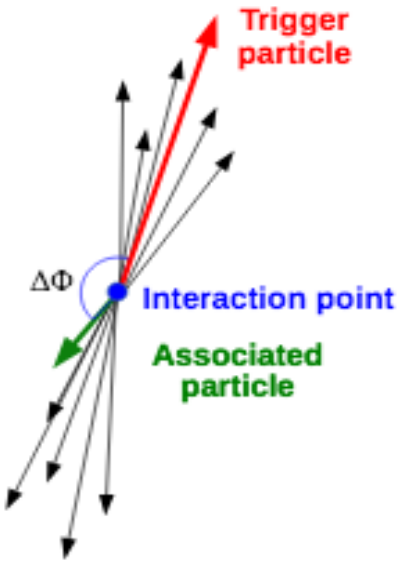

Figure 1.19: Schematic diagram showing a high-p_T hadron as the trigger particle in the study of dihadron correlations in a p+p collision

in Au-Au collisions indicated substantial interactions of the partons with the medium. The near side peak was similar in pp and Au-Au collisions which can be due to the effect of a strong "surface bias" that means, the trigger selects jets with a short in-medium path length. The suppression of away-side peak relative to p+p or d+Au is quantified by a factor similar to R_{AA} as, $I_{AA} = \frac{Y_{AA}}{Y_{pp}}$ [72] where Y_{AA} and Y_{pp} are the away-side yields for Au-Au and p-p collisions. More number of particles at low p_T compared to that at high p_T are caused by gluon bremsstrahlung or collisional energy loss, so I_{AA} <1 at high p_T. On the other hand, no differences are observed between d+Au and p+p collisions on the near or away-side [73] which indicates that any modifications observed are due to hot nuclear matter effects. The near-side peak can be used to study the angular distribution of momentum and particles around the triggered jet. The ALICE collaboration measured di-hadron $\Delta\eta - \Delta\phi$ azimuthal correlations in Pb-Pb at $\sqrt{s_{NN}}$ =2.76 TeV. At low p_T, a near-side ridge structure is seen and the away-side is broad which indicates hydrodynamics as the underlying physics. At higher p_T, there is a "jet" peak in nearside and a small recoiling jet distribution in

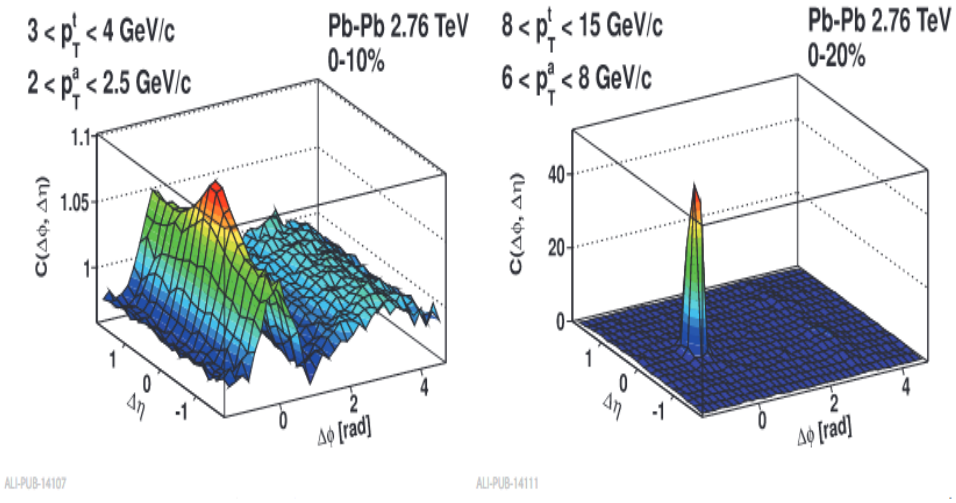

Figure 1.20: Di-hadron azimuthal correlations in Pb-Pb for two different p_T regime

away side as shown in Fig. 1.20. Similar to di-hadron correlations, correlation studies between hard hadrons and reconstructed jets are performed to overcome the drawbacks of bias imposed by the background suppression methods as described earlier. In this case, the yield of reconstructed jets within $|\pi - \Delta\phi|$ <0.6 is estimated with respect to an already selected reconstructed hadron [74]. Compared to dihadron correlations, it is more advantageous because a jet has a stronger correlation with the kinematics of the parent parton than a high p_T hadron as shown in Fig. 1.21. For very high p_T hadrons, the jets correlated with that hadrons come from hard process, whereas, for low p_T hadrons, the yield will be dominated by combinatorial jets. Now, the difference between the jet yields in these two cases Δ_{recoil} are estimated to subtract the background from jets and compared to that in p+p collisions. It is seen that there is substantial jet suppression in A+A collisions relative to p+p collision.

1.5.6 Quark coalescence as an indirect probe of QGP

A strong nuclear suppression in the yield of pions in the intermediate transverse momenta (> 2 GeV/c) in central Au + Au collisions was observed in Relativistic Heavy Ion Collider (RHIC) [75], compared to that in p+p collisions [76]. The reason of the observed suppression of the intermediate

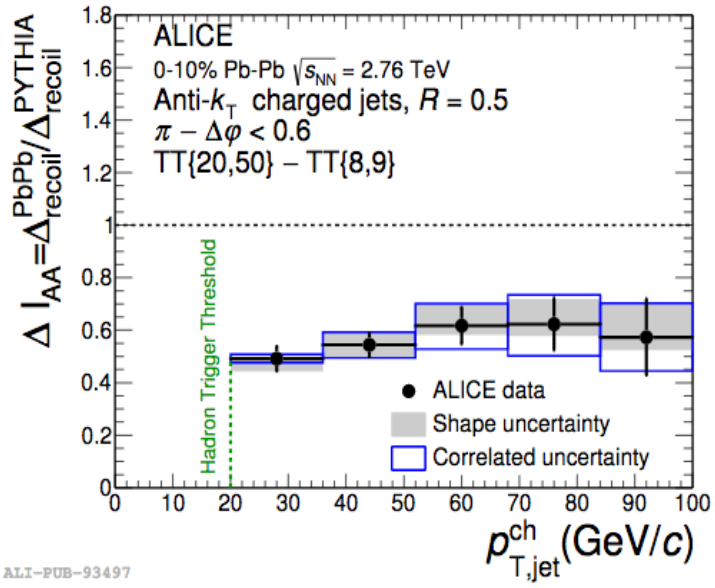

Figure 1.21: Suppression of jets in Pb+Pb collision with respect to p+p collision. Δ_{recoil} is the difference between the number of jets within $\pi - \Delta\phi < 0.6$ of a hadron with $20 < p_T < 50$ GeV/c and a hadron with $8 < p_T < 9$ GeV/c

and high p_T hadrons was experimentally established to be due to the energy loss of partons in the hot and dense medium [67] known as jet quenching. But this suppression was seen to be absent in case of protons and Λ's which is very surprising. The other interesting observations are that, the p/π ratio exceeds unity for transverse momenta 2 to 5 GeV/c and R_{AA} is close to 1 for baryons while it is much less than 1 for pions in this momentum range. The effects are also seen in Pb-Pb collision at 2.76 TeV in ALICE shown in Fig 1.22. Apart from that, the elliptic flow also shows a particle species dependence [56, 77]. This is called Baryon Anomaly. It was proposed that in the region of high parton density, hadrons of a few GeV momenta are produced by recombination of partons instead of fragmentation. Now, in the exponential regime of the parton spectra, recombination dominates over fragmentation but fragmentation takes over when the parton spectra exhibits a power law form [75]. There is also an alternative explanation of this behaviour using radial flow that pushes the massive particles more to higher p_T as discussed earlier.

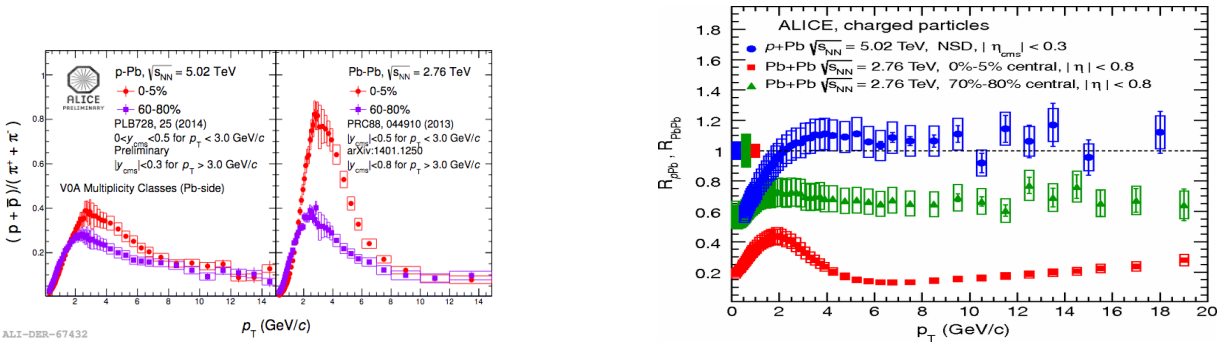

Figure 1.22: Left: p/π ratio with p_T in pPb and PbPb collisions at $\sqrt{s_{NN}}$ =5.02 and 2.76 TeV, respectively. Right: R_{AA} of charged particles with p_T in minimum bias p+Pb compared to 0-5% and 70-80% Pb+Pb collisions [78, 79]

1.6 Motivation of this study:

Measurement of jets in proton-proton collision systems allows to test pQCD and hadronization models. Also, these measurements provide the baseline for the heavy-ion studies like the modification of jet structures and production rates in heavy-ion collisions due to the presence of the medium. Jet measurements in pp collisions also constrain non-perturbative effects, such as hadronization [9]. The ultimate goal of jet measurements in heavy ion collisions is to learn about the QGP by comparing the results with that of p+p collision. Measurements of jets in small system like p+p collisions are already complicated. Additionally, it is more challenging to measure jets experimentally in heavy ion collisions due to the large background. Subtracting the background using different methods and the selection criteria to remove the background contribution impose biases on the resultant jet.

As discussed earlier, the jet yield and fragmentation are modified due to the interaction with the medium formed in heavy ion collisions with respect to the pp collisions. Therefore, the energy loss mechanism of the partons in the medium can be understood through the measurement of such modifications.

1.6.1 Jets

In a collision, a hard process leads to a partonic shower called parton jet which later hadronizes and generates a collimated shower of hadrons known as hadron jet. But the definition of a jet is ambiguous both in partonic and hadronic level [9]. In the partonic level, in a process like $e^+e^- \rightarrow q\bar{q}$, if the quark emits a gluon at an small angle relative to itself, it is taken as a part of the jet but if the gluon is emitted at large angle, it may be considered as a third jet. In hadronic level also, it is unclear which final state particles should be considered as the part of jet and it is more difficult in heavy ion collision than p+p collision due to large background as shown in Fig. 1.23. It is very complicated whether the particles generated from any interaction between

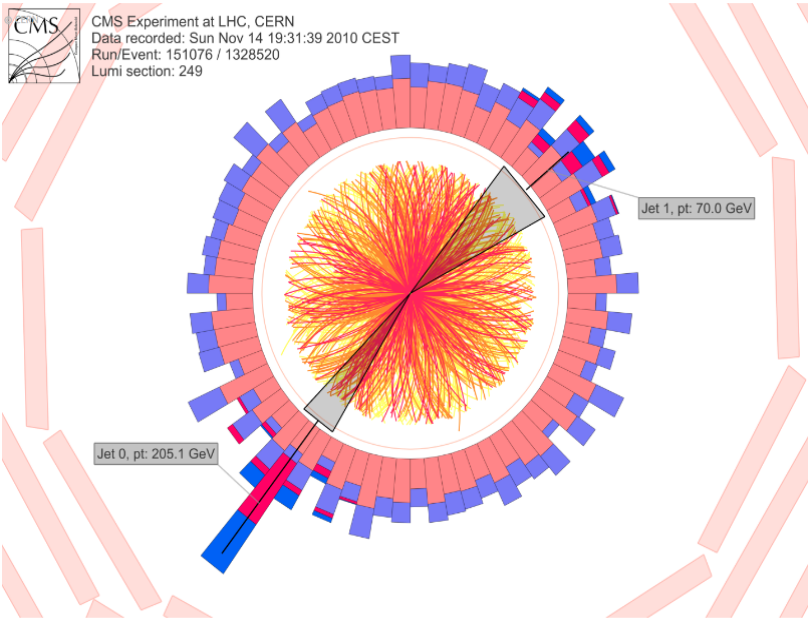

Figure 1.23: A dijet event in a Pb+Pb collision at $\sqrt{s_{NN}}$= 2.76 TeV in CMS showing the large background for jet measurements in heavy ion collisions.

the daughters of the parton and the medium particles should be taken as part of the jet or not. For this, jet measurements are different from the other measurements like particle yield. A proper jet finding algorithm and background subtraction methods should be used for the study of jets. However, to suppress the background contribution in the measurements of reconstructed jets, a

minimum momentum threshold for the constituent particles is usually used which may bias the measured jet also. The momentum distribution of a hadron in the jet is given by the fragmentation function $D_h(z)$, where z= p^h/p represents the fraction of parent parton's momentum taken away by the hadrons. This fragmentation function is modified in heavy ion collision due to the energy loss of the partons via interaction with the medium. As the hard partons have much higher transverse momentum and energy than the medium partons, so the energy loss broadens and softens the jet. Hence,this study allows to understand the energy loss mechanism in the QGP medium. Mostly, the collective flow contributes to the correlated background in jet measurements. But jets themselves can result in a non-zero v_n through jet quenching, thereby making the background subtraction complicated for jet studies.

1.6.2 Effect of medium in jets

From the discussions so far, the energy loss of partons in medium is evident, though how they interact with medium is not yet discussed. As already discussed, measurement of a jet is not the measurement of a parton, rather it measures the final state particles that come from the fragmentation of the parton. The interactions with the formed medium can shift the energy from higher momentum final state particles to lower momentum and therefore jets are broadened by the energy shift from higher p_T to lower p_T final state particles through the interactions with the formed medium. Similarly, if medium partons become correlated with the hard parton via interactions with medium, then also modifications can occur [80]. This lost energy may or may not be reconstructed as part of a jet depending on the jet finding algorithm. Several observables provide evidence in support of the modification of jets in medium. Some observables that focus on the average property of jets as a function of directly measurable quantities include di-hadron correlations, jet shape ($\rho(r)$), momentum distribution of particles in a reconstructed jet, called

the fragmentation function $D_{jet}(z)$ etc. Some new observables include angularity (g), dispersion ($p_T D$), LeSub, jet mass etc., some of these observables are discussed below. Jet shapes allow to study the information on how constituents are distributed in a jet. The jet-medium interaction also results in jet substructure modifications which can be quantified by different jet-shape observables.

Fragmentation function with jets

The fragmentation function measures the distribution dN_h/dz of the momentum fraction z, where $z=p^h/p$ is the fraction of parton's momentum or jet momentum carried away by hadron. It is defined as [81],

$$D_h(z) = \frac{1}{N_{jets}} \frac{dN}{dz_{ch}} \tag{1.5}$$

From the Fig 1.24, it is seen that there is a significant change in the fragmentation function in the

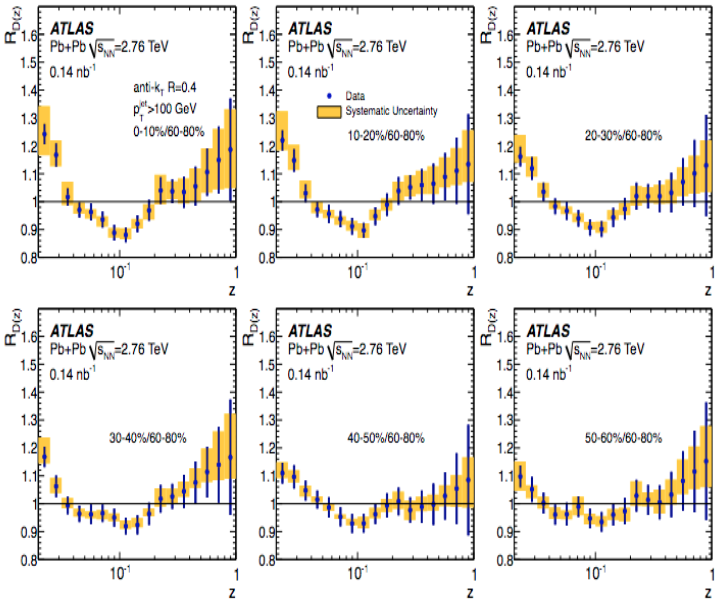

Figure 1.24: Ratio of fragmentation functions of reconstructed jets for different centralities to 60-80% in Pb+Pb collision at 2.76 TeV [82].

most central collisions relative to that in the peripheral collisions. An enhancement is seen at low

z whereas, there is a reduction at intermediate z which indicates the redistribution of the energy loss for mid to high p_T hadrons to low p_T particle production. It is one of the direct observations of the softening of the fragmentation function in the medium. However the definition includes the parent parton's momentum and jet momentum is not same as parton momentum. But the fragmentation functions estimated with large radii jets are approximately same as the definition.

Jet shape

Another observable related to the structure of the jet is the jet shape ($\rho(r)$) which measures the radial distribution of the transverse momentum of the tracks in a jet and is defined by,

$$\rho(r) = \frac{1}{\delta r}\frac{1}{N_{jet}}\sum_{jets}\frac{\sum_{tracks\in[r_a,r_b]} p_T^{track}}{p_T^{jet}} \tag{1.6}$$

Here, the jet cone is divided into several annuli with radial width of δr and each annular ring has an inner radius of $r_a = r - \delta r/2$ and outer radius of $r_b = r + \delta r/2$.
The $r = \sqrt{(\phi^{track} - \phi^{jet})^2 + (\eta^{track} - \eta^{jet})^2} \leq$ R is the radial distance of the track from the jet axis. The transverse momenta of the tracks and the reconstructed jet are denoted as p_T^{track} and p_T^{jet} respectively. In the numerator, the transverse momenta of the charged particles inside one annular ring is summed to estimate the fraction of the reconstructed jet momentum p_T^{jet} carried by the particles inside each annulus. The final result is obtained after averaging over the total number jets (N_{jet}) under consideration.

Fig 1.25 shows that the difference in $\rho(r)$ between p+p and Pb+Pb is largest for 0-10% centrality in Pb+Pb collision at larger radii. Whereas, the radial distribution of the p_T of the tracks in a jet is almost similar for p+p and 50-100% Pb+Pb collision. The large deviation from unity in the ratio at large radii (r > 0.2) indicates that jets are broadened in the medium in most central Pb+Pb collisions with respect to that in p+p collisions for a particular $\sqrt{s_{NN}}$ [85] and this is

expected due to the redistribution of the lost energy of the jets in the medium at large distances from the jet axis.

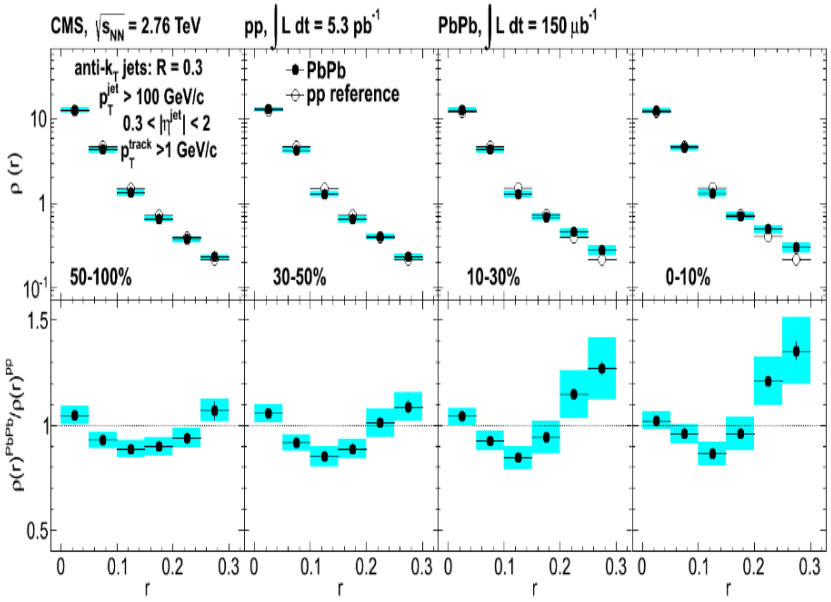

Figure 1.25: CMS measurement of $\rho(r)$ as a function of jet radii in Pb+Pb and p+p collisions and their ratios at different centralities [85].

LeSub

One of the new observables is LeSub [84] defined by,

$$LeSub = p_T^{lead,track} - p_T^{sublead,track} \tag{1.7}$$

It describes the hardest splitting, so it should not be sensitive to the background. LeSub measured in Pb+Pb collision at $\sqrt{s_{NN}} = 2.76$ TeV for jets with charged particle constituents (charged jets) for R=0.2 agrees with the PYTHIA simulation results of p+p collisions well indicating that the presence of medium cannot affect the hardest splittings, though, ALICE data are for relatively low momentum and relatively small jets, which selects more collimated fragmentation patterns.

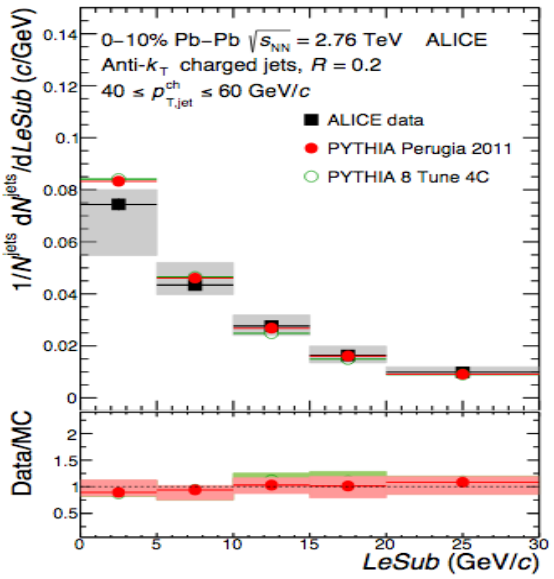

Figure 1.26: Figure from ALICE [84]. Lesub distribution in Pb+Pb collisions for R=0.2 charged jets with momenta between 40 and 60 GeV/c compared to PYTHIA simulations

Dispersion

Quark jets have harder fragmentation functions than gluon jets. Therefore, jets with hard constituents carrying a large fraction of the jet momentum are mostly generated from them. Dispersion is defined as,

$$p_T^D = \sqrt{\sum_i p_{T,i}^2} / \sum_i p_{T,i} \tag{1.8}$$

where $p_{T,i}$ represents the transverse momentum of the i-th constituents of the jet. It tells how hard or soft the fragmentation is [83]. This quantity was initially introduced to separate between quark and gluon jets as quark jets yields a larger mean p_T^D [86]. Fig 1.26 shows the p_T^D distribution of charged jets in Pb+Pb collisions at $\sqrt{s_{NN}}$ = 2.76 TeV for R=0.2 having $40 < p_T < 60$ GeV are compared to that of PYTHIA. It was seen that the mean p_T^D was larger compared to the PYTHIA (p+p) but the data are close to PYTHIA quark which indicates a quark jets bias or

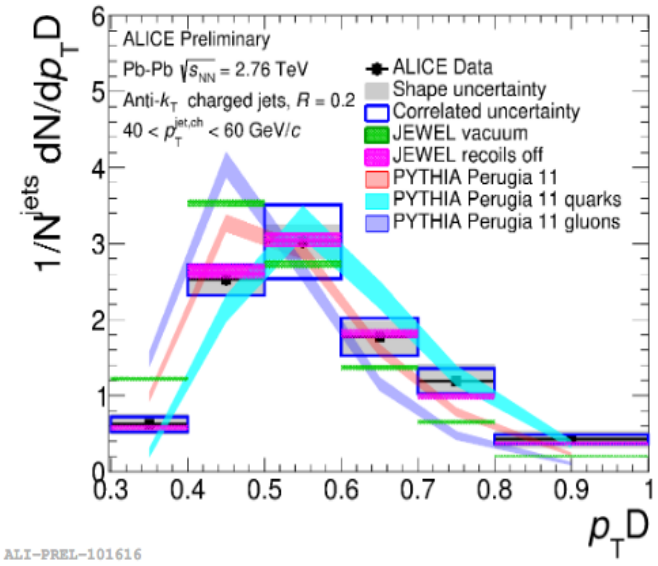

Figure 1.27: Figure from ALICE [83]. p_T^D shape distribution of charged jets for R=0.2 in Pb+Pb collisions along with PYTHIA comparison for 40< p_T^{jet} <60 GeV/c

harder fragmenting jets.

Angularity

Another jet shape variable that measures the radial energy profile of the jet is the angularity or girth and it is defined by,

$$g = \sum_i \frac{p_T^i}{p_T^{jet}} |\Delta R_{jet}^i| \tag{1.9}$$

where p_T^i denotes the transverse momentum of the i-th constituent of the jet with reconstructed jet momentum p_T^{jet} and ΔR_{jet}^i is the distance between i-th constituent and the jet axis in (η, ϕ) space. g will increase with the broadening of the jet in the medium and will decrease if the jet is collimated. The gluon jets are broader than quark jets and therefore they have a higher average g. In the ALICE Pb+Pb collisions as shown in Fig 1.27, it is observed that compared to the PYTHIA results, g slightly shifts towards left i.e. smaller values [83], though the shift is unclear,

but this indicates a higher collimation of the core in Pb+Pb collisions than in p+p collisions. The comparison of data with PYTHIA shows that it is closest to PYTHIA predictions for quark jets. This can be due to the quark bias towards quarks.

These shape studies are important to understand the intra-jet broadening or collimation as a

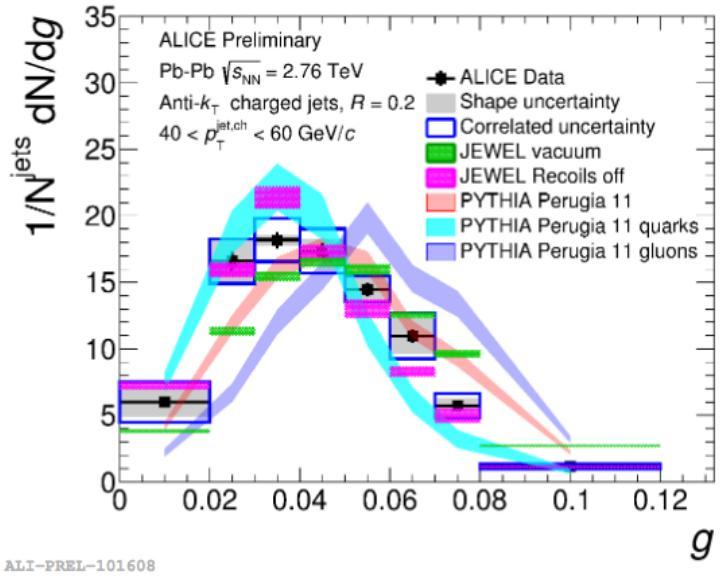

Figure 1.28: Figure from ALICE [83]. Angularity distribution for charged jets in Pb+Pb collisions for R=0.2 with 40< p_T^{jet} <60 GeV/c along with PYTHIA,JEWEL and to q/g PYTHIA results.

result of jet quenching. Jet shape study can help to answer one more question : whether jets fragment in the medium, or they just lose energy in the medium and then fragment after reaching the surface like vacuum fragmentation. If the latter one is true, then jet quenching is a shift in parton p_T followed by vacuum fragmentation and it indicates the consistency of jets shapes in Pb+Pb collisions with p+p collisions. But a shift in g indicates the fragmentation in the medium. The thesis is organized as follows. In chapter 2, We have discussed the overview of LHC and ALICE experiment, its sub-detectors and their working principles. In the present work, the Inner Tracking System (ITS) and Time Projection Chamber (TPC) are used to detect charged particles. In chapter 3, the in-medium modification to the two jet shape observables i.e., the differential jet

shape ($\rho(r)$) and the angularity (g) in the most central Pb-Pb collisions at $\sqrt{s_{NN}}$= 2.76 TeV using two event generators JEWEL (recoil OFF) and EPOS-3 in the jet-p_T range of 20-40 GeV/c have been studied. The study of medium-induced modifications to the substructure of inclusive charged jets indicates a redistribution of energy inside the jet cone and provides insight into the energy loss mechanisms of jets in the medium. JEWEL with recoil OFF has been used mainly as a reference as that can explain the global jet observables satisfactorily but lacks in jet-shape variables at higher jet-radii. EPOS-3 takes into account a hydrodynamically evolving bulk matter, jets and hard-soft interactions. A comparison between the results from these models shows that while JEWEL (recoil OFF) does not explain the distribution of lost energy at higher radii with respect to the jet-axis, EPOS-3 explains the effect quite well. The observation indicates that the unconventional hard-soft interactions as implemented in EPOS-3 can be instrumental in the realistic modelling of jet-medium interactions. JEWEL is a Monte Carlo simulation program designed for the study of jet quenching in heavy ion collisions. It interfaces a perturbative final state parton shower with the medium and accounts dynamically for the interaction between jet and medium. JEWEL can be used in two operational modes: recoil ON and OFF. In the recoil OFF mode, the energy and momentum transferred to the background partons are not taken into account in the final state fragmentation. EPOS-3 is a parton based model with flux tube initial conditions. In EPOS, the partonic energy loss scheme doesn't involve the interaction of jets with hydrodynamic fields. The secondary hard-soft interactions take place during the hadronization and the hadronic cascade phase.

In chapter 4, the analysis details of the ALICE data in pp collisions at $\sqrt{s_{NN}}$ =5.02 TeV have been presented. The aim of the analysis is to obtain the jet-shape parameters i.e. angularity, dispersion and LeSub. In this chapter, data sets, events and track selection cuts, jet finding cuts, jet reconstruction algorithm have been discussed. Additionally, efficiency correction on the raw

data has been performed through the unfolding method. A closure test has also been performed to validate the unfolding procedure. The sources of systematic uncertainties have been discussed. Finally the fully corrected results are presented along with the model comparison for pp collision at $\sqrt{s_{NN}}$=5.02 TeV.

Bibliography

[1] M. Riordan and W. A. Zajc, The first few microseconds, Sci. Am. 294N5, 24 (2006) [Spektrum Wiss. 2006 N11, 36 (2006)].

[2] D. J. Schwarz, Annalen Phys. 12, 220 (2003) [astro-ph/0303574].

[3] Dr. Gerald L. Schroeder, The Science of God, The Free Press, NY,NY 1997

[4] K. A. Olive, Nucl. Phys. B 190, 483 (1981).

[5] A. Pich, [arXiv:0705.4264 [hep-ph]].

[6] H. Fritzsch, M. Gell-Mann, eConfC720906V2:135-165, 1972. arXiv: hep-ph/0208010v1 (2002).

[7] J. Iliopoulos, doi:10.5170/CERN-2014-008.1 [arXiv:1305.6779 [hep-ph]].

[8] N. Bogolubov, B. Struminsky, A. Tavkhelidze. On composite models in the theory of elementary particles. JINR Preprint D-1968, Dubna 1965.

[9] Greenberg, O. W. (1964). "Spin and Unitary Spin Independence in a Paraquark Model of Baryons and Mesons". Phys. Rev. Lett. 13 (20): 598–602.

[10] Han, M. Y.; Nambu, Y. (1965). "Three-Triplet Model with Double SU(3) Symmetry". Phys. Rev. 139 (4B): B1006–B1010.

[11] D. Gross, Asymptotic freedom and QCD: A historical perspective, Nucl.Phys.Proc.Suppl. 135 (2004) 193211.

[12] D. J. Gross and F. Wilczek, Phys. Rev. Lett. **30** (1973), 1343-1346 doi:10.1103/PhysRevLett.30.1343

[13] H. D. Politzer, Phys. Rev. Lett. **30** (1973), 1346-1349 doi:10.1103/PhysRevLett.30.1346

[14] O. Philipsen, arXiv:0808.0672v1 [hep-ph]

[15] S. Gupta, J. Phys. G: Nucl. Part. Phys. 35 (2008) 104018.

[16] F. Karsch, E. Laermann and A. Peikert Nucl. Phys. B605 (2001) 579.

[17] T. Nayak and B. Sinha, doi:10.1007/978-81-8489-295-6_9 [arXiv:0904.3428 [nucl-ex]].

[18] F. Karsch and E. Laermann, [arXiv:hep-lat/0305025 [hep-lat]].

[19] T. K. Nayak, [arXiv:0804.1368 [nucl-ex]].

[20] Phases of nuclear matter https://pdfs.semanticscholar.org/246d/d4028e86528e4d27ba40f79838a100f85287.pdf

[21] F. Karsch, Lect. Notes Phys. **583** (2002), 209-249 doi:10.1007/3-540-45792-5_6 [arXiv:hep-lat/0106019 [hep-lat]].

[22] Bazavov, A.,et al.(HotQCD) (2014), Phys. Rev.D90(9),094503.

[23] Adam, J.,et al.(ALICE) (2016i), Phys. Rev.C94(3),034903.

[24] Chatrchyan, S.,et al.(CMS) (2012d), Phys. Rev. Lett.109,152303.

[25] Modelling Hadronic Matter 2016 J. Phys.: Conf. Ser. 706 032001

[26] R. P. Scharenberg, B. K. Srivastava, A. S. Hirsch and C. Pajares, Universe **4** (2018) no.9, 96

[27] Y. Aoki, Z. Fodor, S. D. Katz and K. K. Szabo, Phys. Lett. B **643** (2006), 46-54 doi:10.1016/j.physletb.2006.10.021 [arXiv:hep-lat/0609068 [hep-lat]].

[28] Y. Aoki, G. Endrodi, Z. Fodor, S. D. Katz and K. K. Szabo, Nature **443** (2006), 675-678 doi:10.1038/nature05120 [arXiv:hep-lat/0611014 [hep-lat]].

[29] S. Ejiri, Phys. Rev. D **78** (2008), 074507 doi:10.1103/PhysRevD.78.074507 [arXiv:0804.3227 [hep-lat]].

[30] Miller, M. L., K. Reygers, S. J. Sanders, and P. Steinberg(2007), Ann. Rev. Nucl. Part. Sci.57, 205.

[31] Iancu, E., A. Leonidov, and L. D. McLerran (2001), Nucl.Phys.A692, 583.

[32] Harris, J. W., and B. Muller (1996), Ann. Rev. Nucl. Part.Sci.46, 71.

[33] Adam, J.,et al.(ALICE) (2016j), Phys. Rev.C93(2),024917.

[34] Adams, J.,et al.(STAR) (2005b), Nucl. Phys.A757, 102.

[35] Fodor, Z., and S. D. Katz (2004), JHEP04, 050.

[36] Abelev, B.,et al.(ALICE) (2013b), Phys. Rev.C88, 044910.

[37] Adcox, K.,et al.(PHENIX) (2004), Phys. Rev.C69, 024904.

[38] Arsene, I.,et al.(BRAHMS) (2005b), Nucl. Phys.A757, 1.

[39] Back, B. B.,et al.(PHOBOS) (2007), Phys. Rev.C75,024910

[40] M. Kliemant, R. Sahoo, T. Schuster and R. Stock, Lect. Notes Phys. **785** (2010), 23-103 doi:10.1007/978-3-642-02286-9_2 [arXiv:0809.2482 [nucl-ex]].

[41] J. Adam *et al.* [ALICE], Phys. Lett. B **772** (2017), 567-577 doi:10.1016/j.physletb.2017.07.017

[42] J. Adam *et al.* [ALICE], Phys. Rev. Lett. **116** (2016) no.22, 222302 doi:10.1103/PhysRevLett.116.222302

[43] A. Mazeliauskas and V. Vislavicius, Phys. Rev. C **101** (2020) no.1, 014910 doi:10.1103/PhysRevC.101.014910 [arXiv:1907.11059 [hep-ph]].

[44] R. Nouicer, Eur. Phys. J. Plus **131** (2016) no.3, 70 doi:10.1140/epjp/i2016-16070-2 [arXiv:1512.08993 [nucl-ex]].

[45] Roland, G.; Safarik, K.; Steinberg, P. Heavy-ion collisions at the LHC.Prog. Part. Nucl. Phys.2014,77, 70–127

[46] S. Acharya *et al.* [ALICE], JHEP **11** (2018), 013 doi:10.1007/JHEP11(2018)013

[47] N. Armesto et al., e-Print: arXiv:0711.0974.

[48] P Huovinen 2017 J. Phys.: Conf. Ser.798 012063

[49] B. Alver, M. Baker, C. Loizides and P. Steinberg, [arXiv:0805.4411 [nucl-ex]].

[50] P. Huovinen, P. F. Kolb, U. W. Heinz, P. V. Ruuskanen and S. A. Voloshin, Phys. Lett. B **503** (2001), 58-64 doi:10.1016/S0370-2693(01)00219-2

[51] P. F. Kolb and U. W. Heinz, [arXiv:nucl-th/0305084 [nucl-th]].

[52] R. Snellings, New J. Phys. **13** (2011), 055008 doi:10.1088/1367-2630/13/5/055008 [arXiv:1102.3010 [nucl-ex]].

[53] Adcox, K.,et al.(PHENIX) (2005), Nucl. Phys.A757, 184.

[54] Back, B. B.,et al.(2005), Nucl. Phys.A757, 28.

[55] H. Niemi, G. S. Denicol, H. Holopainen and P. Huovinen, Phys. Rev. C **87** (2013) no.5, 054901 doi:10.1103/PhysRevC.87.054901

[56] L. Adamczyk *et al.* [STAR], Phys. Rev. Lett. **116** (2016) no.6, 062301 doi:10.1103/PhysRevLett.116.062301 [arXiv:1507.05247 [nucl-ex]].

[57] B. B. Abelev *et al.* [ALICE], JHEP **06** (2015), 190 doi:10.1007/JHEP06(2015)190 [arXiv:1405.4632 [nucl-ex]].

[58] J. Adam *et al.* [ALICE], Phys. Lett. B **754** (2016), 235-248 doi:10.1016/j.physletb.2016.01.020 [arXiv:1509.07324 [nucl-ex]].

[59] A. Adare *et al.* [PHENIX], Phys. Rev. C **91** (2015) no.6, 064904 doi:10.1103/PhysRevC.91.064904 [arXiv:1405.3940 [nucl-ex]].

[60] S. Afanasiev *et al.* [PHENIX], Phys. Rev. Lett. **109** (2012), 152302 doi:10.1103/PhysRevLett.109.152302

[61] Adare, A.,et al.(PHENIX) (2010a), Phys. Rev. Lett.104,132301.

[62] Adam, J.,et al.(ALICE) (2016g), Phys. Lett.B754, 23

[63] T. Matsui and H. Satz, Phys. Lett. B **178** (1986), 416-422 doi:10.1016/0370-2693(86)91404-8

[64] S. Acharya *et al.* [ALICE], Phys. Lett. B **805** (2020), 135434 doi:10.1016/j.physletb.2020.135434

[65] J. Rafelski and B. Muller, Phys. Rev. Lett. **48** (1982), 1066 [erratum: Phys. Rev. Lett. **56** (1986), 2334] doi:10.1103/PhysRevLett.48.1066

[66] J. Adam *et al.* [ALICE], Nature Phys. **13** (2017), 535-539 doi:10.1038/nphys4111 [arXiv:1606.07424 [nucl-ex]].

[67] C. Adler *et al.* [STAR], Phys. Rev. Lett. **89** (2002), 202301 doi:10.1103/PhysRevLett.89.202301

[68] M. Lv, Y. G. Ma, G. Q. Zhang, J. H. Chen and D. Q. Fang, Phys. Lett. B **733** (2014), 105-111 doi:10.1016/j.physletb.2014.04.025 [arXiv:1404.4394 [nucl-th]].

[69] B. Abelev *et al.* [ALICE], Phys. Rev. Lett. **110** (2013) no.8, 082302 doi:10.1103/PhysRevLett.110.082302

[70] J. Adams *et al.* [STAR], Phys. Rev. Lett. **97** (2006), 162301

[71] https://lphe.epfl.ch/seminar/extern/Marta_Verweij_02052016.pdf

[72] Nattrass, C., N. Sharma, J. Mazer, M. Stuart, and A. Be-jnood (2016), Phys. Rev.C94(1), 011901

[73] Adler, S.,et al.(PHENIX) (2006a), Phys.Rev.Lett.96,222301.

[74] Adam, J.,et al.(ALICE) (2015c), JHEP09, 170.

[75] R. J. Fries, B. Muller, C. Nonaka and S. A. Bass, J. Phys. G **30** (2004), S223-S228 doi:10.1088/0954-3899/30/1/025

[76] K. Adcoxet al.[PHENIX], Phys. Rev. Lett.88, 022301 (2002); C. Adleret al.[STAR],nucl-ex/0210033

[77] P. Sorensen [STAR], J. Phys. G **30** (2004), S217-S222 doi:10.1088/0954-3899/30/1/024 [arXiv:nucl-ex/0305008 [nucl-ex]].

[78] A. Ortiz Velasquez [BNL-Bielefeld-CCNU], Nucl. Phys. A **932** (2014), 146-151 doi:10.1016/j.nuclphysa.2014.07.034

[79] B. Abelev *et al.* [ALICE], Phys. Rev. Lett. **110** (2013) no.8, 082302 doi:10.1103/PhysRevLett.110.082302 [arXiv:1210.4520 [nucl-ex]].

[80] Casalderrey-Solana, J., D. Gulhan, G. Milhano, D. Pablos,and K. Rajagopal (2017), JHEP03, 135.

[81] S. Acharya *et al.* [ALICE], Phys. Rev. D **99** (2019) no.1, 012016 doi:10.1103/PhysRevD.99.012016 [arXiv:1809.03232 [nucl-ex]].

[82] G. Aad *et al.* [ATLAS], Phys. Lett. B **739** (2014), 320-342 doi:10.1016/j.physletb.2014.10.065 [arXiv:1406.2979 [hep-ex]].

[83] Cunqueiro, L. (ALICE) (2016),Proceedings, 25th Interna-tional Conference on Ultra-Relativistic Nucleus-NucleusCollisions (Quark Matter 2015): Kobe, Japan, September27-October 3, 2015, Nucl. Phys.A956, 593.

[84] S. Acharya *et al.* [ALICE], JHEP **10** (2018), 139 doi:10.1007/JHEP10(2018)139 [arXiv:1807.06854 [nucl-ex]].

[85] Chatrchyan, S.,et al.(CMS Collaboration) (2013a), Phys.Lett. B730(arXiv:1310.0878. CMS-HIN-12-002. CERN-PH-EP-2013-189), 243. 31 p.

[86] CMS Collaboration,"Performance of quark/gluon discrimination in 8 TeV pp data," CMS-PAS-JME-13-002

Chapter 2

A Large Ion Collider Experiment

An overview of the accelarating components at LHC is presented in this chapter with brief discussions on the ALICE detectors and sub-detectors that have been used in this analysis.

2.1 Large Hadron Collider

LHC is the largest particle accelerator in the world till date. The CERN accelerator complex is a set of accelerators that accelerates the particles to increasingly higher energies [1, 2, 3]. The function of the machines is to accelerate the beam to a certain energy, injects the beam into the next one which further increases the beam energy to a higher value and sends the beam to the next one and so on. LHC is the last element of this chain in which it has become possible to accelerate the proton beams to collide from opposite directions & provides maximum up to the centre of mass energy ($\sqrt{s_{NN}}$) of 13 TeV, Pb beams up to $\sqrt{s_{NN}}$ =5.02 TeV and recently the Xe beams upto $\sqrt{s_{NN}}$ = 5.44 TeV till now. Fig 2.1 shows the schematic diagram of the accelerator complex. The process of accelerating a beam, say, of protons is as follows. At first, electrons are stripped from the hydrogen atoms to obtain protons. Then, these are fed into the PS Booster (PSB) at 50 MeV energy from the LINear ACcelerator where they are accelerated further and sent to the next

	LINAC	PSB	PS	SPS	LHC
proton	50 MeV	1.4 GeV	25 GeV	450 GeV	7 TeV
Pb ions	4.2 MeV	72 MeV (LEIR)	5.9 GeV	177 GeV	2.76 TeV

Table 2.1: Different stages of acceleration of protons and leads

machine Proton Synchrotron (PS) at 1.4 GeV that subsequently accelerates them to 25 GeV. Then they enters the next element of the chain which is the Super Proton Synchrotron (SPS) where they reach the energy of 450 GeV and finally they are inserted to the LHC where they are accelerated to few TeV energy. The stored beams move in both clock-wise and anticlock-wise directions and circulate for hours in the beam pipes. Similarly, Pb ions are extracted from a pure vapourized sample of Lead and accelerated to 4.2 MeV per nucleon by passing through LINAC3. Then they are accelerated to 72 MeV per nucleon in Low Energy Ion Ring (LEIR). After that, they are transferred to PS which accelerates them to 5.9 GeV per nucleon and sent to SPS where it is fully stripped to Pb^{82+}. There, it acquires energy of 177 GeV per nucleon and are fed to LHC where they achieve the corresponding desired energies. The circumference of the Large Hadron Collider is 26.7 km. In LHC, the stored beams, travelling in opposite directions, collide at four interaction points where the two rings intersect. There are four big experiments situated at those points- ALICE, ATLAS, CMS and LHCb. Apart from that, there are three more smaller experiments- TOTEM next to CMS, LHCf next to ATLAS and MoEDAL next to LHCb [1].

Charged ions radiate when they are accelerated in a curved path or orbit. This is called Synchrotron radiation. The energy loss per turn by synchrotron radiation is inversely proportional to the fourth power of mass of the particle. So, the energy loss for protons is much lower than the electrons per turn since protons are about 2000 times heavier than electrons. Therefore, it is more effective to accelerate massive particles to obtain high energy collision than lighter ones. The LHC tunnel is built underground at a mean depth of 100 m because of several factors. First of all, it is less expensive to build a tunnel underground than to build at the surface by acquiring the land.

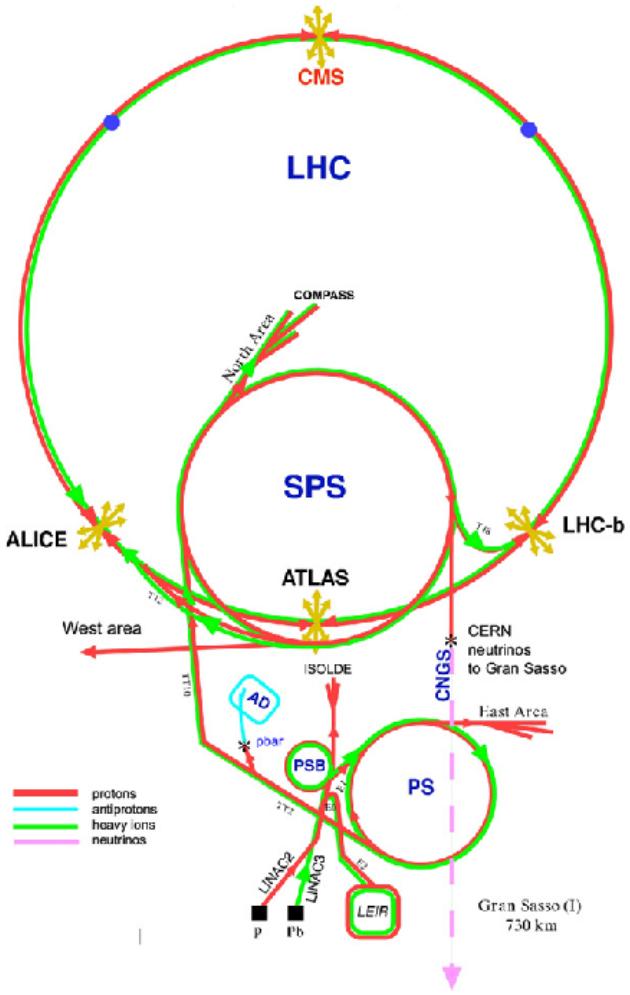

Figure 2.1: THE CERN accelerator complex consisting of accelerators LINAC, PS, PSB, LEIR, SPS and LHC and the experiments ALICE, CMS, ATLAS, LHCb

Also, the impact on the landscape is reduced and the earth crust serves as a good shield against radiation.

The primary goal of LHC is to produce and study the details of Higgs boson which is responsible for the mass of the elementary particles, understanding of the supersymmetry, dark matter and dark energy through the proton-proton collision and to study the properties of the matter existed in micro-second old universe called Quark-Gluon-Plasma through the heavy-ion collisions.

As per the present theories, after the creation of the Universe from the Big Bang, a phase existed where the matter was extremely hot and dense and composed of elementary building blocks of

matter-quark and gluons-called "Quark-Gluon-Plasma". As the Universe cooled, the quarks are combined to form hadrons which is known as the hadronization of quarks. The LHC can produce the deconfined state of quarks and gluons by colliding heavy ions at extremely high energy. Finally, the particles produced in the collisions, hadrons, leptons and photons, reach the detectors and can be detected to study the properties of QGP.

The LHC is not a perfect circle. It consists of dipole bending magnets which bend the beam particles to keep them in their nearly circular orbits, quadrupole magnets which focus the beam to a very narrow region and accelerating RF cavities that accelerate particles and keep them at a constant energy. LHC uses (10^{-13} atm) ultrahigh vacuum to avoid collisions of beams with gas molecules. The particles circulate in the ring in the form of bunches. Each bunch of protons or Pb ions, as it circulates around the LHC, gets squeezed to about 16 μm near the interaction points to increase the collision probability and then expanded to 1 mm far from the interaction zone.

2.1.1 Beam parameters

The event rate (R) is related to the interaction cross-section (σ) of a process by, R = L $\times$ σ, where L is the luminosity. The reaction rate of a process depends on the instantaneous luminosity, luminosity depends on the number of particles in each bunch, the frequency of complete turns around the ring, the number of bunches and the beam cross-section. As discussed earlier, to increase the collision rate, bunch size is squeezed to about 20 μm near the collision point [4]. Luminosity in a machine can be increased by increasing the number of bunches. Each beam contains nearly 3000 bunches of particles with a bunch spacing of 25 nsec and each bunch contains almost 100 billion particles. When the bunches cross each other, there are about 40 collisions. Bunches cross about 30 million times/second resulting in almost 1 billion collisions/second in LHC [1]. The designed luminosity for pp collisions is of the order of $10^{34} cm^{-2} s^{-1}$ but ALICE operates

around $10^{30} cm^{-2} s^{-1}$. In 2010 and 2011, the highest luminosity achieved in ALICE with Pb ions are of the order 10^{25} and 10^{26} $cm^{-2} s^{-1}$ respectively.

2.2 ALICE detectors

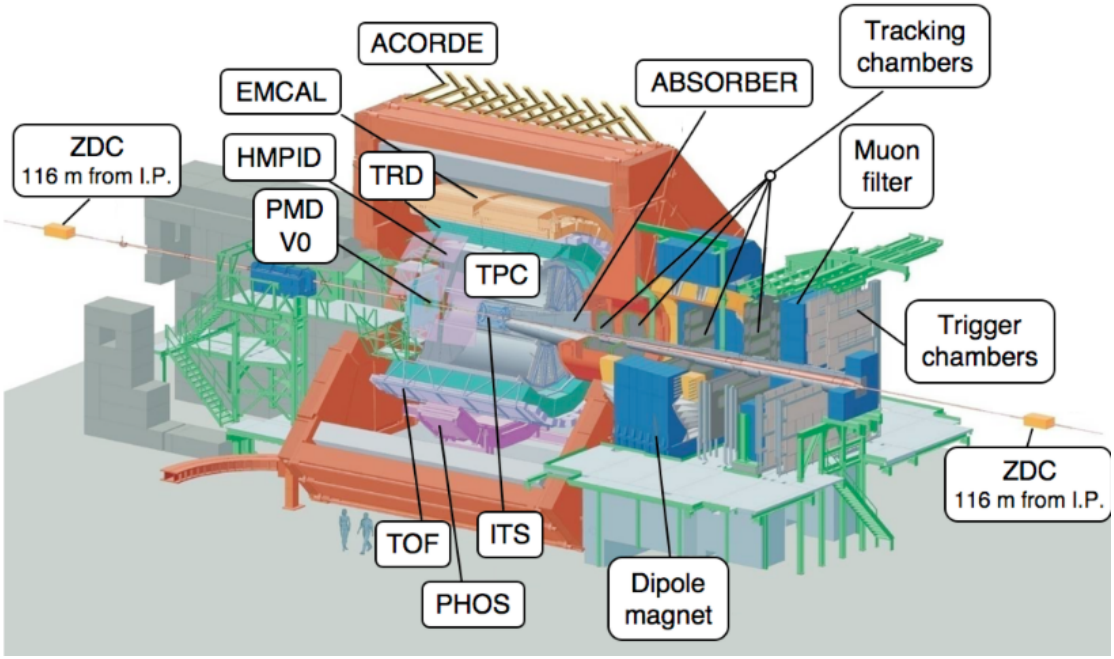

Figure 2.2: ALICE detector layout showing all the sub-detectors

The primary goal of ALICE is to form and probe the properties of a state of deconfined quarks and gluons called Quark-Gluon Plasma by colliding heavy ions at high temperatures and energy densities that is predicted to have existed a micro-second after the Big Bang, before the atoms and molecules were formed. In such collisions, several thousands of particles are produced. For this, high-granularity detectors, like the Time Projection Chamber and the Silicon Drift Detectors are used. One of the primary requirements for such a heavy-ion collision experiment is to have a tracking system with a large acceptance and efficiency that can track the particles produced in the collisions. Also, detectors are needed to identify particles in a wide momentum range. An efficient online trigger system is also essential. Tracking is done in ALICE using three-dimensional

hit information in the detectors in a magnetic field. A low magnetic field is preferred to allow the reconstruction of low-p_T particles. ALICE uses magnetic field of 0.5 T to guarantee a good momentum resolution at high momenta as well as reconstruction of low momenta particles. ALICE collects data with the collisions of proton-proton, proton-lead, lead-lead, Xe-Xe at $\sqrt{s_{NN}}$ upto a few TeV. The weight of ALICE is about 10000 tonne and size is about 26 m $\times$ 16 m $\times$ 16 m. ALICE can measure particles in a wide range of momentum from 100 MeV/c to 10 GeV/c.

Fig 2.2 shows the layout of the ALICE experiment. It has a central barrel system and several forward detectors. The central system is placed in a magnetic field of about 0.5 T. It consists of the Inner Tracking System (ITS) for tracking and vertex determination, the main tracking detector Time Projection Chamber (TPC), the Transition Radiation Detector (TRD) to identify electrons and the Time Of Flight detector (TOF) to identify and track the particles are having full azimuthal coverage at mid rapidity $|\eta| \leq 0.9$ and the High-Momentum Particle Identification Detector (HMPID) to identify particles in high p_T range, the Photon Spectrometer (PHOS) which is an electromagnetic calorimeter to detect direct photons and the Electromagnetic Calorimeter (EMCal) to detect photons and electrons. These detectors have smaller acceptance in both pseudorapidity and azimuthal angle. The forward detector system covering forward pseudorapidity consists of the Muon Spectrometer, the Forward Multiplicity Detector (FMD), Photon Multiplicity Detector (PMD) and the Zero Degree Calorimeter (ZDC). There are two trigger detectors located on each side of the interaction point: the scintillator detector V0 and the cherenkov counter T0. The ALICE experiment also includes a dedicated detector ACORDE to study the high-energy cosmic ray showers and the nature of primary cosmic rays.

The ALICE detectors have been described in detail in the subsequent sections.

2.3 The Central Barrel Detectors

The central part of ALICE contains Inner Tracking System (ITS), Time Projection Chamber (TPC), Transition Radiation Detector (TRD), Time Of Flight (TOF), PHOton Spectrometer (PHOS), Electromagnetic Calorimeter (EMCal) and High Momentum Particle Identification Detector (HMPID). ITS, TPC, TRD and TOF have full azimuthal coverage at mid rapidity ($|\eta| < 0.9$), the rest of the detectors are of limited coverage. In this analysis, substructure of only charged jets are studied. Jets are reconstructed with jet algorithm and the charged constituents of jets are selected using TPC. For full jet reconstruction, apart from TPC, the EMCal and PHOS are needed to detect the neutral components of jets.

2.3.1 Inner Tracking System

ITS is the tracking detector closest to the collision point having six cylindrical layers placed coaxially around the beam pipe as shown in Fig 2.3. To handle a very high track density, up to $90/cm^2$, high granularity Silicon-pixels are used in the inner most layers of ITS to provide very good position and momentum resolutions.

ITS is designed to be capable of handling a maximum of 8000 tracks per unit rapidity. The spatial resolution of ITS is of the order of a few tens of μm.[5] The primary functions of ITS are to reconstruct primary vertex using the first two layers of ITS, to find the secondary vertex for hyperons, B, D mesons, to identify particles of low momentum via energy loss measurement (< 1 GeV) in non-relativistic region using the next four layers, to perform tracking in the standalone mode of low p_T particles and with TPC, to improve the momentum resolution of TPC tracks, providing good position as well as energy momentum resolution. ITS has six cylindrical layers of silicon detectors - two Silicon Pixel Detector (SPD), two Silicon Drift Detectors (SDD) and two Silicon Strip Detectors (SSD). Except the two innermost SPD, all the layers have analogous readout to

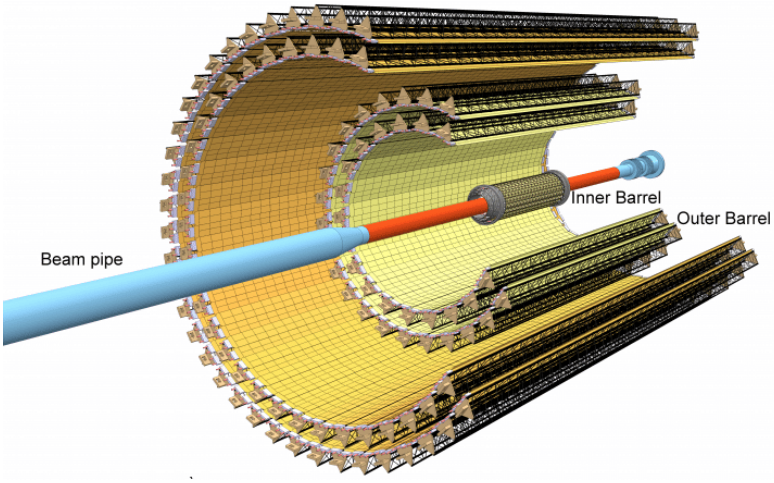

Figure 2.3: ITS detector of ALICE with its six layers

	SPD	SDD	SSD
Inner radius(cm)	3.9	14.9	38.5
Outer radius(cm)	7.6	23.8	43.6
η-coverage	$\|\eta\| < 1.75$	$\|\eta\| < 0.9$	$\|\eta\|$ <1.0
Resolution(μm)	12 (r-ϕ) & 100 (z)	38 (r-ϕ) & 28 (z)	20 (r-ϕ) & 830 (z)

Table 2.2: Details of the ITS layers

identify particles via energy loss measurement. The low momentum particles can be detected by ITS only. SPD covers the pseudo-rapidity range $|\eta| < 1.75$, SDD and SSD cover $|\eta| < 1.0$ and $|\eta| < 0.9$ respectively.

Silicon Pixel Detector: The coverage of these two layers is $|\eta| < 1.75$ and it is placed at radius R=3.9 to 7.6 cm respectively. It is a highly granular layer with spatial resolution of maximum 12 μm in r-ϕ and 100 μm in the z-direction. SPD helps to measure the primary vertex precisely and reconstruct the secondary vertex.

Silicon Drift Detector: The two middle layers of ITS are SDD with coverage $|\eta| < 0.9$ and radius R=14.9 to 23.8 cm from the beam pipe. This is used for particle identification using specific energy loss (dE/dx) and tracking of the tracks passing through it. It uses drift time of electrons to find the position of track hits and the z-position of the hits are determined from the centroid of the charge accumulated in the anodes. It has position resolution of 38 μm in r-ϕ and 28 μm in z.

Silicon Strip Detector: These are the last two layers of ITS used for particle identification and tracking. It covers $|\eta|$ <1.0 and is located at radius R=38.5 and 43.6 cm respectively. It has spatial resolution of 20 μm in r-ϕ and 830 μm in Z. This layer is important for TPC-ITS track matching.

Performance of ITS:

Primary vertex reconstruction: The high track density in SPD is advantageous to determine the z-coordinate of the vertex with a precision of about 10 μm by combining the hits in the two pixel layers. For pp collisions it is around 90 μm. The interaction vertex is a space point where maximum number of tracklets converge. Each cluster on layer 1 is connected to all clusters on layer 2 of SPD within a window $\delta\phi < 0.5$ rad by a line in z,r, thereby forming tracklets. At $r = 0$, DCA between the tracklet and nominal beam position is calculated for all such tracklets. The position of the maximum in the z-distribution of DCA is considered as the preliminary vertex. x,y position of vertex is determined from the centre of beam spot averaged over many events and resolution is given by the size of the beam spot. For N tracklets, vertex resolution $\propto 1/\sqrt{N}$, N $\propto dN_{ch}/d\eta$.

Tracking: The tracking is performed using Kalman filter inward-outward-inward algorithm. Track seeds, built using the TPC clusters and the preliminary vertex at the outer radius of TPC, are propagated inward and at each step, nearest found clusters are associated to them. Only the tracks having $>$ 20 clusters in the outer volume, are propagated to the inner TPC region. The reconstructed TPC tracks are extrapolated to the ITS outermost layer and become its seed which is propagated inward and updated at each ITS layer similar to TPC. The reconstruction efficiency in TPC for low p_T particles is very poor. For this, Standalone ITS reconstruction is done with the clusters leftover by TPC+ITS. Tracks reconstructed in ITS are extrapolated to their point of closest approach (PCA) to preliminary determined vertex. Then they are propagated outward using

the clusters found at previous stage. Tracks reaching TOF are matched with the TOF clusters. Similarly track matching is performed with TRD, EMCal, PHOS, HMPID and re-fitted. Also, the expected time of flight for different particles are updated to identify particles using TOF. Again the tracks are propagated inwards and re-fitted, thus, the position, direction, curvature etc. of the tracks are determined. The reconstructed tracks in TPC and ITS are used to find vertex more precisely than the SPD tracklets alone. The tracks reconstructed in TPC and ITS are extrapolated to the PCA to the nominal beam line and far outliers are removed. Thus the precise vertex is determined.

Secondary vertex reconstruction: The secondary vertex reconstruction is shown in Fig 2.4. The

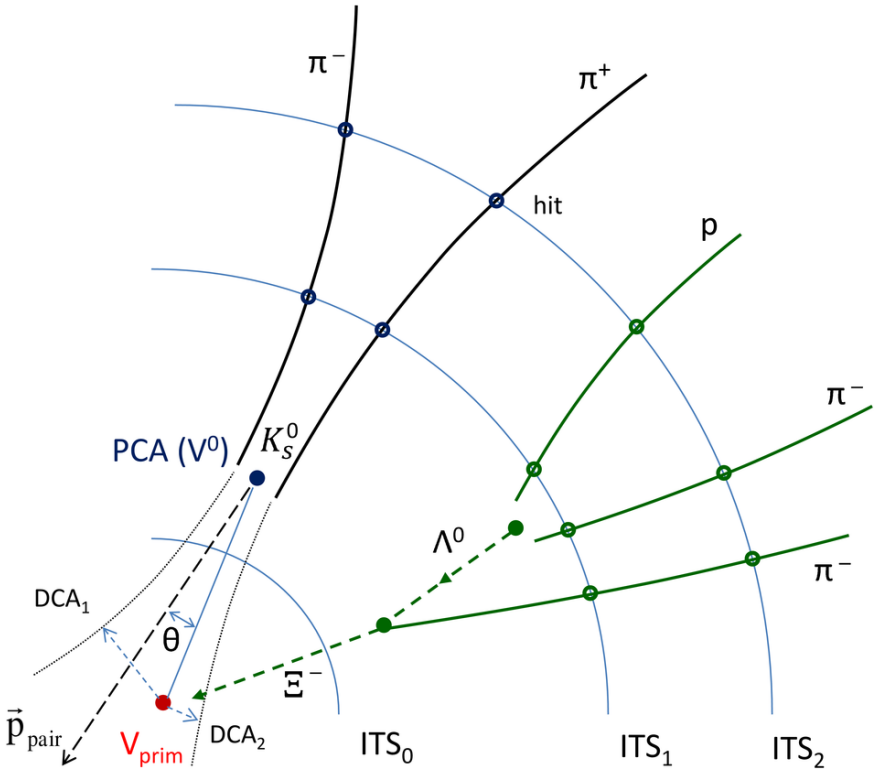

Figure 2.4: Secondary vertex reconstruction using ITS

tracks with DCA (distance of closest approach of the track) to the interaction vertex > a specific value are selected. For each unlike-sign pair of such tracks, PCA between the two tracks is calculated. PCA is the point where the two tracks are closest to each other. Then the following cuts are

checked: Distance between two tracks at PCA < 1.5 cm, PCA should be closer to the interaction vertex than the innermost hit of either of the two tracks, $cos\theta$ between the total momentum vector of the track pair and the line connecting the primary and secondary vertices must be> 0.9

Particle identification: ITS allows hadron separation below 100 MeV/c. dE/dx is measured from the analog readout of the electronic signals produced in SDD and SSD resulting in good π-K separation upto 0.5 GeV/c and good π-p and p-K separation upto 1 GeV/c.

ALICE is also going through an upgrade of ITS, the main goal of the detector upgrade is to handle the collision rate of 50 kHz in Pb–Pb collisions. The current ITS detector has some limitations [6], though the precision of ITS to determine the DCA is sufficient for the study of production of charm mesons above $p_T > 1$ GeV/c, it is insufficient at lower p_T. Also, the proper decay length of the charm baryon is about 60 μm which is lower than the impact parameter resolution of the present ITS. Therefore currently, charm baryons cannot be measured by ALICE in central PbPb collisions. Also, it has a limited read-out rate capabilities of maximum rate of 1 kHz which is not sufficient to fulfil the required rate capabilities. The main aim of the ITS upgrade includes heavy flavour measurements like, R_{AA} and v_2 measurement of B,D mesons, Λ baryons, D meson production within jets and its fragmentation functions etc. Apart from that, the reduced material thickness and the efficient tracking and read-out capabilities of the upgraded ITS is expected to help in the detailed measurement of low-mass dielectrons. In short, the goal of ITS upgrade includes highly improved tracking in standalone mode and with TPC over a wide range of momentum specially in low momentum and precise secondary vertex reconstruction from the decay of charm and beauty hadrons. The upgraded detector is designed to consist of seven concentric cylindrical layers having radial extension from 22 mm to 430 mm with respect to the beamline. The data handling capacity of the upgraded detector is expected to be at a rate of 100 kHz and 400 kHz for Pb+Pb and pp collisions respectively [6].

2.3.2 Time Projection Chamber

TPC is the main tracking detector in ALICE that surrounds ITS [7] as shown in Fig 2.5. It is used to identify charged particles by measuring their momentum & dE/dx and to determine the vertex of the colision along with ITS, TOF and TRD thereby providing a good momentum resolution, two track separation and dE/dx resolution for p_T < 10GeV/c. The acceptance of TPC is $|\eta|$ <0.9 which is important for event-by-event fluctuation study of the hadronic observables. The inner and outer radii of TPC are about 80 cm and 250 cm respectively and the overall length in the beam direction is 500 cm. TPC provides a large volume of 88 m^3 filled with gas 90% Ne,10% CO2 and N_2. The TPC field cage provides a highly uniform electric field in the cylindrical volume so that the primary charged particles can be transported to the read-out end plates by going a long distance of ≈ 2.5 m. Due to the symmetry in particle production in a collider experiment, two such back-to-back field configurations are chosen in the same volume, having a common high-voltage electrode at the axial centre of the cylinder. The potential, developed between a central electrode and the two end plates is required to drift the particles. Due to the gas mixture in the TPC and the required high rate capability, a uniform drift field of about 400 V/cm is developed which causes the high voltage at central electrode as high as 100 kV causing a maximum drift time of about 90 μs. The readout chambers on the two end plates are multiwire proportional counters with cathode pad readout. There are 570132 pads in the the multiwire proportional chambers located at the TPC end plates. In TPC upgrade, MWPC are being replaced by the GEM chambers and they can handle Pb-Pb interaction rate up to 50 kHz. The data collection rate of the upgraded TPC is expected to increase by a factor of about 100 in the high-luminosity environment. Choice of the gas mixture is optimized to ensure good momentum resolution, high rate handling capability,low space charge effect and low scattering. Since the medium is gaseous, there is low multiple scattering due to large radiation length. Charged particles pass through the gas volume and ionise the

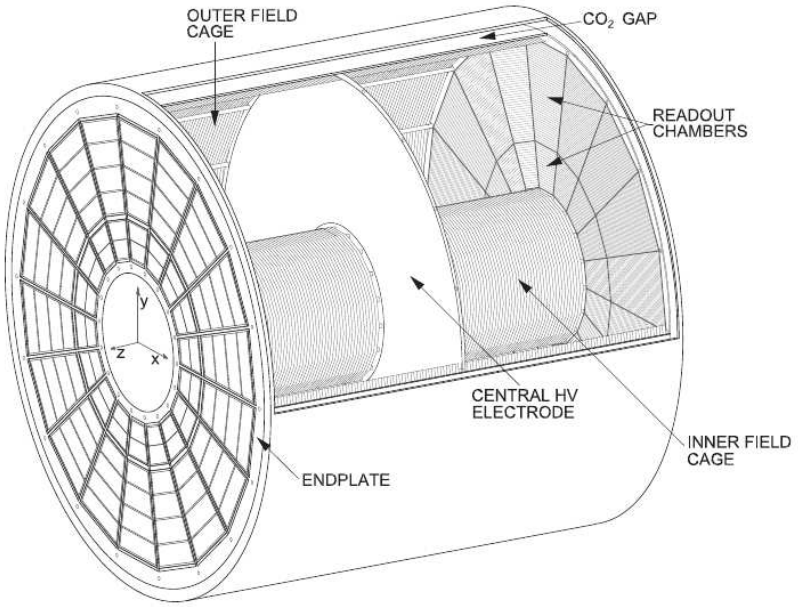

Figure 2.5: Schematic layout of the ALICE Time Projection chamber (TPC)

gas and the liberated electrons drift towards the end plates with drift velocity $\approx$ 2.7 cm/s and hit the readout pads. Under the influence of magnetic field, depending on the charge and momentum, the particles bend in helical path. Since, there are 159 pad rows, a track of a particle can have maximum 159 clusters in the TPC volume. From the radius of curvature of the track and magnetic field, the momentum of the particle can be determined. The (x,y) coordinates are determined by the hits in MWPC pads at the end plates and z coordinate is determined by calculating the arrival time of the signal with respect to collision time of the beams. The detector's position resolution is about 800-1100 μm and 1100-1250 μm in the r-ϕ plane and z-direction. From the measurement of the particle momentum and the specific energy loss $< dE/dx >$ which is measured by the charge collected from readout pads, the particle can be identified from Bethe-Bloch formula as shown in Fig 2.6. The separation of the charge particles upto p_T= 1 GeV/c using dE/dx measuremt is possible in the TPC. The momentum resolution varies from 2% to 20% for tracks of p_T from 100 MeV/c to 100 GeV/c for TPC alone and with other detectors, TPC provides better momentum resolution up to 10% for tracks up to 100 GeV/c. For good dE/dx resolution, particle identification

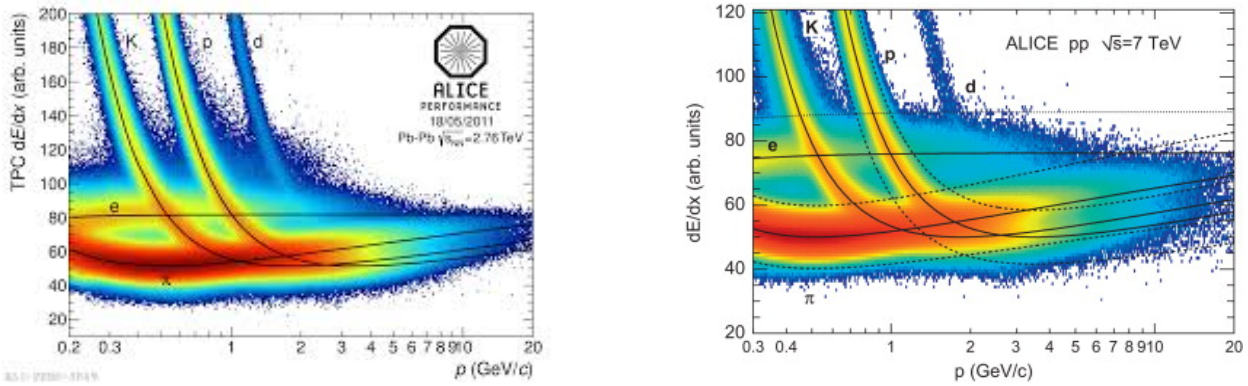

Figure 2.6: Particle Identification using energy loss. Black line represents the Bethe-bloch curve for different particles. If the dE/dx of a track with a certain p is close to the dE/dx of a particular species obtained from Bethe curve at the same p, that track is identified as that species.

is possible down to $p_T = 0.3$ GeV/c.

2.3.3 Time Of Flight (TOF)

TOF is used for particle Identification up to a higher p_T range than with TPC alone by measuring the particle velocity from their time of flight measurement, in the intermediate p_T range [8, 9]. To measure the time of flight, it needs a start time t0 and a stop time t. Therefore, the velocity of the particle is given by, v= l / (t-t0) or β = l / c(t-t0), l is the known track length. Knowing the momentum p of the particle from TPC, one can determine its mass and thus one can identify the particle by :$m = p\sqrt{\frac{t^2}{l^2} - 1} = p\sqrt{\frac{1}{\beta^2} - 1}$, t is the time of flight. The start time is provided by the T0 detector or it can be estimated using the particle arrival times at the TOF detector. The particle identification process is shown in Fig 2.7. TOF provides PID upto 2.5 GeV/c for π/K & upto 4 GeV/c for protons which is not achievable by the TPC alone. TOF in ALICE is a large area Multi-gap Resistive Plate Chamber (MRPC) located just around TRD. Gas detector is the only choice to cover a large area of about 141 m^2.The mass resolution has three contributions: $\delta m/m = \delta p/p, \delta m/m = (E/m)^2 \delta l/l$, and $\delta m/m = (E/m)^2 \delta t/t$. For high momentum, only the

errors in time of flight and track length dominate. Therefore, the time resolution must be good. The MRPC used here has a time resolution ≈ 80 ps, better than Scintillator (≈100 ps). The dis-

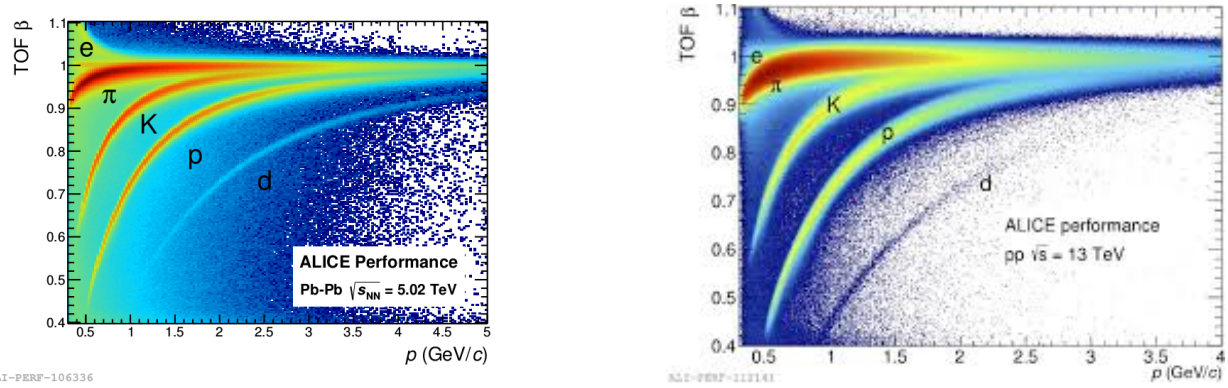

Figure 2.7: ALICE Time-Of-Flight technique: particle momentum vs velocity of the particles obtained from TOF

tribution is cleaner in p-p than Pb-Pb. The background is due to the tracks incorrectly matched to TOF. This background does not affect the TOF resolution. The number of standard deviation in time of flight difference $n\sigma = \frac{t_2 - t_1}{\delta t}$ is used to identify particles, where δt is the intrinsic time resolution. TOF has the inner and outer radii of 370 cm and 399 cm from the beam axis respectively and it covers a full azimuth at mid rapidity $|\eta|$ <0.9. The overall time resolution of TOF is given by, $\sigma_{TOF} = \sqrt{\sigma^2_{intrinsic} + \sigma^2_{t0}}$, where the last term is the resolution in initial time from the T0 detector.

2.3.4 Electromagnetic Calorimeter

The primary goal of using the EMCal in ALICE is to study the jet quenching effect and full jet reconstruction. It extends the p_T range for jets, direct photons and electrons from heavy-flavor decays. Calorimeters measure energy of particles by measuring the energy deposited by them in the material. EMCal detects electrons and photons that interact via electromagnetic interaction. The strongly interacting particles can be detected using Hadronic Calorimeter as they begin to lose energy in EMCal but are stopped in HCal (Hadronic Calorimeter). The main property of a

calorimeter is that it can detect neutral particles like neutrons and photons also by the energy deposition which cannot be detected in a tracking detectors like TPC. The particle identification using EMCal is illustrated in Fig 2.8. It detects the electromagnetic components of jets, electrons

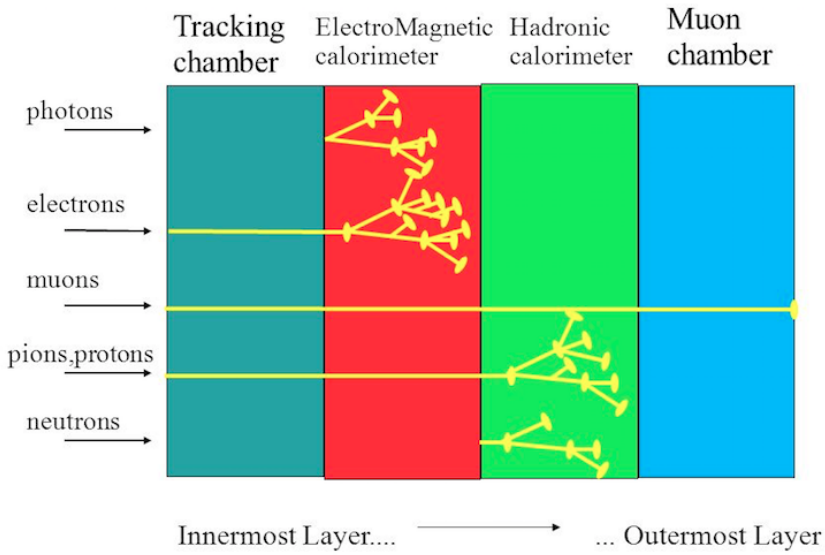

Figure 2.8: Particle identification using ALICE EMCal where the EM particles produce showers & get stopped and hadrons mostly pass through the region.

from heavy flavour decay and photons. EMCal is a sampling calorimeter consisting of active layers of scintillator material and absorbing layers of high density materials (lead). The absorbing layers stopped the particles whereas, the active layers produce the signals. EMCal covers $|\eta| < 0.7$ and $80^o < \phi < 187^o$ and it has depth of $20X_0$ [10]. The distance of this detector from the interaction point is 428 cm. One of the goals of EMCal is to measure neutral energy of jets. With the help of this, full jet spectra can be measured in different systems, as the charged components are detected by TPC. It can perform γ/π^0 discrimination up to 30 GeV/c, electron/hadron separation for momenta larger than 10 GeV/c.

2.3.5 Photon Spectrometer (PHOS)

PHOS is a high resolution, high granularity homogeneous electromagnetic calorimeter based on scintillating PbWO_4 crystal to detect photons, covering the range from thermal raditaion to hard processes in a wide range up to 100 GeV/c and reconstruct neutral mesons decaying to photons as shown in Fig 2.9. It can detect the photons directly coming from the interaction point and its main goal is to separate the direct photons from the decaying photons. The acceptance of this detector is $|\eta| < 0.12$ and $250< \phi <320^o$. The distance from IP is 460 cm [11] and it is made of dense scintillating crystals ($PbW0_4$) to bear the large particle density. A set of multiwire chambers in front of the PHOS helps to separate the charged particles from photons.

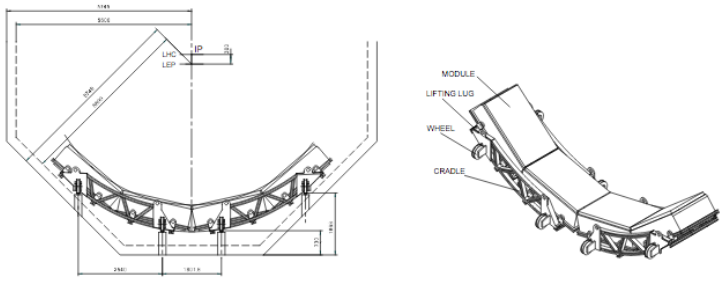

(a) PHOS xy-projection (b) PHOS axonometric projection

Figure 2.9: Schematic layout of Photon Spectrometer with coverage $|\eta| < 0.12$ and $250< \phi <320^o$

2.3.6 Transition Radiation Detector (TRD)

Transition radiation is a radiation emitted by a relativistic charged particle traversing through an inhomogeneous medium like a boundary between two different materials with different electrical properties and it is in proportion to its energy [1]. By this way, it can distinguish the particles from each other. TRD is the main detector for electron detection of momentum above 1 GeV/c which is not accessible by the TPC through the ionization energy loss measurement for the discrimination of electrons from hadrons. The low p_T (<1 GeV/c) electrons can be identified by measuring the

specific energy loss dE/dx in the TPC. This is necessary for measuring the production of J/ψ and Y in their dielectron channel. Also, with the help of the TRD along with the ITS, mesons with open charm and open beauty via their semi-leptonic decays can be studied. It provides good electron-pion separation for momenta $1 \leq p \leq 100$ GeV/c. ALICE TRD is part of the ALICE central barrel having full ϕ coverage and -0.84 $\leq \eta \leq$ 0.84. It is placed at a radial distance from 290 cm to 368 cm from the beam axis. The TRD consists of a radiator and a drift chamber filled with a mixture of Xe/CO2(85/15) [10].

2.3.7 High Momentum Particle IDentification (HMPID)

HMPID is basically a Ring Imaging Cherenkov counter with a liquid C_6F_{14} radiator and a CsI photo-cathode as shown in Fig 2.10. Under certain conditions, particles passing through a medium above a certain velocity excite the medium and it emits 'Cherenkov light', named after the discoverer of this phenomenon. The photons are emitted at an angle that depends on the velocity of the particle [1, 10]. From the meaasurement of the velocity by detecting the light and the momentum information of the particle from TPC, the mass and therefore the type of the particle can be determined. The main challenge is that the number of emitted photons is very less. A photon incident on the CsI surface will produce an electron with high probability of getting detected. It makes it possible to measure particles beyond the momentum range allowed by ITS, TPC and TOF. With HMPID, it is possible to separate π/K up to 3 GeV/c and π/p up to 5 GeV/c.

The particle identification ranges of different detectors are shown in Fig 2.11.

2.3.8 ALICE COsmic Ray DEtector (ACORDE)

The ACORDE is scintillator counters placed on the upper surface of the L3 magnet [1] with the acceptance of $|\eta| \leq$1.3 and $|\phi| < 60^0$. Single atmospheric muons and muti-muon events are

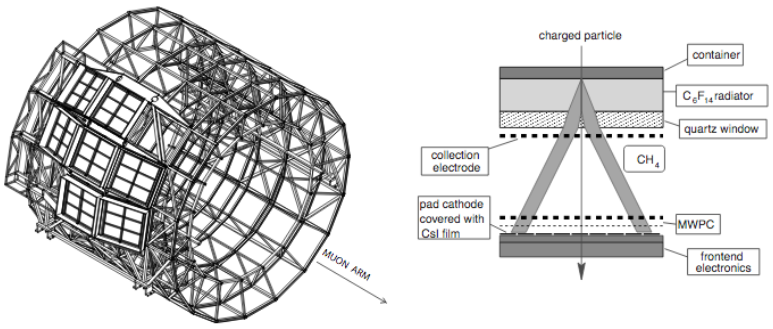

Figure 2.10: Layout & working principle of HMPID in ALICE

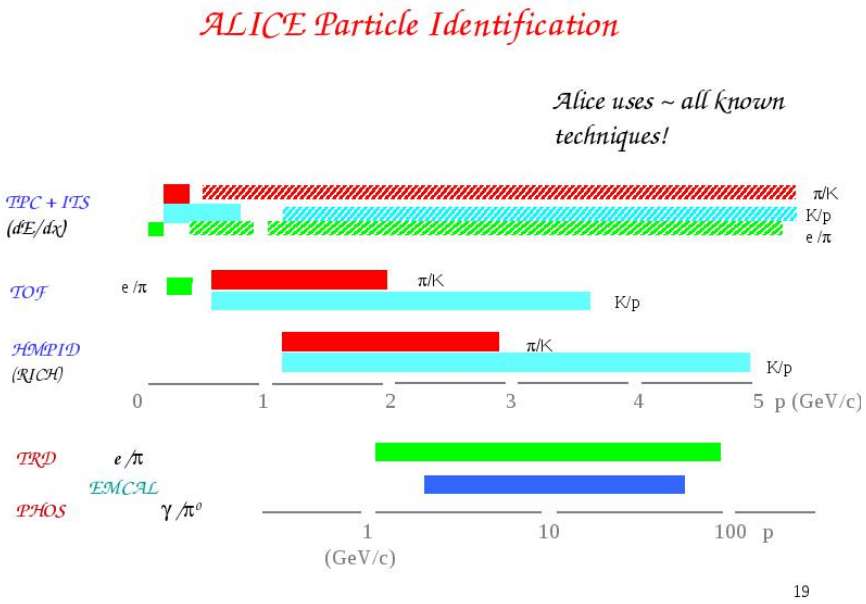

Figure 2.11: Particle identification in ALICE

identified using ACORDE together with the TPC, TRD and TOF. When atmospheric muons hit the detectors, the ACORDE supplies a fast L0 trigger. For the calibration, alignment and performance of ALICE tracking detectors, the signal is required.

2.4 The Forward detectors

Photon Multiplicity Detector (PMD), Forward Multiplicity Detector (FMD), Cherenkov detector T0, Scintillator detector V0 and Zero Degree Calorimeter (ZDC) are the forward detectors

in ALICE [11]. Their main purpose is to provide Level-0 trigger and multiplicity information in forward/backward region. FMD, T0 and V0 are located on both sides of Interaction Point.

2.4.1 T0 detector

The two T0 detectors -T0A and T0C, consisting of Cherenkov radiators are placed on the opposite sides of the Interaction Point (IP). T0C is placed at 70 cm from IP and T0A is placed at 360 cm from IP. The main goal of T0 is to supply fast timing signals for the L0 trigger, to give a wake-up call for TRD and to provide start time or collision time for TOF for particle identification. T0 has $|\eta|$ acceptance of 3.3 to 2.9 & 4.5 to 5 and it has a timing resolution better than 50 ps. The first trigger function is very important to discriminate beam–gas interactions. With this time resolution, $\pm$1.5 cm accuracy in vertex determination is obtained. If the vertex position lies within the pre–defined values, an L0 trigger signal known as T0–vertex will be generated. The T0 signal must correspond to the real time of the collision and it has to be independent of the vertex position. Cherenkov detectors with quartz radiators are chosen because fast scintillators may not survive for long under heavy dose of radiation and quartz is radiation hard. Also, it has very fast light emission compared to other fast scintillators. T0 detector layout is shown in Fig 2.12.

2.4.2 Forward Multiplicity Detector (FMD)

The primary function of the FMD is to measure the multiplicity of charged particles in the pseudorapidity acceptance $-3.4 < \eta < -1.7$ & $1.7 < \eta < 5.0$. This detector helps to extend the coverage of η of multiplicity measurements, to study event-by-event multiplicity fluctuations and to perform flow analyses.

2.4.3 V0 detector

It is the basic detector to estimate the centrality of a collision. Since the deposited energy in the V0 detectors is directly proportional to the number of primary particles generated in the collision, so the centrality of a collision can be obtained from this. Two scintillating V0 detectors - V0A and V0C are placed at a distance of 340 cm and 90 mm from IP respectively on both sides of IP having pseudo-rapidity coverages V0A ($2.8 > \eta > 5.1$) and V0C ($-3.7 < \eta < -1.7$). V0 mainly provides online L0 centrality trigger. It provides minimum bias trigger for central barrel detectors in pp and ion-ion collisions. Minimum bias trigger requires the condition of at least one particle hit on V0A or V0C or on both V0A & V0C. The trigger efficiency would be more with only V0A or V0C but due to background of interaction of beam with the residual gas of beam pipe, it is not advantageous. V0 can separate the background particles from those coming from real collisions by using the time of flight of particles detected by each V0. There is a difference of about 6 ns between real events and events associated to beam gas interactions. The mean number of hits are 10-20 for rings of V0C and somewhat smaller for V0A. The number of charged particles emitted inside the acceptance angles of the V0A and V0C rings are about 1000-1600 and 1400-1800 respectively. To identify a beam-beam collision, the event should occur on both V0A and V0C at the expected time i.e. 11 ns after the collision on V0A and 3 ns after the collision on V0C. The separation of real events from beam gas interactions using V0 detector is shown in Fig 2.13. The V0 provides centrality measurement based on the energy deposited in the scintillators. The centrality estimation using V0 detectors is shown in Fig 2.14. The relation between the number of primary charged particles emitted into the corresponding pseudorapidity range and the total charge collected inside a V0 ring was extracted. In 2009 and 2010 pp data taking periods, the minimum bias trigger requires a hit in either of the V0s or in the SPD. In 2011 and 2012, the trigger condition was changed to a requirement of hits in both V0s and any other detector triggering as

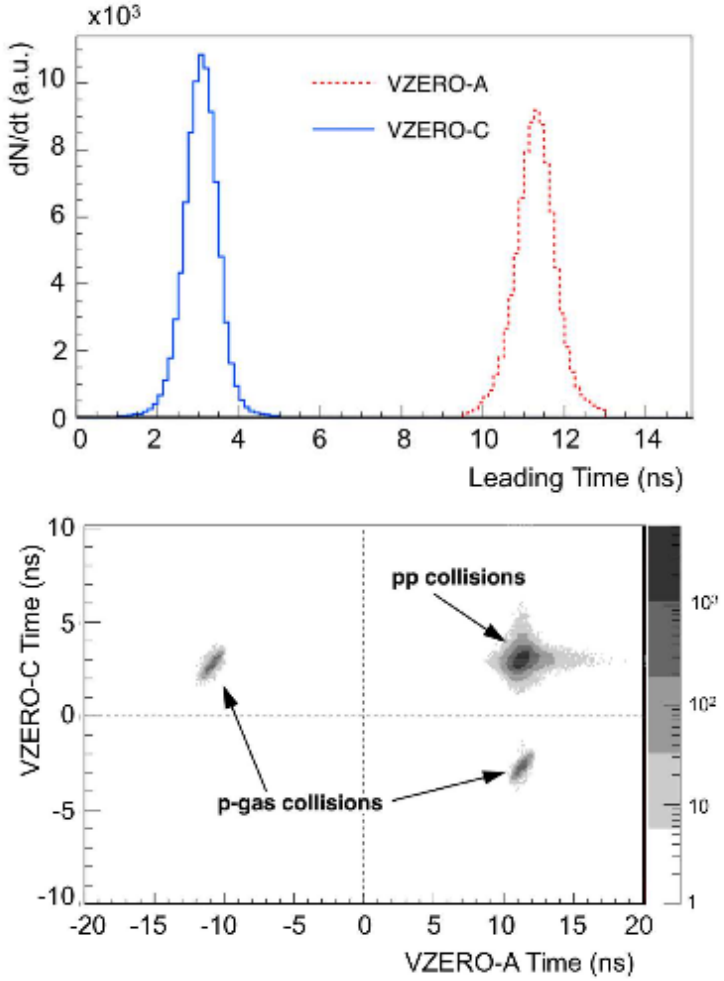

Figure 2.12: Distinguishing real events from beam gas interaction using V0 detector

the luminosity and beam background increased in LHC for pp collision. In Pb–Pb collisions, at least two out of the three conditions are to be satisfied and those are: (a) a signal in V0A, (b) a signal in V0C (c) two hits in the SPD outer layer. Later in 2010, the MB trigger was restricted to the coincidence between SPD and both V0s with the increase in luminosity during Pb–Pb data taking.

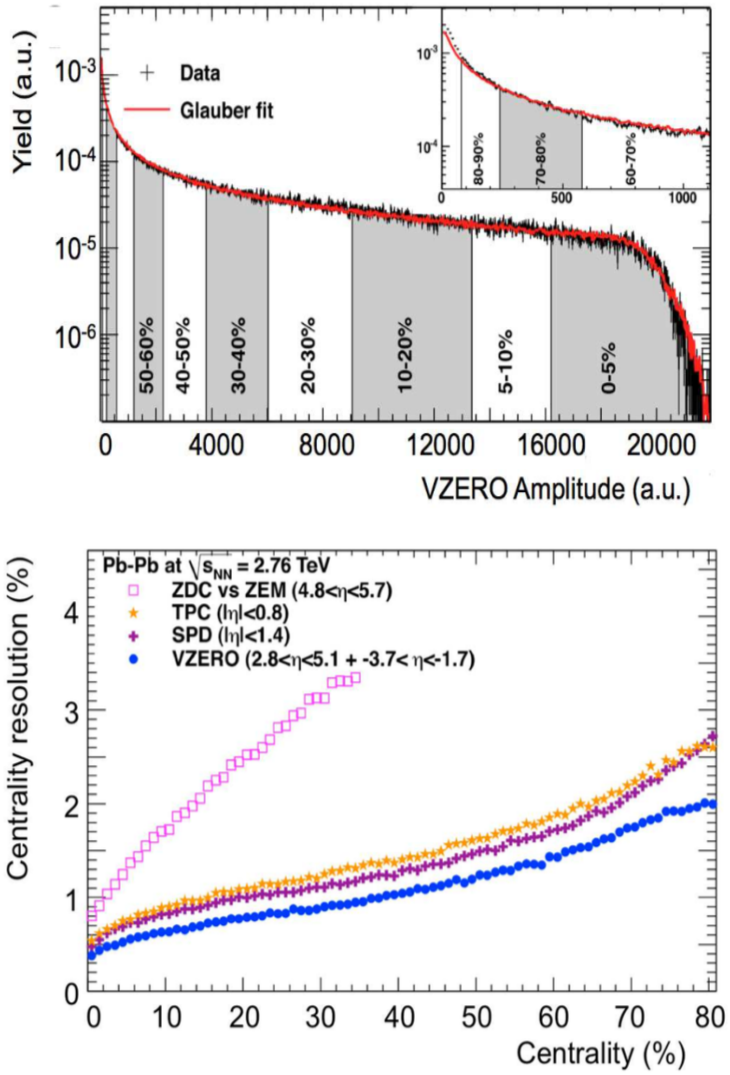

Figure 2.13: Centrality estimation using V0

2.4.4 Photon Multiplicity Detector (PMD)

PMD is a forward detector designed to measure the event-by-event multiplicity and the spatial distribution of photons in the forward region. The working principle is shown in Fig 2.15. It is a highly granular preshower detector with full ϕ acceptance and $1.8 \leq \eta \leq 2.6$ placed at a distance of 5.8 m from the IP on the opposite side of the dimuon spectrometer [12, 13]. Photons pass through a converter and initiate electromagnetic shower producing signals on several cells of the detector. Hadrons do not produce shower and usually hit only one cell and generate a MIP

signal (minimum-ionizing particle). The converter's thickness is chosen in such a way that the photon conversion probability is high. Also the transverse spread of shower is kept small so that the overlap of shower does not occur in high multiplicity events. The veto detector in front of the converter is used to reject charged particles. PMD is able to study event shapes and fluctuations

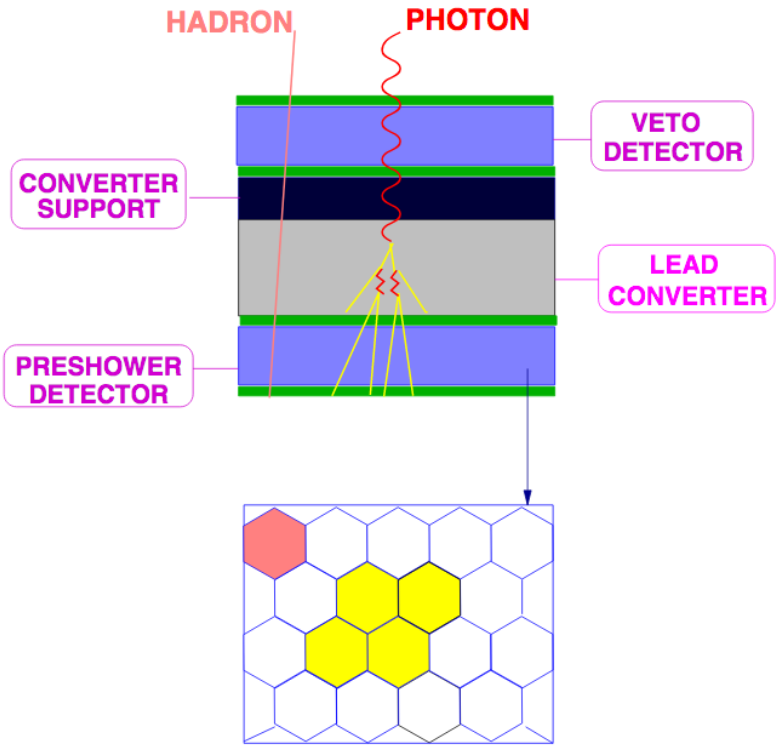

Figure 2.14: Working principle of PMD in ALICE

in the forward region. Using the preshower signal the PMD will provide estimates of transverse electromagnetic energy.

2.4.5 Zero Degree Calorimeter (ZDC)

ZDC measures the energy of the spectator nucleons and therefore, the centrality of the collision can be estimated using this detector. When two nuclei collide, they can overlap fully or partially. In peripheral collisions, a small portion of the nuclei overlap, therefore only a few nucleons participate in that collision and most of the nucleons fly apart along the beam direction without

participating. These are called spectator nucleons [14]. ZDC is the farthest detector from IP which collects these spectator nucleons. These spectators deposit their energy in ZDC. For central collision, the deposited energy is very small, whereas, for peripheral collisions, the energy deposited is large. Therefore, the centrality of a collision can be estimated by ZDC. It has a dense absorber where incident particles generate showers and quartz fibers where the showers produce Cherenkov radiation. It consists of two proton calorimeter (ZP) and two neutron calorimeter (ZN) to detect protons and neutrons respectively placed along beam line 115 meters away from the IP on both sides. Hence, they are called Zero Degree Calorimeters (ZDC). But due to the incomplete fragmentation of the spectator nucleons, the correlation between the ZP and the ZN is not sufficient for the determination of the centrality of collision. So, there is an electromagnetic calorimeter (ZEM) in ZDC to measure the energy of forward photons coming from neutral pion decays.

2.4.6 Muon Spectrometer:

Heavy quarkonium states like $J/\psi, \psi', \Upsilon, \Upsilon', \Upsilon$" help to study the hot and early stage of heavy ion collision as they are sensitive to QGP formation [15, 16]. In presence of QGP at high energy, quarkonium states are dissociated due to colour screening. Therefore, their production rate is suppressed. The ALICE forward muon spectrometer basically detects these quarkonia through their decay in $\mu^+\mu^-$ channels. This detector covers pseudorapidity range $2.5 \leq \eta \leq 4$ with full azimuthal acceptance and the resonances can be detected down to a very low p_T. The invariant mass resolution is about 70 MeV in the J/ψ region and about 100 MeV for Υ. The layout of the Muon spectrometer is shown in Fig 2.16. The inner beam shield protects the chambers from background particles. The front absorber, made of carbon and concrete, filters all the particles except muon coming from vertex. It limits the multiple scattering and energy loss of the muons. The tracking system is made of 10 cathode pad chambers which are made of composite material

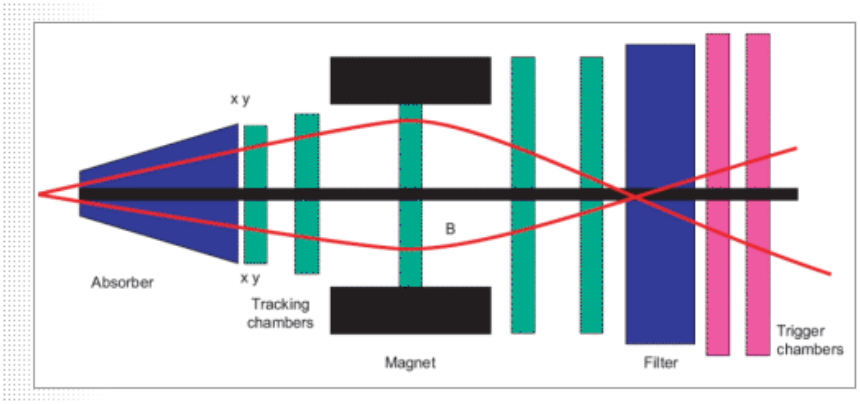

Figure 2.15: Muon spectrometer

to minimize the scattering of the muons and the trigger system is to select heavy quark resonance decays. It selects on the basis of the p_T of the two individual muons. Most of the muons that are emitted in the decays of the J/ψ or Υ family resonances have a p_T larger than the background muons from pion and kaon decays. Therefore, a cut on the p_T of the muons is implemented by the trigger to reject the background muons and to select the interesting events that contains at least one pair of opposite-sign muons with a high p_T. It consists of a large dipole magnet which helps in tracking and momentum reconstruction of muons.

2.4.7 Triggers:

The data from all the underground ALICE detectors are transmitted to the Data Acquisition farm near the surface over optical fibers using the Detector Data Links (DDLs). There are two types of computers there. The Local Data Concentrators (LDCs) or the first layer of computers receives and formats the data and send it to the Global Data Collectors (GDCs) or second group of computers after data is accepted by the High Level Trigger (HLT). GDCs put all the things together to create the so-called events which are stored on local disks (the Transient Data Storage - TDS) in files encoded using the AliROOT format, adopted for the Offline data processing. The data files are finally transferred to the CERN Computing Centre, and are ready to be published

on the Grid.

There are four online systems in the ALICE experiment to control, read out, and monitor different sub-detectors: trigger system, Detector Control System (DCS), High Level Trigger(HLT) and Data AcQuisition (DAQ). The Experiment Control System(ECS) organizes the operations controlled by these four systems.

The trigger system (hardware trigger) selects events of particular interest while rejecting the others. A sub-detector is called trigger detector when it participates in the production of a trigger decision, whereas, when it participates in the readout of data, it is called a readout detector. A sub-detector can be both triggering and readout detector in the same run. For example, EMCal and PHOS can act as both trigger and readout detectors. The trigger system receives triggers from many triggering detectors, makes decisions and selections, and then sends the final trigger decisions to readout detectors. ALICE provides three level trigger system - Level-0 (L0), Level-1 (L1) and Level-2 (L2) triggers. In some readout detectors, trigger decision L0 has to be supplied in 1.2 μs just after the collision occurs which is very fast for some triggering detectors. A L1 trigger is defined for those detectors which need longer time than L0 triggers. ACORDE, TOF, HMPID, PHOS, V0, T0, muon spectrometer produces L0 trigger. TRD produces L1 trigger for electrons of high momentum. EMCal provides L0 and L1 triggers.

2.4.8 ALICE Offline analysis:

After reconstruction, the events are called Event Summary Data (ESD) which contain all information about an event and its tracks like trigger type, vertex, centrality, multiplicity and track by track PID from various detectors. But, ESD files are of huge volume and not efficient to handle. Therefore, the data files are compressed to the Analysis Object Data (AOD) which are derived from ESD by filtering. Tracks which pass some sets of cuts are stored and rest are deleted from

AOD. Thus AOD contains only the physics related data and is efficient to handle, though analysis can be done using both AOD and ESD.

Bibliography

[1] LHC -The Guide, https://home.cern/resources/brochure/cern/lhc-guide

[2] The CERN Large Hadron Collider : Accelerator and Experiments, Volume 1, Breskin, Amos (ed.) and Voss, Rudiger (ed.) (CERN), 2009.

[3] The ALICE experiment at the CERN LHC, K. Aamodt et al., [ALICE Collaboration], J. Instrum. 3, S08002 (2008).

[4] ALICE Collaboration: "Performance of the ALICE Experiment at the CERN LHC" Int. J. Mod. Phys. A 29, 1430044 (2014).

[5] ALICE Inner Tracking System (ITS): Technical Design Report, CERN-LHCC-99-012

[6] B. Abelev *et al.* [ALICE], Technical Design Report for the Upgrade of the ALICE Inner Tracking System, J. Phys. G **41** (2014), 087002

[7] ALICE Time Projection Chamber: Technical Design Report, CERN- LHCC-2000-001, http://cdsweb.cern.ch/record/451098.

[8] ALICE Time-Of-Flight system (TOF): Technical Design Re- port, CERN- LHCC-2000-012, http://cdsweb.cern.ch/record/430132.

[9] ALICE Time-Of-Flight system (TOF): addendum to the technical design report, CERN-LHCC-2002-016, http://cdsweb.cern.ch/record/545834.

[10] L. Lijiao,L0/L1 trigger generation by the ALICE PHOS detector, CERN-THESIS-2011-356.

[11] ALICE forward detectors: FMD, T0 and V0: Technical Design Report, CERN-LHCC-2004-025, http://cdsweb.cern.ch/record/781854.

[12] ALICE Photon Multiplicity Detector (PMD): Technical Design Report, CERNLHCC-99-032, http://cdsweb.cern.ch/record/451099.

[13] ALICE Photon Multiplicity Detector (PMD): addendum to the technical design report, CERN-LHCC-2003-038, http://cdsweb.cern.ch/record/642177.

[14] ALICE Zero-Degree Calorimeter (ZDC): Technical Design Report, CERN- LHCC-99-005, http://cdsweb.cern.ch/record/381433.

[15] ALICE dimuon forward spectrometer: Technical Design Report, CERN- LHCC-99-022, http://cdsweb.cern.ch/record/401974.

[16] ALICE dimuon forward spectrometer: addendum to the Technical Design Re- port, CERN-LHCC- 2000-046, http://cdsweb.cern.ch/record/494265

Chapter 3

Study of medium modified jet shape observables in Pb-Pb collisions at $\sqrt{s_{NN}}$=2.76 TeV using EPOS and JEWEL event generators

3.1 Introduction

In high energy heavy ion collisions at the RHIC and the LHC energies, as per available data, a medium with partonic degrees of freedom is formed [1]. The transition from a confined hadronic phase to a deconfined partonic phase has been concluded to be a cross-over [2]. A wide range of observables measured in Au-Au/Pb-Pb collisions and their comparison with the reference systems like pp collisions shed light on various properties of the medium. One of the early observables in this field of study that probed the gluon-density of the medium had been the fragments of highly energetic partons in terms of high p_T leading particles and additionally reconstruction of full jets

at the RHIC and LHC energies [3, 4, 5, 6, 7, 8]. Initially, global jet-observables in the form of suppression of both the leading particles and jets, commonly known as jet-quenching have been used to probe the gluon-density of the medium. [9, 10, 11].

Now, energy loss of partons by radiation or collision is expected to modify the fragmentation function of the incoming partons. It is expected that during the process of energy loss and hadronization, the internal structure of jet also undergoes modification. Measurements of observables like transverse spread of energy and momentum of the jet fragments in central heavy ion collisions and it's comparison to pp collisions lead to a conclusion that the core of the jet gets harder and the periphery gets extended to a larger radii with softer fragments due to jet-medium interaction [12]. Observables like energy asymmetry (A_j) and variation of particle density inside a jet cone with radial distance have been used to understand the energy distribution within jets after quenching [13, 14].

As per the theoretical descriptions of jet quenching [9, 15, 16, 17, 18, 19], higher energetic partons suffer energy loss due to their interactions with the thermal partons in the medium and these scattered partons can have an effect on the final jet-shape parameters [20, 21, 22]. Analyzing the jet-shape parameters therefore will help to understand the underlying interaction of jets with the medium. Studies are ongoing using various models for estimating the effect of jet-quenching on jet-shape observables. These models mostly describe the global jet observables like R_{AA} quite well [23, 24, 25]. One model that has been extensively used in such studies is JEWEL [26] that describes the global jet properties quite satisfactorily at the LHC energy. The model as discussed in the next section in detail, does not simulate the heavy ion collisions as a whole. Rather it uses the perturbative QCD to describe the interaction of the hard scattered partons with an ensemble of partons whose phase space distribution and flavor composition are provided by the Bjorken model [27]. In JEWEL, interaction of the shower partons with the medium partons can be treated in two

modes i.e., recoil OFF and recoil ON. In the recoil OFF version, the recoiled medium partons do not take part in further processes towards hadronization. The recoil-ON version, on the other hand propagates the effect of those recoiled partons to the final observables. Analysis of results from the recoil-ON version however faces the challenges of background subtraction which is necessary for comparison with the experimental results [24]. Even though extensive efforts have been made to develop background subtraction methods, they have their own limitations. The recoil-OFF version can however be compared with the experimental results directly. Experimentally, for very high p_T jets($>$ 100 GeV/c), the background reduces drastically mainly due to higher kinematic cuts applied on the fragments for jet reconstruction [28]. But for jets with relatively lower p_T, background effect is more prominent along with the other softer contributions from the medium. This issue is similar for both data and the event-generators simulating the jet-medium interactions. At a jet p_T range of say 20-40 GeV/c, the absence of full event simulation in JEWEL coupled to the uncertainties in various background subtraction methods together make the predictions of jet-shape observables with recoil-ON version even more complicated. In this study, we have taken JEWEL with recoil-OFF and studied the jet p_T range of 20-40 GeV/c with R = 0.2 and 0.3 as a reference, where R is the resolution parameter or the radius parameter of the jet.

In addition to the results from JEWEL taken as a reference, we have studied the same set of jet-observables using another model named EPOS-3 [29, 30] that explains the bulk observables in high energy heavy ion collisions quite satisfactorily [31, 32, 33, 34]. However the model has not been tested well for hard probes. EPOS-3, a full event generator and described in the next section in detail considers the collision zone consisting of two regions called core and corona. The core is the region that undergoes 3+1 D event by event hydrodynamic evolution and explains observables like flow, particle production at low p_T quite well. The corona region, on the other hand consists of jets and implements the high p_T phenomena. The simplistic implementation of the partonic

energy loss in EPOS-3 is different from the conventional jet-energy loss models. In addition, a modified hadronization procedure through recombination of the string segments from the core and corona regions has been found to be essential in explaining the R_{AA} upto $p_T \approx 20$ GeV/c in heavy ion collisions. Hence, the comparison of the jet shapes obtained using EPOS-3 and JEWEL will shed some light on the different physics processes capable of explaining the jet-shape broadening in heavy ion collisions. In EPOS-3, the probability of formation of jet-hadrons inside the fluid freezeout surface is considerably high upto $p_T \approx 20$ GeV/c and these jet-hadrons also have a large probability of re-scattering with the soft hadrons from freeze-out. These secondary hard-soft interactions can modify the distribution of jet particles inside the jet cone. Hence, the comparison of the jet shapes obtained using EPOS-3 and JEWEL will shed some light on the different physics processes which can potentially explain the jet-shape broadening in heavy ion collisions.

In this work, we reconstruct jets from the two models with two R values of 0.2 and 0.3 with a jet p_T range of 20-40 GeV/c. This low-intermediate jet p_T range, where medium induced modifications to the jets are stronger, consists of jet constituents having $p_T < 20$ GeV/c and suitable for investigating the effect of secondary hard-soft interactions in EPOS-3 as described above. We have studied a set of jet-shape observables as described in section 3.3. Higher R values access higher transverse region and thereby explores the lost jet energy region in greater detail.

Main motivation of this work can be listed as (a) sensitivity of JEWEL on jet-shape at lower p_T region without considering the recoiled partons. The possible difference in the pattern compared to the experimental data may help to better understand the effect of these medium partons on the jet-shape observables, (b) Study the jet-shape observables in the same p_T range using EPOS-3 that includes a simplistic partonic energy loss mechanism and secondary hard-soft interactions during hadronization and the hadronic cascade phase.

This chapter is organised as follows, in the next section we provide further details on two models

i.e. JEWEL and EPOS-3 in the context of jet quenching, in section 3.3, we discuss the observables and the analysis method adopted here. Section 3.4 presents the results and the discussions.

3.2 Event generators: JEWEL and EPOS

EPOS-3 is a parton based model with flux tube initial conditions [35, 36, 37, 38]. Initially, the partons undergo multiple scatterings and the final state partonic system consists of mainly longitudinal color flux tubes (strings) carrying transverse momentum of the hard scattered partons in the transverse direction [31, 39]. Depending on the partonic energy loss scheme as described in [29] and local string density, these strings will eventually form the core (bulk) and the corona (jet). The low momentum strings in the high density area undergo hydrodynamic evolution and form the bulk. Whereas, the highly energetic strings in the low density area form the corona (jet) following Schwinger mechanism [34]. In EPOS-3, the partonic energy loss scheme doesn't involve the hydrodynamic fields and it depends on the initial geometric size of the fireball and density of the string segments along with some other parameters. The secondary hard soft interactions take place at the hadronization and also during the hadronic cascade phase [29]. For example, the intermediate p_T corona string segments have significant probability of forming inside the fluid freeze-out surface and these segments may pick up partons from the thermal matter rather than creating them via usual Schwinger mechanism [29, 34]. In addition, these string segments will also suffer hadronic interactions with the soft hadrons from the fluid freeze-out and may affect the properties of the jet. This approach has been found to be essential in describing several experimental features such as the nuclear modification factor (R_{AA}) [29, 32], baryon to meson enhancement at intermediate p_T [33], elliptic flow at higher p_T [29] etc in heavy ion collisions. In this work, the jet-shape will reflect the effect of the jet-fluid interactions in both partonic and hadronic phases as implemented in EPOS-3 and will be compared with the JEWEL (recoil OFF) results.

JEWEL is a Monte Carlo simulation program designed for the study of jet quenching in heavy ion collisions. It interfaces a perturbative final state parton shower with the medium and accounts dynamically for the interaction between jet and medium. Aforementioned, the background medium consists of an ensemble of partons whose phase space distribution and flavor composition are determined by an external medium model [27]. The current version of JEWEL uses a variant of the Bjorken model [27] which describes the boost-invariant longitudinal expansion of an ideal QGP. The shower initiated by the hard scattered parton interacts with the background partons and loses energy through elastic and radiative processes.

JEWEL can be used in two operational modes: recoil ON and OFF [27]. In the recoil OFF mode, the energy and momentum transferred to the background partons are not taken into account in the final state fragmentation. Whereas, in the recoil ON case [27, 40], the recoiling partons are inserted into the strings connecting the parton shower and this significantly improves the description of the jet shape observables in JEWEL after proper background subtraction [27].

3.3 Observables and analysis method

Even though a large number of jet-shape observables are being used to study the jet-medium interactions, in this work, we study two particular observables called differential jet-shape (ρ(r)) [13] and the angularity or girth g [41] . The differential jet shape ($\rho(r)$) [13] describes the radial distribution of the jet transverse momentum density inside the jet cone. The definition has been given in Eq. 1.6 with the description of the parameters. The Angularity or girth [41] that measures the radial energy profile of the jet is defined in Eq. 1.9.

These shape observables provide quantitative description of the radial distribution of the jet energy inside the jet cone and have been extensively measured by all the experimental collaborations at the LHC [13, 42, 41, 43]. In heavy ion collisions, based on these observables, the jet

core has been found to be more collimated and harder compared to the pp collisions at the same reconstructed jet energy, accompanied by a broadening of the jet at it's periphery [13, 14].

The analysis is performed on the charged jets reconstructed with the sequential $anti-k_T$ jet finding algorithm using the Fastjet package [45]. Jets are reconstructed with two different values of resolution parameters R = 0.2 and R = 0.3 for $20 < p_{T,chjet} < 40$ GeV/c. The minimum transverse momentum of the tracks allowed for jet reconstruction is set to 0.15 GeV/c. Tracks are selected within $|\eta| < 0.9$ and jets are selected with $|\eta_{jet}| < 0.7$ and $|\eta_{jet}| < 0.6$ for R = 0.2 and R = 0.3 respectively. The jets having at least one particle with transverse momentum above $p_T > 5$ GeV/c are considered to reduce the contribution of the combinatorial jets in the selected jet sample [46][47].

In this work, we have used pp collisions in JEWEL to represent no medium effect and have then compared with Pb-Pb results from both the models. It should be noted that even though we have compared pp and Pb-Pb collisions at the same reconstructed jet p_T range, it is likely that the intial jet partons in Pb-Pb were of higher energy before loosing energy in the medium.

For making the observables on the same footing as on the experimental data, we have used JEWEL recoil OFF data without background subtraction and in EPOS, only corona (jet) particles are considered to construct the jet.

3.4 Results and Discussions

The top panels of Fig. 3.1 and Fig. 3.2 show the comparison of differential jet shape measurements ($\rho(r)$) between 0-10% Pb-Pb collisions and minimum bias pp collisions at 2.76 TeV using the JEWEL (recoil OFF) and EPOS-3 event generators in the jet p_T range of 20-40 GeV/c for R = 0.2 and R = 0.3 respectively. Qualitatively, we find a set of similarities in results from both models except at high radial distance with resolution parameter R = 0.3. We can clearly see that for both

the models while going radially outward from the jet-axis, the relative difference in ρ(r) distribution between 0-10% Pb-Pb and minimum bias pp collisions changes. This indicates a modification in distribution of energy inside the jet cone.

To quantify the medium induced modifications, the jet shape nuclear modification factor $(\rho(r)^{PbPb}/\rho(r)^{pp})$ for both the models are shown at the bottom panels of two figures. Deviation of the ratio $(\rho(r)^{PbPb}/\rho(r)^{pp})$ from unity indicates a modification to the jet structure in presence of the medium. In comparison to the jet-shape in pp, a narrowing of the jet core (at r $<$ 0.02) with higher momentum density has been observed in central Pb-Pb collisions in cases of both EPOS-3 and JEWEL and this is qualitatively similar to the pattern observed in experimental measurements by different collaborations at the LHC [41, 13, 48]. One of such results has been shown in Figure 1.25.

As discussed earlier, due to in-medium energy loss, jets reconstructed with a fixed R in central Pb-Pb collisions may originate from higher energy initial parton compared to that in pp. As the jet core gets harder with increase in jet energy/momentum and is less affected in presence of a medium, the jet core in central heavy ion collisions can be harder compared to the peripheral and minimum bias pp collisions as shown in Fig.3.1 and Fig.3.2. Interestingly, the ratio $(\rho(r)^{PbPb}/\rho(r)^{pp})$ becomes less than unity at intermediate radii indicating the in-medium energy loss in central PbPb collisions.

To understand the redistribution of the lost energy in the medium, we compare the results for two values of the resolution parameter i.e. R = 0.2 and R = 0.3 respectively. Increasing the resolution parameter from R = 0.2 to to R = 0.3 open up the possibility of including the energy carried away by softer particles at larger angles from the jet axis. For both the models and the resolution parameters, the ratios $(\rho(r)^{PbPb}/\rho(r)^{pp})$ remain below unity upto a radial distance of 0.2. However at higher radial distances, while it remains below unity for JEWEL (recoil OFF) but goes above unity for EPOS-3 indicating a moderate broadening of jets at the periphery in EPOS-3.

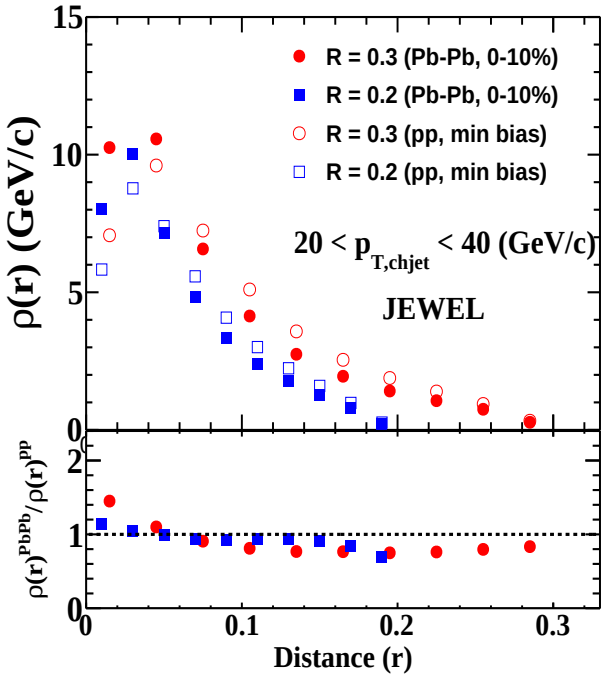

Figure 3.1: **Upper panel:** Differential jet shape $\rho(r)$ measured as a function of distance from the jet axis for inclusive charged jets in $20 < p_{T,chjet} < 40$ GeV/c with $R = 0.2$ and $R = 0.3$ in 0-10% central Pb-Pb collisions at $\sqrt{s_{NN}} = 2.76$ TeV using the JEWEL (recoil OFF) event generator and compared with the minimum bias pp results. **Lower panel:** The jet shape nuclear modification factor, quantified as $\rho(r)^{PbPb}/\rho(r)^{pp}$

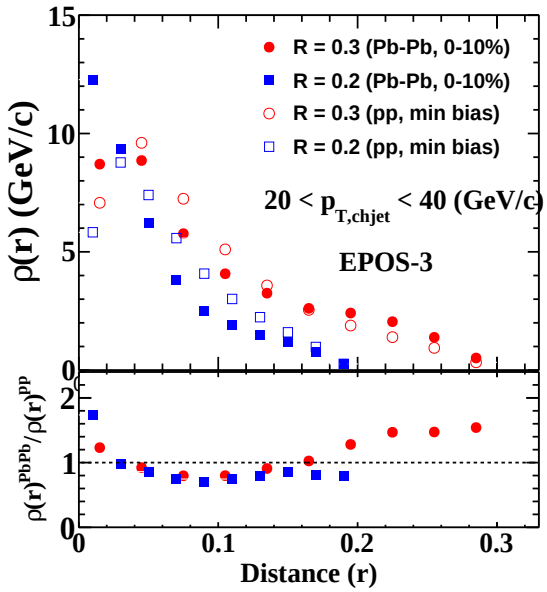

Figure 3.2: **Upper panel:** Differential jet shape $\rho(r)$ measured as a function of distance from the jet axis for inclusive charged jets in $20 < p_{T,chjet} < 40$ GeV/c with $R = 0.2$ and $R = 0.3$ in 0-10% central Pb-Pb collisions at $\sqrt{s_{NN}} = 2.76$ TeV using the EPOS-3 event generator and compared with the minimum bias pp results. **Lower panel:** The jet shape nuclear modification factor, quantified as $\rho(r)^{PbPb}/\rho(r)^{pp}$

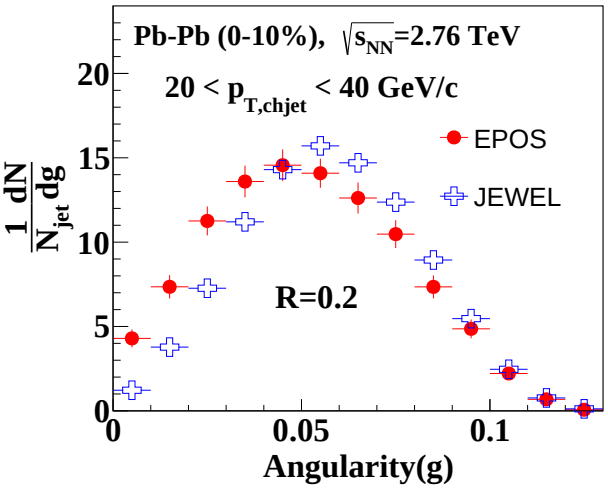

Figure 3.3: Angularity (g) measured in 0-10% central Pb-Pb collisions for inclusive charged jets in $20 < p_{T,chjet} < 40$ GeV/c with $R = 0.2$ using the EPOS-3 and JEWEL (recoil OFF) event generators.

The broadening of jets at the periphery in EPOS-3 is qualitatively consistent with the experimental observations which indicate that the energy lost due to jet-medium interaction is distributed at larger distances from the jet axis and represents a clear signature of in-medium modification of internal jet structure [13]. Aforementioned, in EPOS-3, the simple partonic energy loss mechanism doesn't involve the interaction of jets with hydrodynamically evolving medium. Rather, it depends on the initial geometry of the fireball and local string density along with modified hadronization where the intermediate-p_T jet-string segments pick up hydrodynamically flowing string segments and further interact with the bulk hadrons from the freeze-out. These hard-soft interactions in EPOS-3 contribute to the redistribution of the jet energy inside the jet cone and qualitatively describe the jet-shape broadening in heavy ion collisions.

It should however be noted that in case of JEWEL as well, there is a slight trend of increasing the ratio towards unity at larger radii. Also, it has been observed [44, 49] that at higher jet-p_T, the ratio goes above unity at higher radii for JEWEL with recoil ON suggesting that the recoiled partons carry and redistribute the energy lost by jets to larger radii.

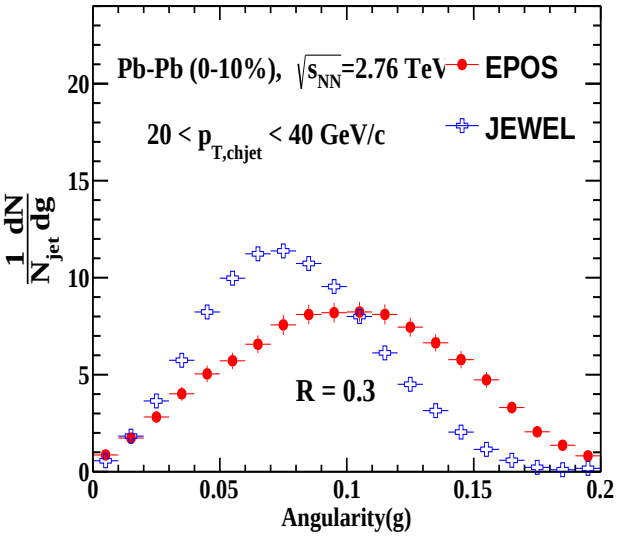

Figure 3.4: Same as Fig.3.3 but for jets with $R = 0.3$ and in the transverse momentum range $20 < p_{T,chjet} < 40$ GeV/c.

To further investigate the radial energy profile of the jets, we also measure the angularity for the two event generators and compared them in Fig. 3.3 and Fig. 3.4 for R = 0.2 and R = 0.3 respectively. For smaller resolution parameter (R = 0.2), the jet core plays an important role in the measurement of jet shapes and Fig. 3.3 indicates that the jet core in EPOS-3 is more collimated than JEWEL. This is qualitatively similar to what we observe in the differential jet shape ($\rho(r)$) measurements as shown in Fig. 3.1 and Fig. 3.2. For larger radius (R = 0.3), a fraction of energy lost by the jets inside the medium is included inside the jet cone and that broadens the jet at the periphery for both models as shown in Fig. 3.4. The jet in EPOS-3 is harder at core and broader at periphery compared to JEWEL and is consistent with the differential jet shape measurements shown earlier.

Our work shows that EPOS-3 which takes into account a simplistic partonic energy loss mechanism and recombination of core and corona string segments at intermediate p_T can qualitatively explain the in-medium modification to the jet shapes in heavy ion collisions. As discussed earlier,

the JEWEL with "recoil ON" can reasonably explain the jet shapes in heavy ion collisions at higher p_T (where it is easier to make assumptions for background subtractions) thereby emphasizing the role of fragments of the scattered partons [27]. One of the main differences between the two event generators (EPOS-3 and JEWEL) lies in the way the event is simulated. JEWEL generates jets and models a medium around it as a collection of scattering centers whose cross sections and distributions in phase space can be chosen from an external medium model. The simplified modeling of the medium in JEWEL (recoil ON and OFF) can't explain the experimentally observed collective behaviors at low p_T as well as the nuclear modification factor (R_{AA}) for hadrons upto p_T = 20 GeV/C in heavy ion collisions [26]. In contrast, simulations based on EPOS 3 with a simple partonic energy loss mechanism and secondary jet-fluid interactions due to recombination of jet string segments with hydrodinamically flowing bulk string segments as well as hard-soft interactions in the hadronic phase can describe the nuclear modification factor [29] and in-medium modification to the jet-substructure in heavy-ion collisions in a consistent way. This observation indicates that the unconventional hard-soft interaction processes as implemented in EPOS-3 can be instrumental in the realistic modeling of jet-medium interactions. Further data-model comparisons over a broad range of jet-p_T with identified constituents will be essential for a better understanding of the medium and the underlying dynamics of the jet-medium interactions in heavy ion collisions.

Bibliography

[1] S. A. Voloshin, A. M. Poskanzer, R. Snellings; arXiv:0809.2949 [nucl-ex].

[2] L. Susskind, Phys. Rev. D **20**, 2610-2618 (1979) doi:10.1103/PhysRevD.20.2610.

[3] M. Connors, C. Nattrass, R. Reed, S. Salur; Rev. Mod. Phys. 90, 025005 (2018), arXiv:1705.01974 [nucl-ex].

[4] I. Arsene et al. (BRAHMS Collaboration), Nucl. Phys. A 757,1(2005).

[5] B. B. Back et al. (PHOBOS Collaboration), Nucl. Phys. A 757, 28(2005).

[6] K. Adcox et al. (PHENIX Collaboration), Nucl. Phys. A 757, 184(2005).

[7] J. Adams et al. (STAR Collaboration), Nucl. Phys. A 757, 102(2005).

[8] K. Aamodt et al.(ALICE Collaboration), Phys. Rev. Lett.105,(2010)252302, K. Aamodt et al.(ALICE Collaboration), Phys. Rev. Lett.107, (2011)032301.

[9] J.D. Bjorken, Fermilab Report No, PUB-82/59-THY, 1982,

[10] M. Gyulassy, M. Plumer, Phys. Lett. B 243 (1990) 432.

[11] G.Y Qin, X.N Wang, Int.J.Mod.Phys. E24 (2015) 1530014.

[12] ATLAS collaboration, Measurement of inclusive jet charged particle fragmentation functions in Pb+Pb collisions at sqrt(s(nn)) = 2.76 TeV with the ATLAS detector, reportNumber = ATLAS-CONF-2012-115" (2012).

[13] CMS Collaboration, Phys. Lett. B 730 (2014) 243 - 263.

[14] CMS Collaboration, JHEP 1611 (2016) 055.

[15] K. Aamodt *et al.* [ALICE Collaboration], Phys. Lett. B **696**, 30 (2011).

[16] S. Chatrchyan *et al.* [CMS Collaboration], Phys. Rev. C **84**, 024906 (2011).

[17] B. Betz, Eur. Phys. J. A **48**, 164 (2012).

[18] M. Gyulassy and L. McLerran, Nucl. Phys. A 750, 3063 (2005).

[19] J.W Harris and B. Muller, Ann. Rev. Nucl. Part. Sci. 46, 71-107 (1996).

[20] C.A. Salgado, U.A. Wiedemann, Phys.Rev.Lett. 93 (2004) 042301.

[21] I. Vitev, S. Wicks, B.W. Zhang, J. High Energy Phys. 0811 (2008) 093.

[22] T. Renk, Phys. Rev. C 80 (2009) 044904.

[23] CMS Collaboration, Phys. Rev. C 84 (2011) 024906.

[24] ATLAS Collaboration, Phys. Rev. Lett. 105 (2010) 252303.

[25] D. Krofcheck [CMS Collaboration], PoS ICHEP **2012**, 418 (2013).

[26] K. C. Zapp, JEWEL 2.0.0: directions for use, Eur. Phys. J. C74 (2) (2014) 2762.

[27] Kunnawalkam Elayavalli, R. and Zapp, K.C. J. High Energ. Phys. (2017) 2017: 141. https://doi.org/10.1007/JHEP07(2017)141

[28] Megan Connors, Christine Nattrass, Rosi Reed, and Sevil Salur, arXiv-1705.01974 nucl-ex,10.1103/RevModPhys.90.025005, Rev. Mod. Phys. 90, 025005 (2018).

[29] K. Werner, Iu. Karpenko, M. Bleicher, T. Pierog, S. Porteboeuf-Houssais Phys. Rev. C 85, 064907 (2012).

[30] S. Porteboeuf, T. Pierog and K. Werner, arXiv:1006.2967 [hep-ph].

[31] K. Werner et al., Phys. Rev. C82 (2010) 044904.

[32] ALICE Collaboration, arXiv:1805.04361 [nucl-ex]

[33] K. Werner, Phys. Rev. Lett. 109, 102301 (2012).

[34] D. Sarkar, S. Chattopadhyay, Phys. Rev. C 95, 044906 (2017).

[35] K. Werner, B. Guiot, I. Karpenko and T. Pierog, Phys. Rev. C **89**, no. 6, 064903 (2014).

[36] K. Werner, I. Karpenko and T. Pierog, Phys. Rev. Lett. **106**, 122004 (2011).

[37] K. Werner, M. Bleicher, B. Guiot, I. Karpenko and T. Pierog, Phys. Rev. Lett. **112**, no. 23, 232301 (2014).

[38] H. J. Drescher, M. Hladik, S. Ostapchenko, T. Pierog and K. Werner, Phys. Rept. **350**, 93 (2001) doi:10.1016/S0370-1573(00)00122-8 [hep-ph/0007198].

[39] K. Werner, Phys. Rev. Lett. 98 (2007) 152301.

[40] R. Kunnawalkam Elayavalli and K. C. Zapp, Nucl. Part. Phys. Proc. **289-290**, 368 (2017) doi:10.1016/j.nuclphysbps.2017.05.085 [arXiv:1612.05116 [nucl-th]].

[41] L. Cunqueiro [ALICE Collaboration], Nucl. Phys. A **956**, 593 (2016).

[42] ALICE Collaboration, Nucl. Phys. A 956, 593 (2016).

[43] G. Aad *et al.* [ATLAS Collaboration], Phys. Rev. D **83**, 052003 (2011) doi:10.1103/PhysRevD.83.052003 [arXiv:1101.0070 [hep-ex]].

[44] B. Abelev et al. [ALICE Collaboration], Phys. Rev. D 91 112012 (2015).

[45] M. Cacciari, G. P. Salam and G. Soyez, Eur. Phys. J. C **72**, 1896 (2012).

[46] F. Krizek [ALICE Collaboration], J. Phys. Conf. Ser. **668**, no. 1, 012018 (2016).

[47] C. Nattrass [ALICE Collaboration], Acta Phys. Polon. B **47**, 1543 (2016).

[48] V. Khachatryan *et al.* [CMS Collaboration], JHEP **1611**, 055 (2016), arXiv:1609.02466 [nucl-ex].

[49] R. Biswas, Subikash Choudhury, S. K. Prasad and S. Das, J. Phys. G Nucl. = Part. Phys. 46 095004 (2019).

Chapter 4

Jets in pp collisions at $\sqrt{s} = 5.02$ TeV: Analysis details and results from the ALICE experiment

4.1 Analysis details

Measurement of jet shapes in pp collisions provides the baseline for the heavy-ion studies like the modification of the jet structures and that of the production rates in heavy-ion collisions due to the presence of the medium. For a comparison of experimental results with model calculations, it is needed to separate the contributions from the parton fragments by the hard scattering from that of the underlying event (UE) particles. The underlying event properties have been extensively studied in ALICE in pp collisions at $\sqrt{s} = 13$ TeV in [1]. It is found that the UE contributions increse by almost 30% from $\sqrt{s} = 7$ TeV to 13 TeV. This is specially important in case of high multiplicity pp collisions at $\sqrt{s}$ =7 TeV to 13 TeV but the UE contribution can be assumed to be insignificant at lower collision energies [2]. So, for pp collisions at $\sqrt{s}$ =5.02 TeV the contributions

from the UE particles are considered to be insignificant and no effect has been made to subtract them from the data. This is even more valid for min-bias pp collisions as have been studied in this analysis. However for higher jet radius, like R>0.7, UE contribution may be significant as more particles are included in the jet cone but for smaller radii (like R=0.2,0.4), the effects are considered to be insignificant. In the analysis presented in this thesis, the substructures of charged jets have been studied in p+p collisions at $\sqrt{s_{NN}} = 5.02$ TeV with a minimum bias trigger using TPC. Three jet shape observables have been used i.e, angularity, dispersion and LeSub. The charged particles of jets are measured using the Time Projection Chamber (TPC) and the Inner Tracking System (ITS), whereas, the electromagnetic component of the jet energy is measured by the ALICE EMCal. In this analysis, only the jets with charged particle components have been studied.

4.1.1 Jet finding

In the analysis the FastJet package has been used for jet finding [4, 5, 6, 7, 8]. Jets have been reconstructed with the $Anti - K_T$ algorithim for resolution parameter R=0.2,0.4 & 0.7 and E-scheme [8]. In this scheme, reconstructing the jet from particle level adds their 4-vectors. A minimum track p_T of 0.15 GeV/c is used as constituent cut and the jet acceptance is considered as $|\eta| < 0.7$ for R=0.2.

4.1.2 Definition of the jet shapes

Three jet shape parameters i.e. Angularity (g), Dispersion ($p_T D$), LeSub are used in this analysis. The definitions of these jet shape observables are defined in Eq. 1.7, 1.8 and 1.9. The first radial moment called angularity can be used to study whether the jets are collimated or broadened [9, 10, 3]. The momentum dispersion $p_T D$ tells how hard or soft the fragmentation is and the LeSub,

defined as the difference between the transverse momentum of the leading and the subleading particles of the jet, describes the hardest splitting. This shape variable is background invariant, so this is very important for analysis of the Pb-Pb collisions.

4.1.3 Jet reconstruction algorithm in data

In experiment, we get only final state stable particles. An algorithm groups the final state particles into jet candidates. In case of a conical jet, the resolution parameter which characterizes a jet finding algorithm is the radius of the jets and it is defined by, $R = \sqrt{\Delta\phi^2 + \Delta\eta^2}$, where $\Delta\phi$ and $\Delta\eta$ are the distances of a particle from the jet axis in ϕ and η. The most commonly used jet algorithm is the anti-k_T algorithm that reconstructs conical jets. But the jet measurement is not a direct measurement of a parton as it is not clear which final state particles should be considered as the parts of the jet. The jet-finding algorithms are encoded in the FastJet package which includes advanced computing algorithms to reduce the computational times for jet-finding which is essential in heavy ion collisions due to large background. In the anti-k_T algorithm [9], two quantities d_{ij} and d_i are calculated where,

$$d_{ij} = min(1/p_{T,i}^2, 1/p_{T,j}^2)\frac{(\eta_i - \eta_j)^2 + (\phi_i - \phi_j)^2}{R^2} \tag{4.1}$$

and $d_i = \frac{1}{p_{T,i}^2}$ for every pair of particles. Then the minimum between d_{ij} and d_i are found. If d_{ij} is the minimum , these particles are combined to one jet candidate by adding their energies and momenta. Then it returns to the first step. If d_i is minimum, then this is a final state jet candidate and is then removed from the list and the algorithm returns to the first step. This continues until there is no remaining particle. As d_{ij} is smallest for pairs of high-p_T particles, so this algorithm starts to cluster high-p_T particles into jets first and produces a jet around these particles. In heavy ion collisions, the jets from such a jet-finding algorithm may not be generated by hard processes.

Because all the final state particles are grouped into jet candidates, some jet candidates will have particles which are not created in the same hard process, rather they randomly come to that same region. These are called fake jets or combinatorial jets and these need to be subtracted [9]. The background subtraction is important for jets in heavy ion collisions but not important in pp collision as medium effect is assumed to be less significant.

Though it is almost impossible to know which particles in the jet belong to the hard process and which ones belong to the background, however the fact that the average momentum of the background particles is much less than that of the signal particles, can be used to reduce the effects of the background. At high p_T, particle production is mostly dominated by the hard processes. But jets themselves can be background for the measurement of other jets, though, the probability is low. So, the number of background particles as well as the number of combinatorial jets decreases after imposing a cut on the momentum of the particles to be used in jet-finding. Alternatively, background can be reduced by considering the higher energy jets or narrower jets by finding its area $A_{jet} = \pi R^2$. As the background energy is proportional to the area, however, independent of jet energy, therefore for higher energy jets, the change in the reconstructed jet energy due to the background is smaller. But the study of such high momentum jets cannot provide a complete picture of partonic energy loss mechanism in the QGP as the jets lose energy in the medium thereby becoming broader.

The contributions from the combinatorial jet candidates can be reduced by requiring at least one particle of the jet candidate above a minimum threshold or requiring a hard core in the jet candidate, or selecting a heavy flavor component within the jet candidate. Though it is ambiguous to distinguish the background particles arising from hard process from the fake jets, particularly for low momentum jets, but different methods are applied to correct for these effects separately.

4.1.4 Data sets:pp

The dataset used in this analysis is LHC 17p. A total 1.03 $\times$ 10^9 minimum bias pp events have been analyzed in this work and after event selection 9.09 $\times$ 10^8 events have been selected. The integrated luminosity is 18 nb^{-1} and EMCAL, MUON triggers are used.

4.1.5 Simulations:pp

We used a Pythia-8 simulation in 20 bins of p_T^{hard} to obtain the detector response in pp collisions. A total of 1.72 $\times$ 10^8 such events have been analyzed in this work.

4.1.6 Track and event selection

In this work, jets are reconstructed with final charged tracks as found in the detector. Global tracks with hits from SPD and refit with hits from ITS and the complementary tracks are used in jet reconstruction. Complementary tracks mean global tracks without SPD hit and with ITS refit. Tracks are selected with particle $|\eta|$ <0.9 and p_T >0.15 GeV/c.

The following cuts are applied which are implemented in the AliAnalysisTaskEmcalJet class for selection of events:

i) The number of vertex contributors is required to be > 1 to have a successfully reconstructed vertex

ii) Vertex position in z direction relative to the interaction point should satisfy -10 cm $< V_Z <$ 10 cm.

iii) The distance between the SPD vertex and the track vertex is required to be within : $\Delta V_z < 0.5$ cm. In this analysis we have used minimum bias pp collisons. These collisions have been tagged in ALICE as kINT7 where trigger select events from the real collisions and reject the ones coming from beam-gas interactions. This trigger requires at least one charged particle hit in both the V0A

and V0C detectors. A physics selection class has been also used to reject background and pileup events.

4.2 Raw distributions of jet shape variables in pp collisions

Distributions of the three raw jet shape variables for jet p_T range 40-60 GeV/c have been shown in Fig.4.1. At higher p_T, jets are found to be collimated for $R = 0.2$ as seen(in g and $p_T D$). If we increase the jet radius, jets are broadened for a particular jet p_T which can be seen in Fig. 4.1.

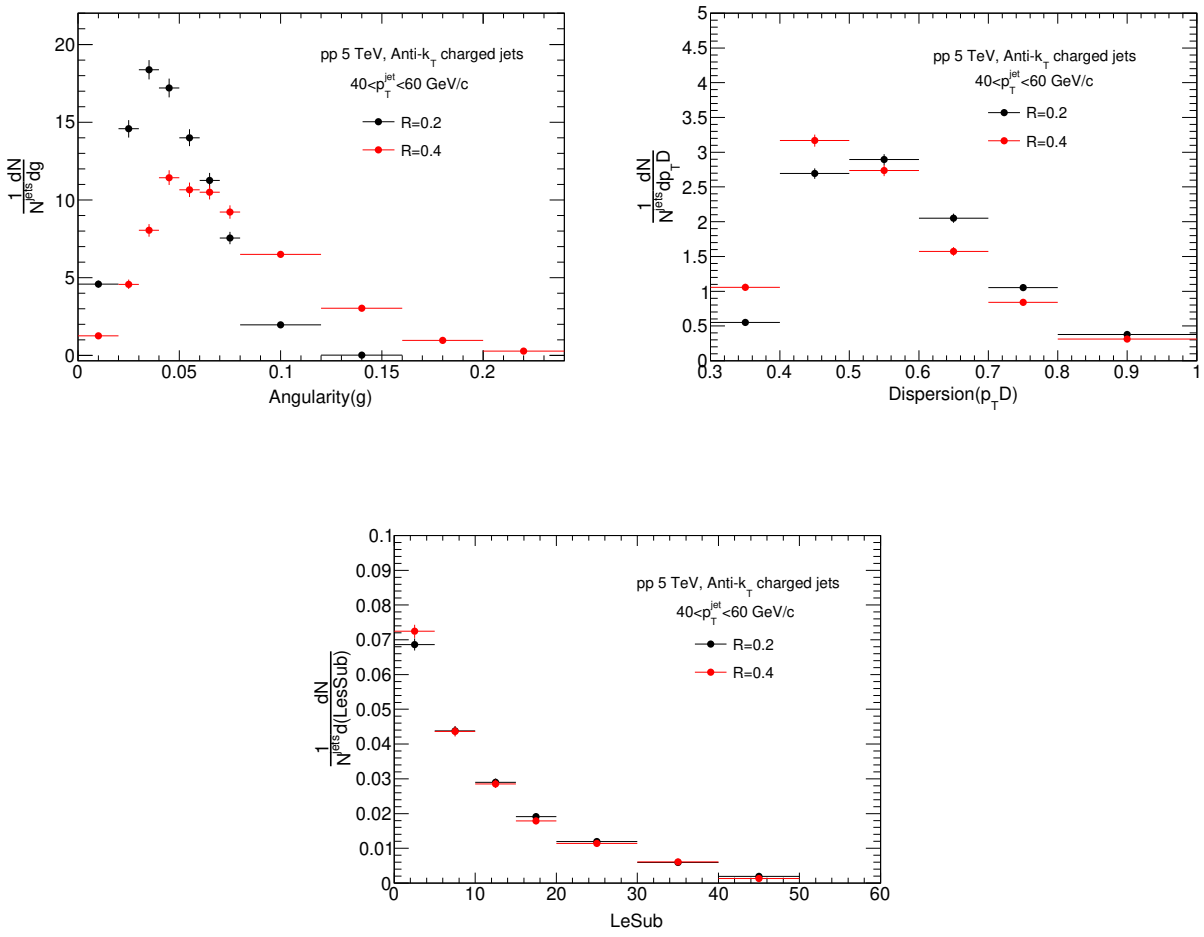

Figure 4.1: Raw shape distributions in pp collisions at $\sqrt{s}$ =5 TeV for R=0.2 and 0.4 with jet p_T = 40 GeV/c - 60 GeV/c. (top-left)angularity (top-right)Dispersion and (bottom)LeSub. Both g & p_TD show broadening with R=0.4 as compared to R=0.2

4.3 Unfolding in 2D

The measured jet shapes are usually distorted due to the detector effects and finite detector resolution. Therefore, to compare the obtained results to theoretical calculations or other measurements, the raw values should be corrected from the effects.

The true unknown shapes are extracted from the measured ones by a process called unfolding. The process acts on a binned distribution of the obtained values. If the true value of an observable in a bin ″i″ is given y_i^{true}, then the observed value in bin "j" is given by, $y_j^{reco} = \sum_i R_{ij} y_i^{true}$. where R_{ij} is the response matrix relating the true and obseved values [9]. The true value (y^{true}) is generated by an event generator such as PYTHIA. The jet finding algorithm is then applied on the particles at the event-generator level to generate the true jet observable in the particle level (y_i^{true}). After that, the true event is run through a detector simulation, track reconstruction, and track selection process to create the reconstructed event which can be considered as the "observed" event in data. Then the jet finding algorithm is applied on this reconstructed event to create the jets y_i^{reco} in which detector effects are follow in. After that , the observables in the particle level are matched to those in the detector-level jets to form the Response matrix. However, y_i^{true} cannot be estimated just by inverting as the Response matrices for jet observables may not always be regular. To solve the problem, a two dimensional Bayesian unfolding [11] technique based on the Bayes' theorem has been used which has been implemented in the RooUnfold package [12]. The probability of finding the true value in i^{th} bin when the measured value is in the j^{th} bin is estimated by Bayes' theorem using the relation $P = \frac{p_i R_{ij}}{\sum_k p_k R_{kj}}$. Here p_i is the initial guess of the true distribution or the base spectrum for unfolding and known as prior [13]. The raw distribution of the jet shape is the main input for unfolding which must not have any combinatorial background. The measured distribution is then multiplied with this probability to get an updated p_i. In the next iteration, this unfolded p_i is used as the prior. This method is repeated till the convergence of the soultion.

In the analysis the solution converges after 4 iteration. For the present analysis, jet shape variables are studied as a function of p_T^{jet}, therefore the observables are two-dimensional and the response matrix is a 4D matrix. This condition is satisfied when the lower p_T bin is more than $5 \times \delta p_T$. In this analysis δp_T is 4 GeV/c for $R = 0.2$, so we truncate measured spectra upto 30-40 GeV/c.

4.4 Statistical requirements for stable unfolding

For the statistical stability of the unfolding procedure the number of jets both for raw & true should be as high as possible. In the present case we have rebinned the distributions in such a way that at least 10 jets are present in every bin. We have given as example of the binning for R=0.2 as preferred for different shape observables.

1. g: 0,0.02,0.03,0.04,0.05,0.06,0.07,0.08,0.12 (for both raw & true)
2. $p_T D$: 0.3,0.4,0.5,0.6,0.7,0.8,1 (for both raw & true)
3. LeSub: 0,5,10,15,20,30,40 (for raw)
4. LeSub: 0,5,10,15,20,30,40 (for true)
5. p_T^{jet}: 20,25,30,35,40,45,50,55,60,80 (for raw)
6. p_T^{jet}: 0,20,40,60,80,100,120,140,160 (for true)

4.5 Graphical representations of the statistical limitations

The number of jets in each (shape,P_T^{jet}) bin for R=0.2 are shown in Fig 4.2 & 4.3. As shown in the following figures, the binnings satisfy the statistical requirement for the stability of unfolding.

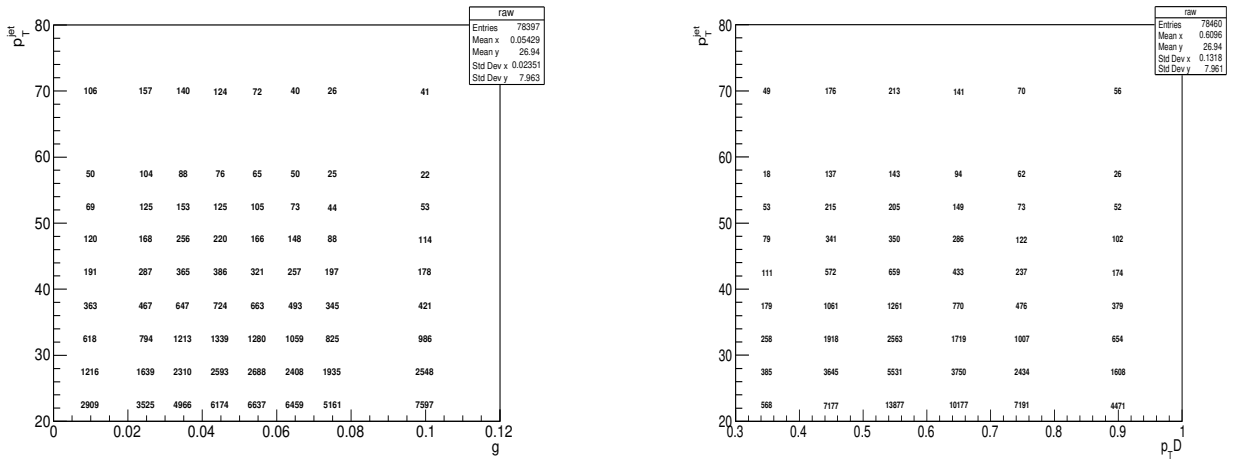

Figure 4.2: Left: 2D plot for p_T^{jet} vs Angularity in pp Right: 2D plot for p_T^{jet} vs Dispersion in pp

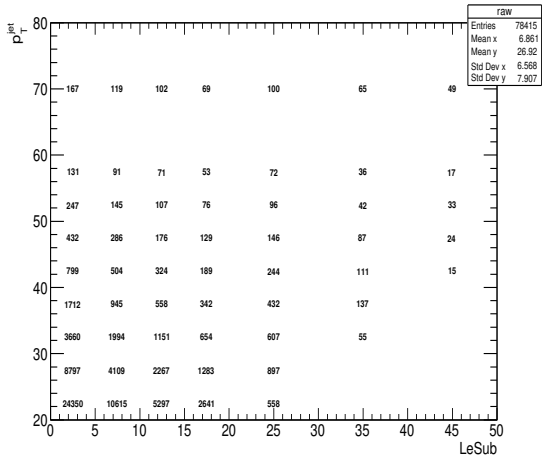

Figure 4.3: 2D plot for p_T^{jet} vs LeSub in pp

4.6 Responses

A response matrix connects the true observable with the measured observable. This contains the detector effects and background fluctuation effects. For an ideal detector and no background, the matrix should be 1-matrix with off-diagonal elements zero. In this analysis, jet shapes are studied which are 2D observables. Therefore, to unfold the shape variables a 4D response matrix [3] with axes $shape^{part}$,$p_{T,jet}^{part}$,$shape^{reco}$,$p_{T,jet}^{reco}$ has been constructed, where superscript 'part' refers to the generated or particle level and 'reco' refers to the reconstructed level or detector level. The

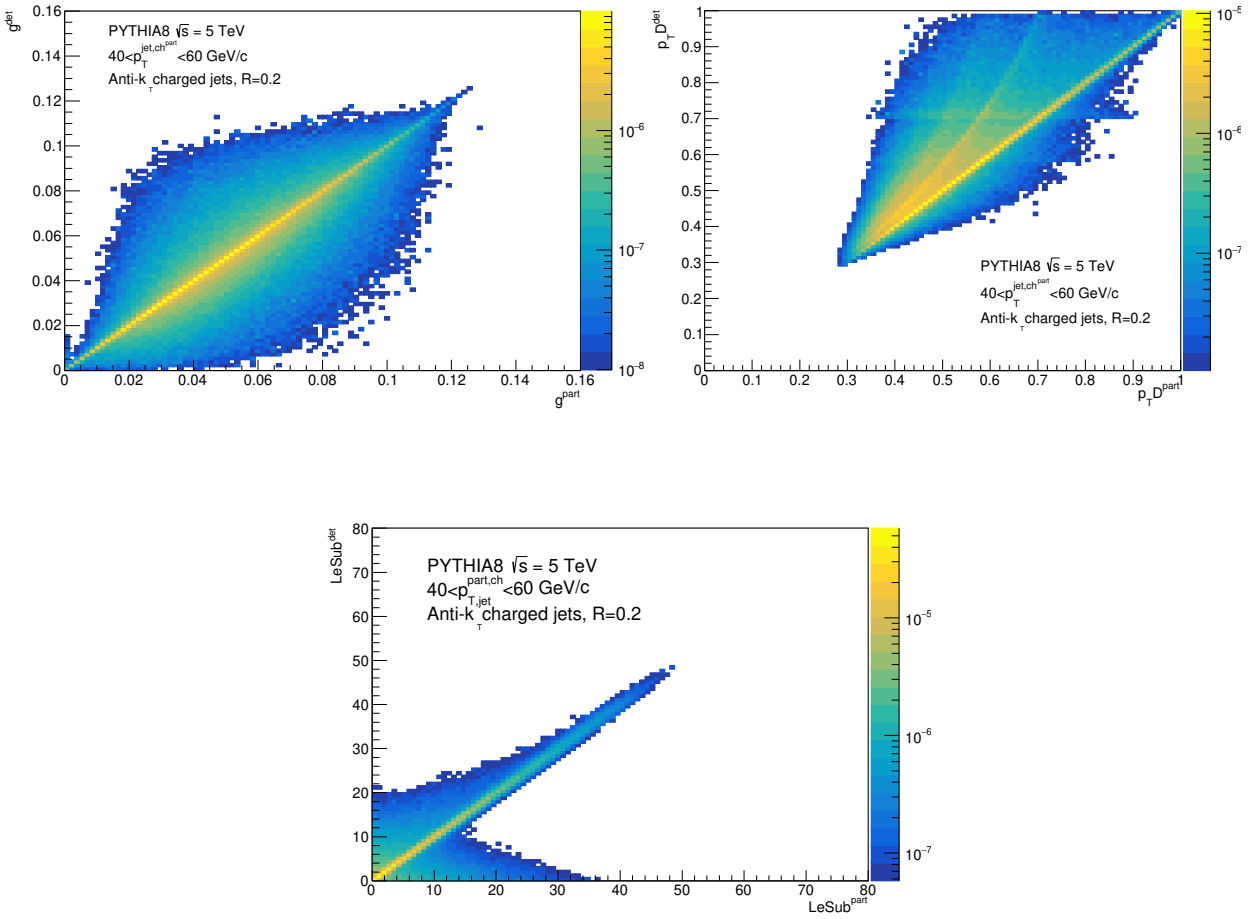

Figure 4.4: $shape^{reconstructed}$ vs $shape^{part}$ in pp for R=0.2 for jets 40 $GeV/c < p_T^{jet,part} < 60$ GeV/c

response matrix has been constructed using PYTHIA events at particle level and after full detector simulation and reconstructions. To evaluate the response matrix, the standard geometric matching

criteria between the particle level and the detector level MC jet must be satisfied which is known as the closest pair of jets. The correlation between the shapes at the particle and detector levels is shown in Fig. 4.4 for each jet shape observable, where the Z coordinate indicates probability. The jet shape resolution can be obtained as the RMS of the distribution of residuals between the reconstructed and the particle level shapes as shown in Fig. 4.5(for g & p_TD) and Fig 4.6(for LeSub). The resolution in angularity is defined as, $\sigma(\frac{g^{rec}-g^{part}}{g^{part}})$. In case of p_TD, the resolution

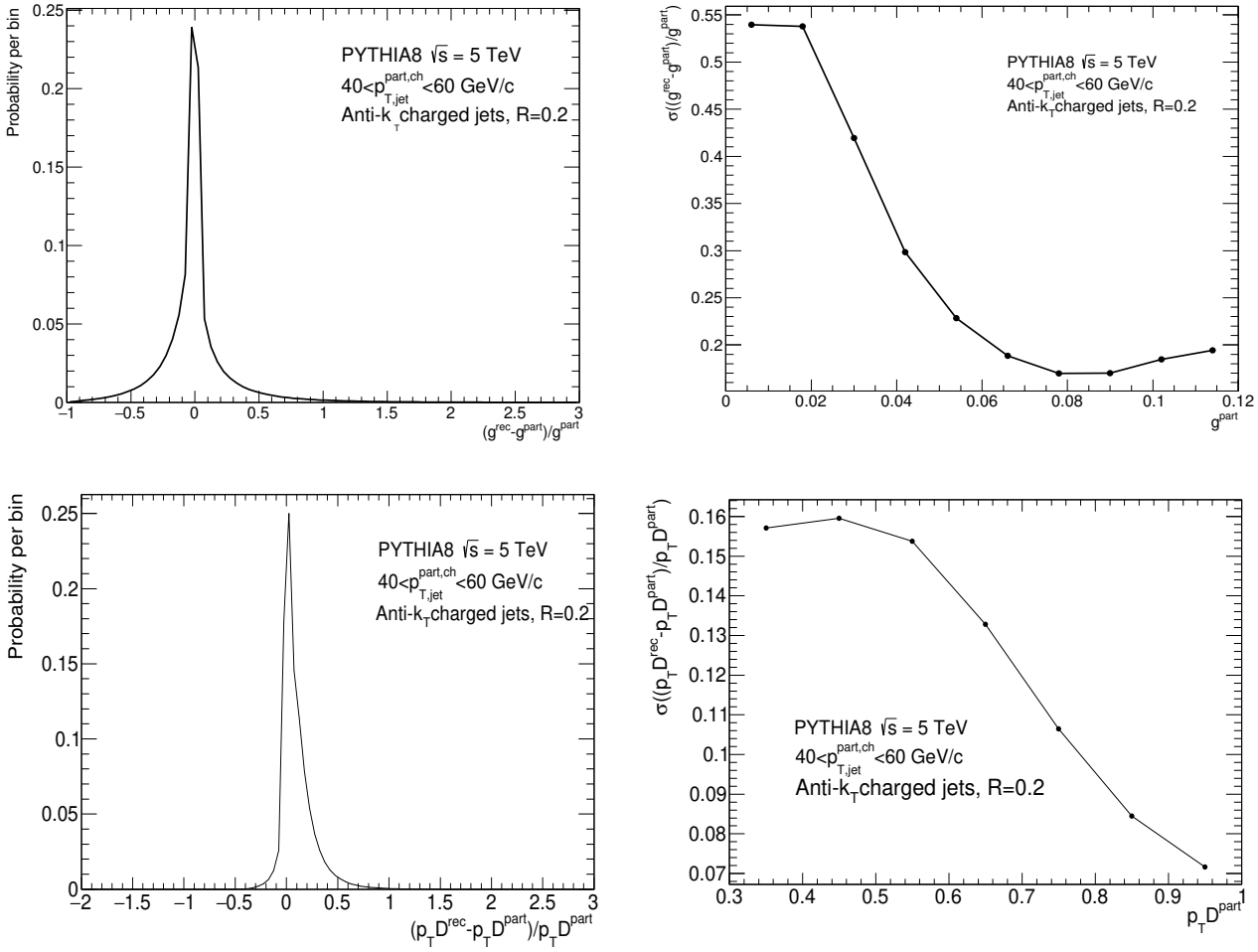

Figure 4.5: (left)Residuals & (right)resolutions of the shape variables in pp for R=0.2 for jets 40 $GeV/c < p_T^{jet,part} < 60$ GeV/c for angularity and dispersion

improves when p_TD tends to one for the harder jets. For g, the resolution is poor at low angularities because of more collimated jets having fewer constituents. At higher angularities the resolution

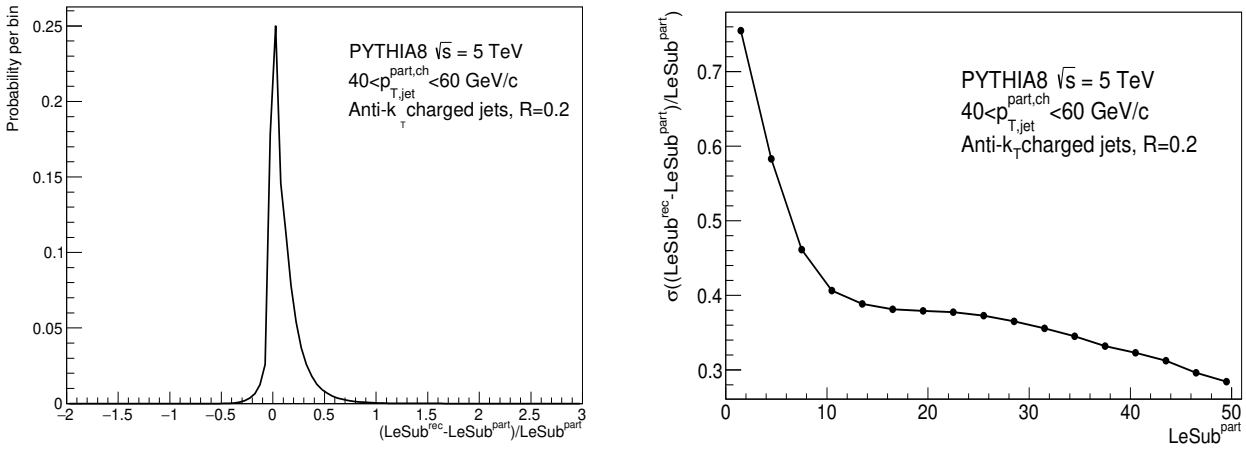

Figure 4.6: shapes residuals(left) & resolutions(right) of the shape variables in pp for R=0.2 for jets 40 $GeV/c < p_T^{jet,part} < 60$ GeV/c for LeSub

improves. Similarly for LeSub, the resolution improves at higher values of the shape variable and worsens at the lower values due to the detector effects.

4.7 Ingredients of the unfolding

As mentioned in Sec 4.3 and 4.6, the probability is calculated using Bayes' theorem using a prior distribution and response matrix. This probability is then multiplied with the measured distribution to obtain the true distribution. Therefore we need the following elements to unfold our 2D shape variables.

(a) raw measured 2D shape variable with Jet p_T ($p_{T,jet}^{raw}$ vs $shape^{raw}$)

(b) A 4D response matrix ($shape^{part}$,$p_{T,jet}^{part}$,$shape^{reco}$,$p_{T,jet}^{reco}$)

(c) A 2D prior distribution

(d) The kinemetic efficiency, that corrects the unfolded yield for lost contributions from measured spectrum beyond the reconstructed limit, which has been shown in Fig 4.7. The kinematic efficiency is defined as, $\varepsilon = \frac{N_{matched}^{p_{T,det}^{jet}=20-80GeV/c}}{N_{matched}^{p_{T,det}^{jet}=0-160GeV/c}}$ where symbol N indicates number of jet in particular jet p_T bin. (e) The jet finding efficiency which includes the probability that, for a true jet in the

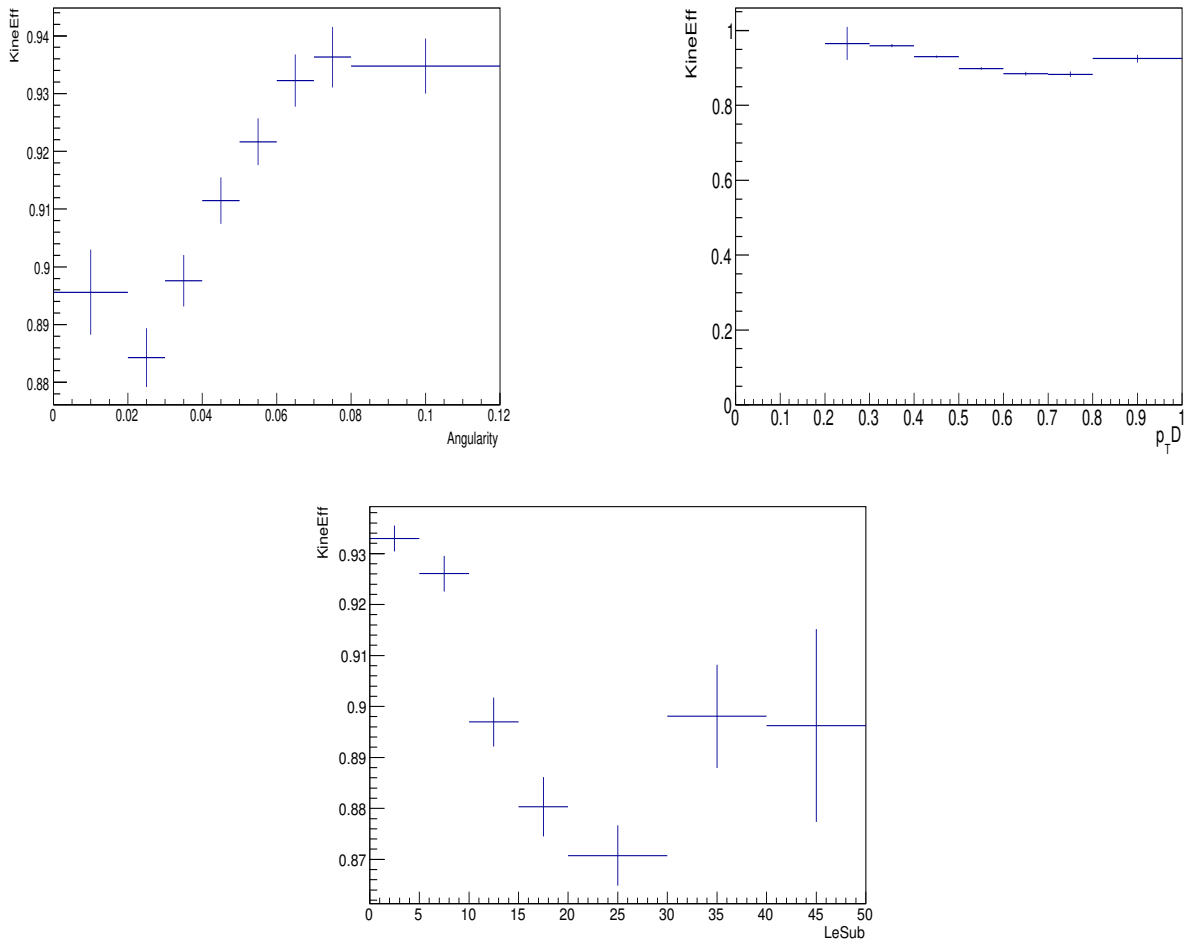

Figure 4.7: Kinematic efficincies for the shape variables in pp collisions for R=0.2 in corrected (true) jet p_T bin of 40 GeV/c - 60 GeV/c and for a raw measurd range of 20 GeV/c - 80 GeV/c ..

acceptance, the reconstructed jet is also in the acceptance.

4.8 Unfolding performance tests in pp for R=0.2

In Fig. 4.8, the unfolded solutions for different iterations are compared to the raw distribution. It is seen that the unfolding iterations change the shape significantly and the solution converges above four iterations. So we choose four as the default number of iterations. The stability of

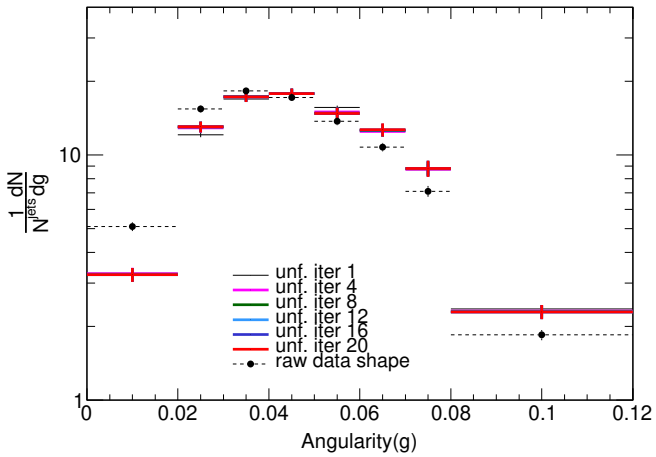

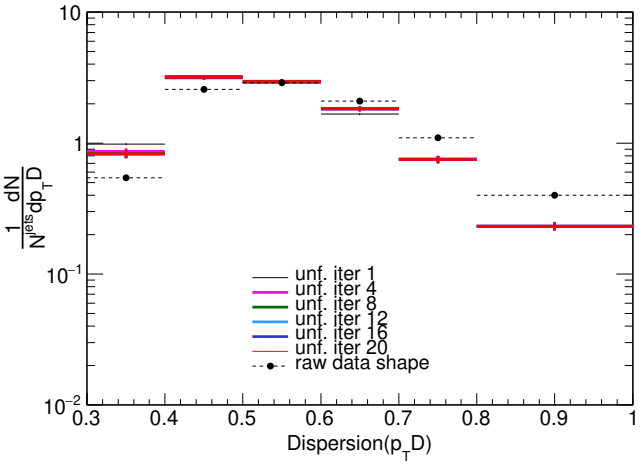

the unfolding is checked by refolding the solution back and checking its agreement with the raw distribution. The refolding is the reverse process of unfolding where, the unfolded solution is fed to the input and the raw distribution is obtained at the output. The refolding of the unfolded

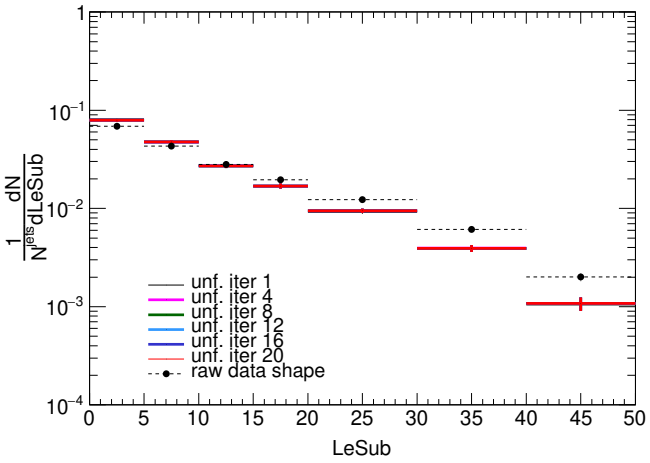

Figure 4.8: Unfolded shape variables compared to the distribution of the raw shape variables in pp collisions for R=0.2 in bin of jet p_T = 40 GeV/c - 60 GeV/c

solution at each iteration, is divided by the raw distributions as shown in fig 4.9 and the ratios are compared to the bin by bin relative statistical errors in the raw distributions. As these are two-dimensional observables, the refolding test is done both for the shape variables and the jet p_T separately shown in Fig. 4.9 and 4.10. As seen from the figures, the difference is within 5% including the error bar for iteration 4 in all the bins. The difference is quite large after the first iteration as expected.

To test the stability of the unfolding procedure, a closure test has also been performed where, the unfolding input is filled with the MC information. The MC information which is used to fill the input is expected to be statistically independent from the sample that is used to fill the response (typically input contains 3% and the response 97% of the MC sample). The performance is validated from the ratio of the unfolded solution to the true MC as shown in Fig.4.11 & 4.12 and the ratio of the refolded solution to the raw as shown in 4.13 & 4.14. As seen from Fig. 4.11 & 4.13, the difference between unfolded(refolded) solution and the true(raw) value is found to be within 5% for iteration 4 for the shape variables in all the bins and it increases for smaller and higher iterations which indicates a reasonable validation of the closure test for iteration 4. The

closure test of p_T^{jet} shows a good agreement between unfolded(refolded) solution and true(raw) value in the region 40-60 GeV/c shown in Fig. 4.12 & 4.14 which is the final result of this thesis.

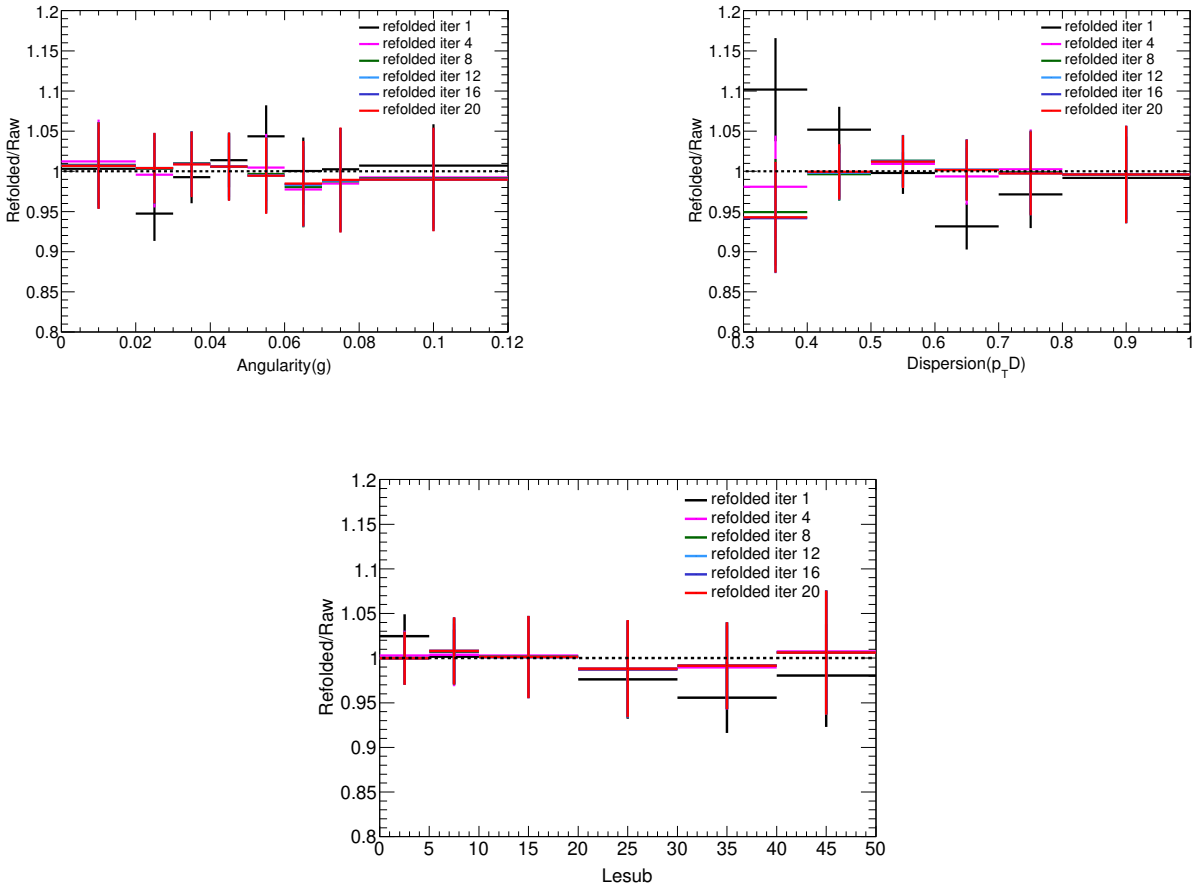

Figure 4.9: Ratio of the refolded shape variables to the raw values for different regularizations in pp collisions for R=0.2 for jet p_T = 40 GeV/c - 60 GeV/c

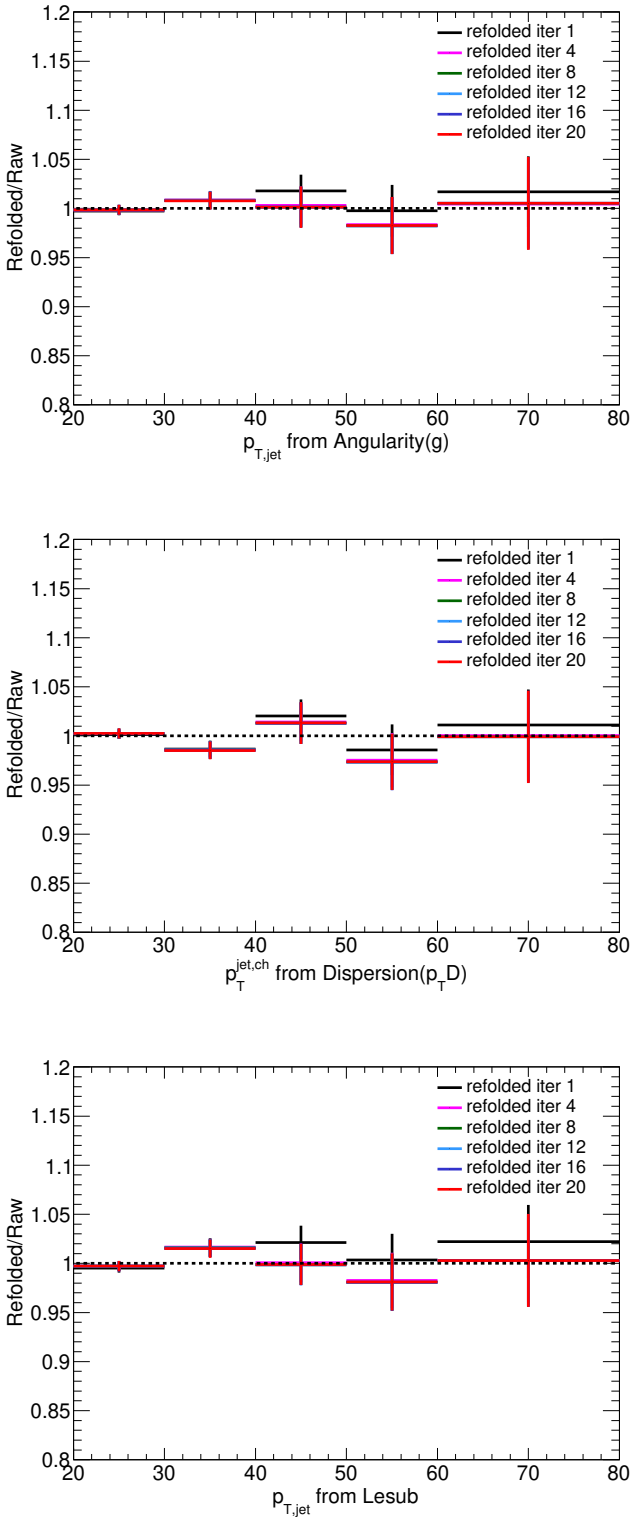

Figure 4.10: Ratio of the Refolded $p_{T,jet}$ relative to the raw values in pp collisions for R=0.2 in the bin of jet p_T = 40 GeV/c - 60 GeV/c

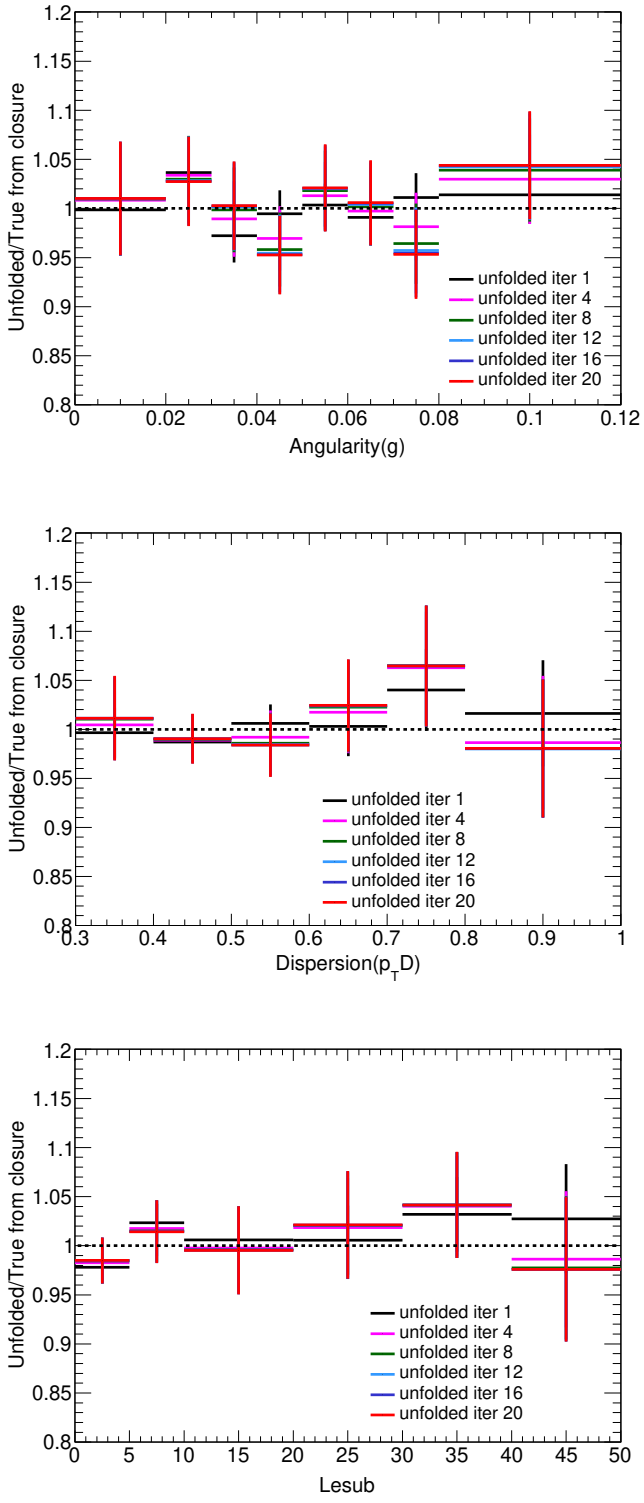

Figure 4.11: Closure Test: Unfolded distributions of the shape variables compared to the true shape distribution represented by the ratio in pp collisions for R=0.2 in jet p_T bin of 40 GeV/c - 60 GeV/c

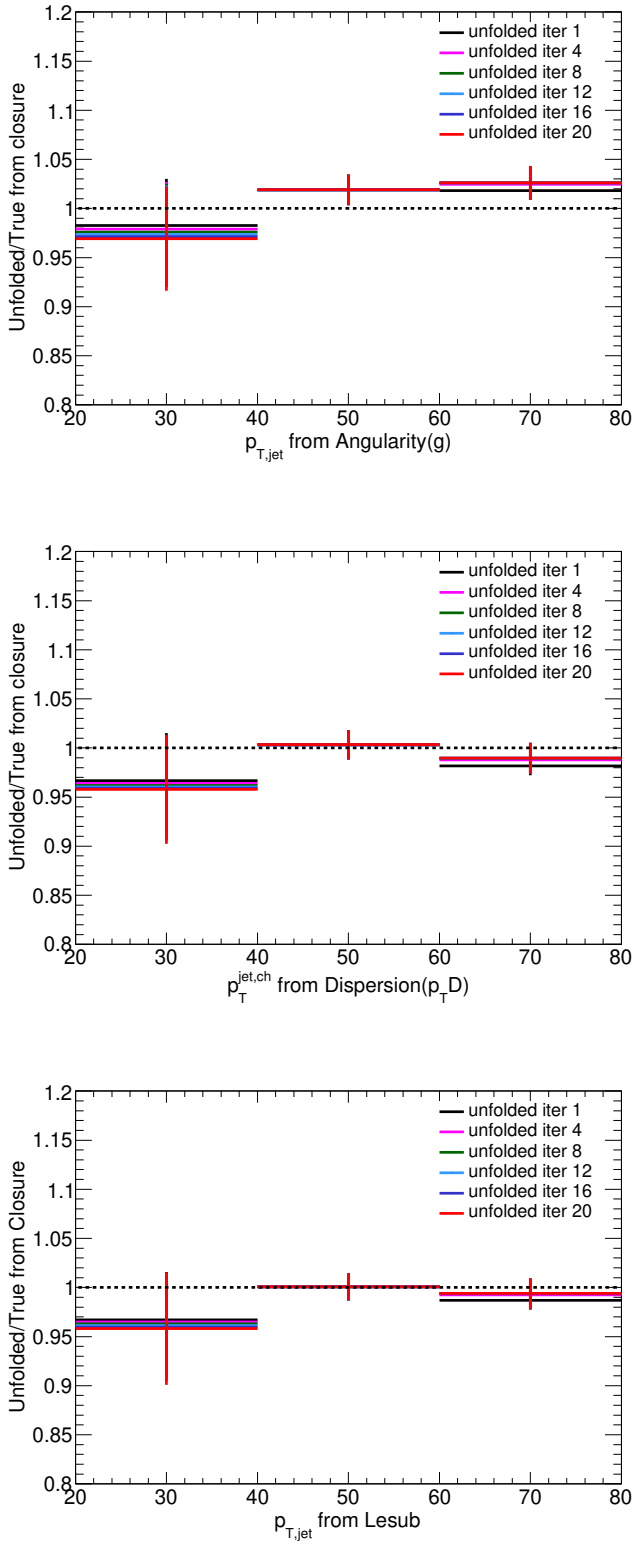

Figure 4.12: Closure test: Unfolded compared to true p_T jet distributions in pp collisions for R=0.2

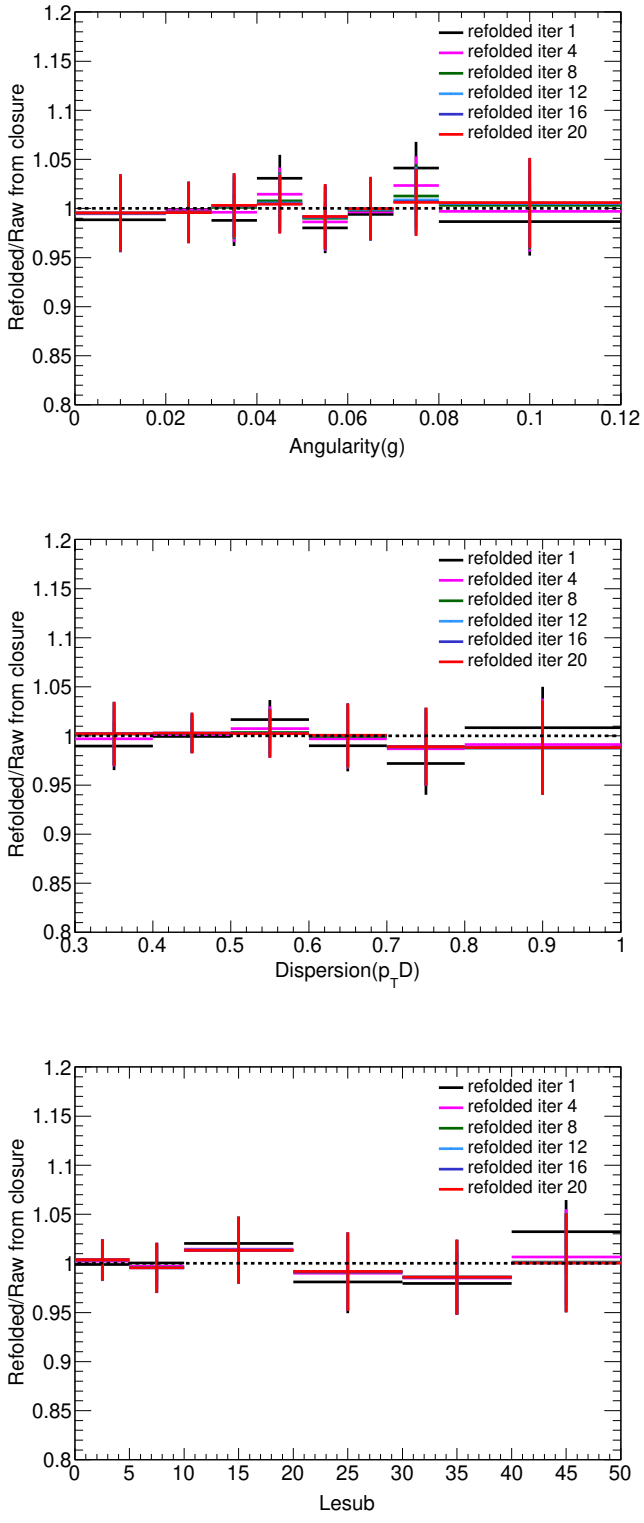

Figure 4.13: Closure Test: Refolded compared to raw shape distributions in pp collisions for R=0.2 in bin of jet p_T 40 GeV/c - 60 GeV/c

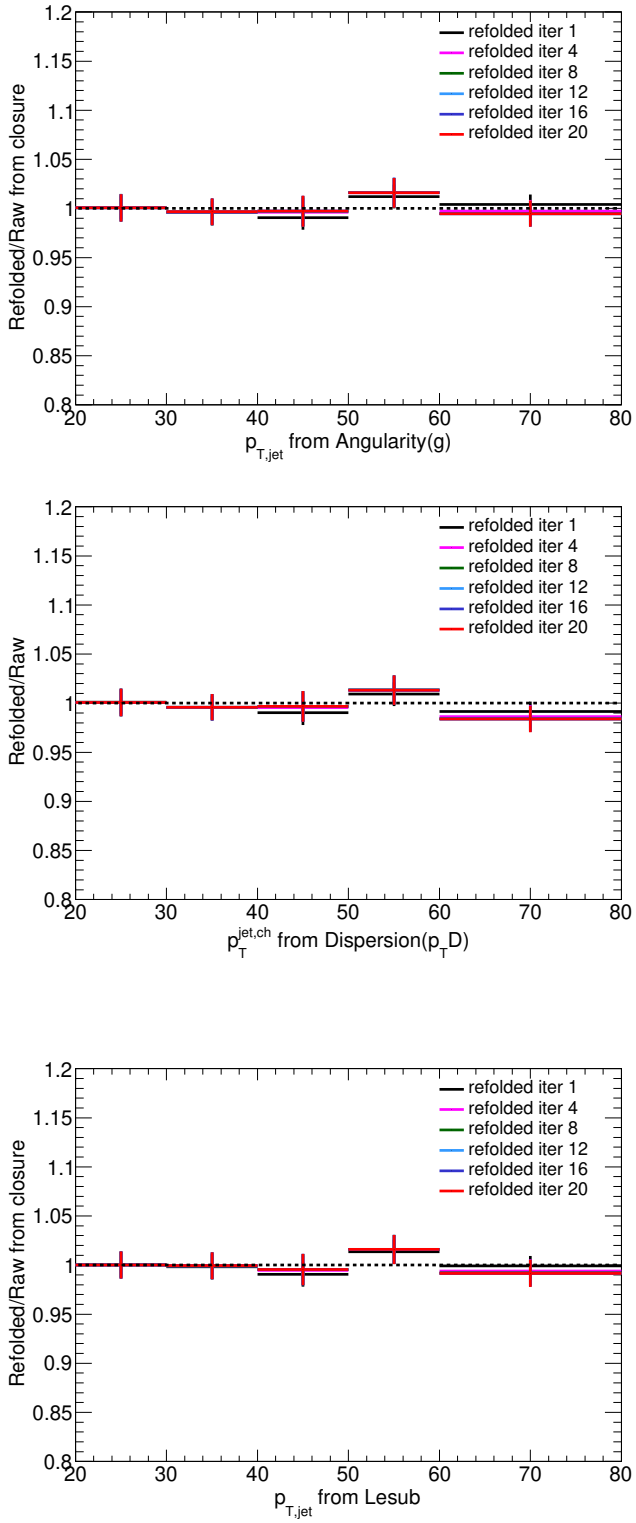

Figure 4.14: Closure test: Refolded compared to raw p_T jet distributions in pp collisions for R=0.2

4.9 Unfolding performance tests in pp for R=0.4

As has been done earlier for R=0.2, unfolding has also been performed for R=0.4 and to check its validity, the closure test has been performed with unfolded and refolded distributions. The results along with the kinematic efficiencies are shown below. The difference between refolded(unfolded) and raw(true) shape variables is larger than those of $R = 0.2$ in some bins, however, the difference is within 5% for iteration 4 in all the bins as shown in Fig. 4.16 and 4.18. The difference between unfolded and true p_T^{jet} is within 5% except for the first bin where it goes beyond 10% as shown in Fig. 4.19. The large disagreement in the first bin needs further investigation. However, the final results of this analysis are for $40 < p_T^{jet} < 60$ GeV/c which satisfies the closure test reasonably.

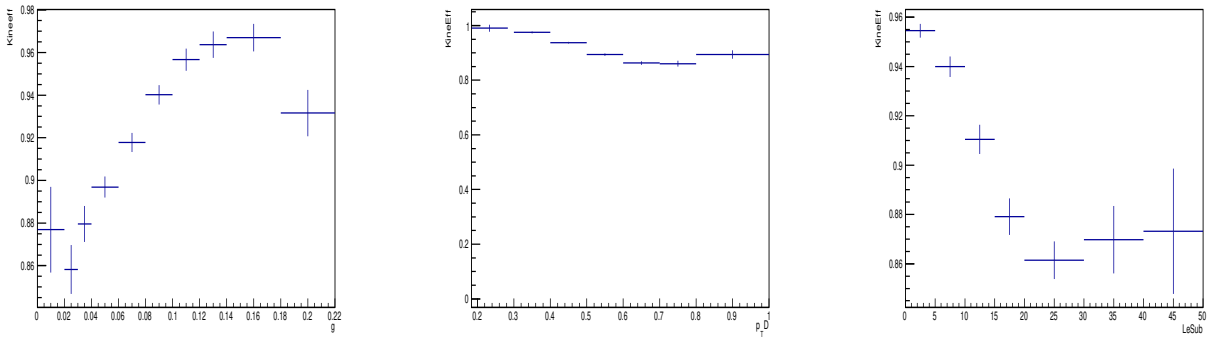

Figure 4.15: Kinematic efficincies for the shape in pp for R=0.4 in corrected (true) jet p_T bin of (40.60) and for a raw measurd range of (20,80) GeV/c.

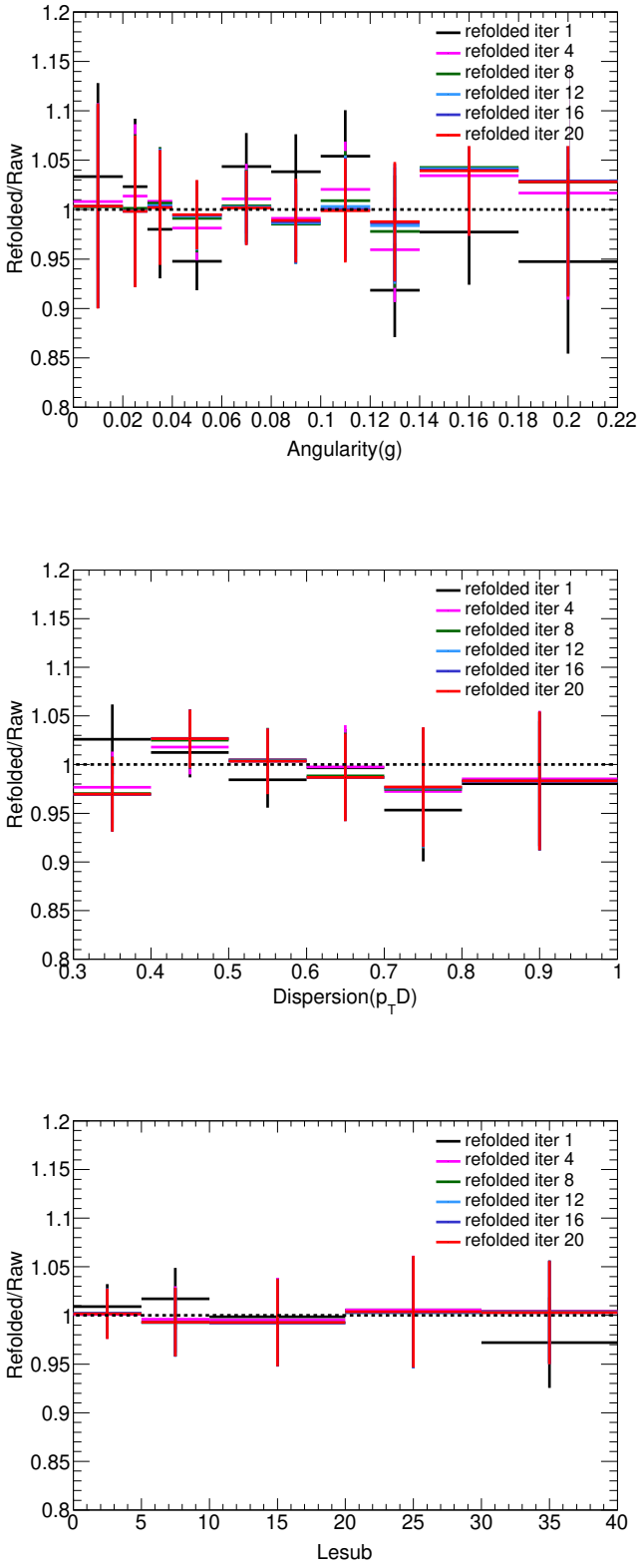

Figure 4.16: Ratio of the Refolded shape variables relative to the raw distributions for different regularizations in pp data for R=0.4 in the jet p_T bin of 40 GeV/c - 60 GeV/c

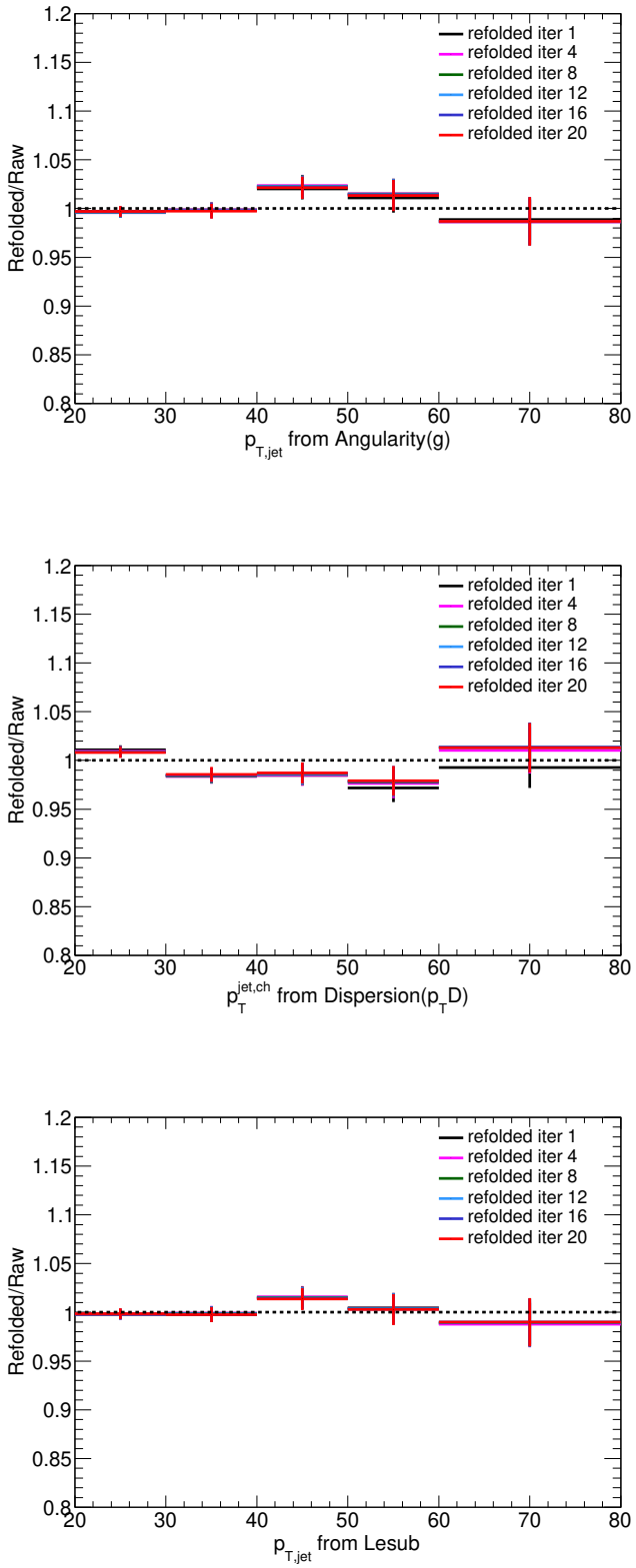

Figure 4.17: Ratio of the Refolded $p_{T,jet}$ relative to that in raw distributions in pp data for R=0.4 in bin of jet p_T = 40 GeV/c - 60 GeV/c

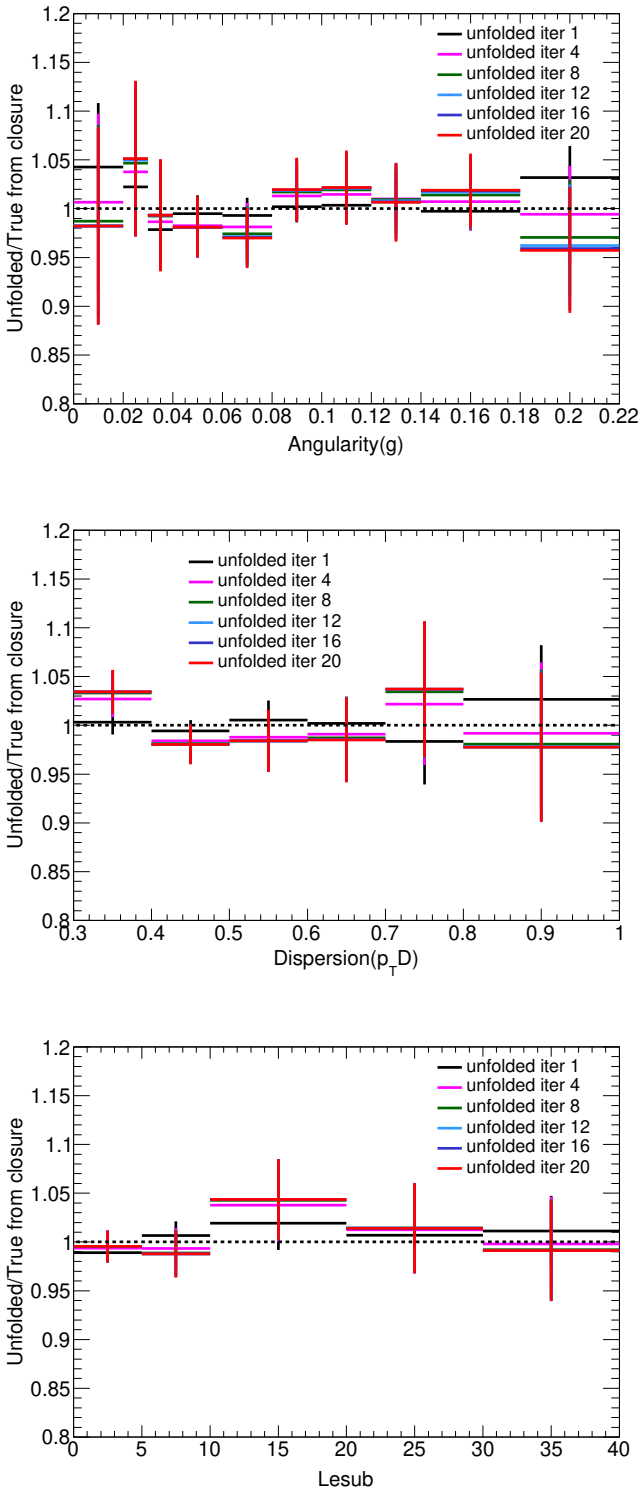

Figure 4.18: Closure Test: Unfolded distributions of the shape variables compared to the true shape distribution represented by the ratio in pp collisions for R=0.4 in jet p_T bin of 40 GeV/c - 60 GeV/c

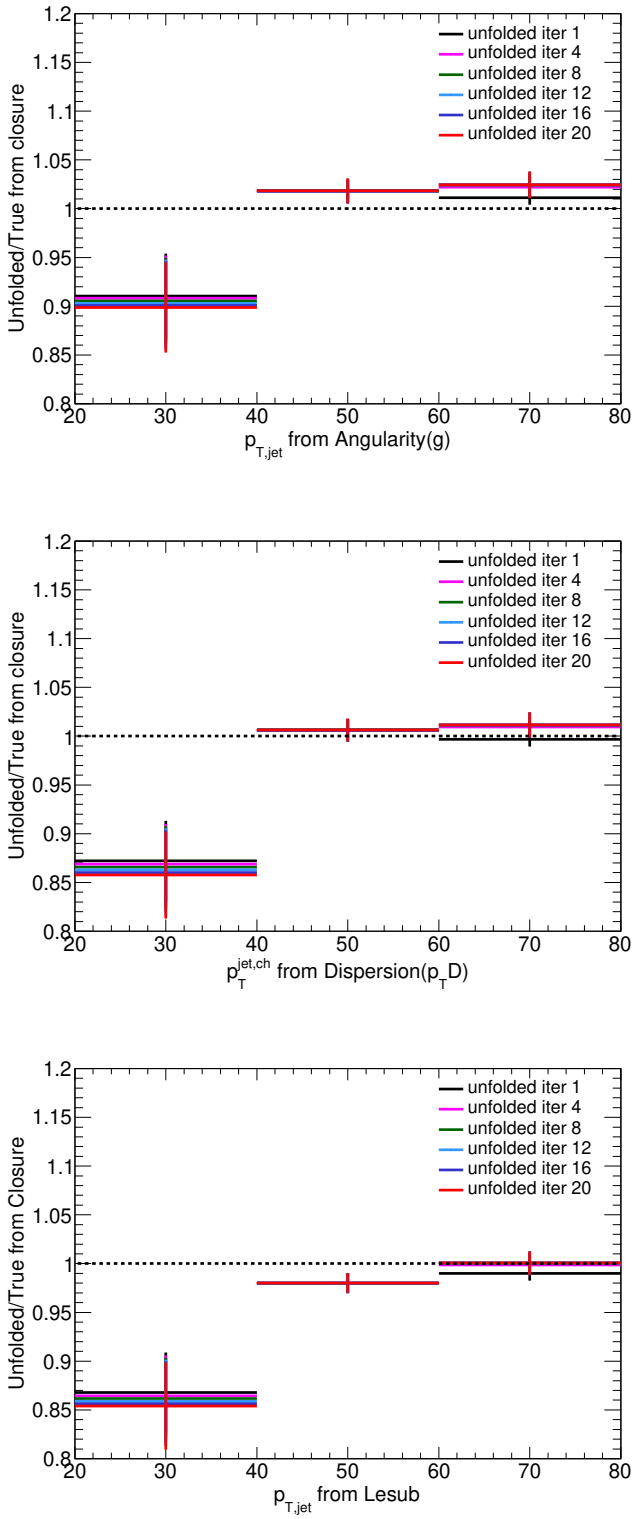

Figure 4.19: Closure test: Unfolded distributions compared to the true p_T distributions in pp collisions for R=0.4

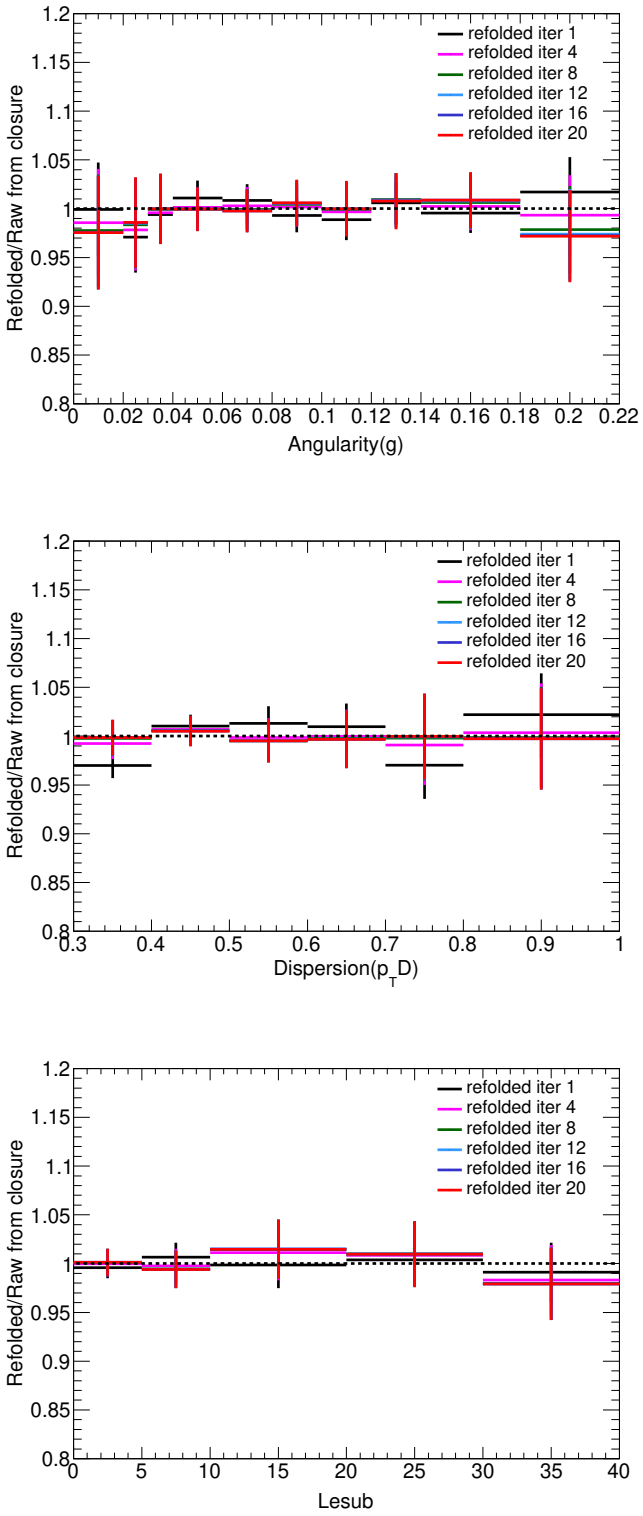

Figure 4.20: Closure Test: Ratio of the refolded shape variables compared to the raw values in pp data for R=0.4 in bin of jet p_T 40 GeV/c - 60 GeV/c

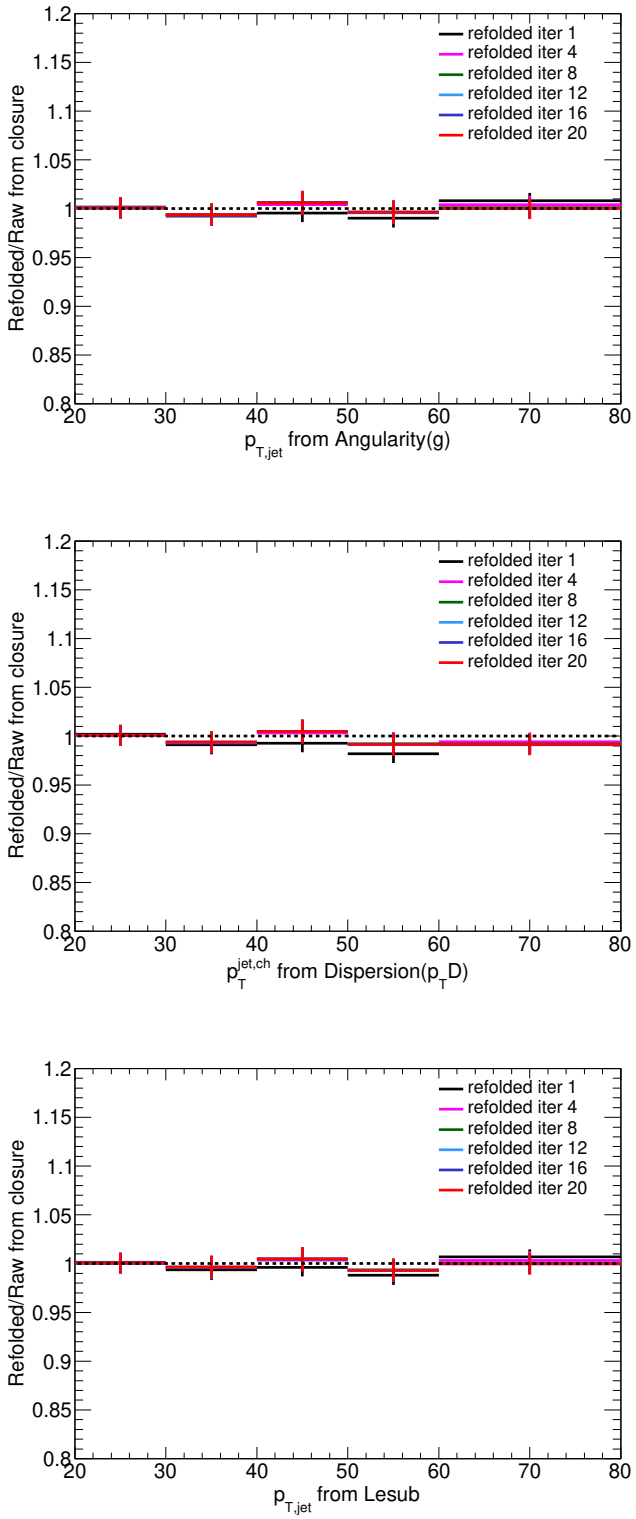

Figure 4.21: Closure test: Refolded distributions as compared to the raw jet p_T in pp data for R=0.4

4.10 Estimation of bin to bin correlation work the Pearsons coefficients in pp collision data

After the unfolding, the bins may get correlated with each other. The value in any bin of the unfolded distribution is dependent on the full measured distribution. The Pearson correlation coefficient is defined as the degree of (anti)correlation between the unfolded bins of the shape variables. It is a measure of the correlation between two bins in the unfolded result. It is defined by [13] $p_{i,j} = \frac{cov(i,j)}{\sigma_i \sigma_j}$ i,j are two bins. It has the value between -1 to +1, the value of ± 1 corresponds to the strongest possible correlation (anti-correlation) between the bins and 0 means no correlation. A bin is correlated with itself, so the coefficient value for the diagonal elements will be ≈ 1 and also there will be a small correlation among the neighbouring bins. Any large deviation from zero corresponds to a smearing rather than unfolding due to either too small or too large number of iterations and the result is far from the true distribution. A strong correlation will cause a potential bias in the result and anti-correlation will cause large statistical fluctuation. The more the coefficient tends towards zero, the less will be the uncertainty and correlation between the bins. Fig 4.22 and 4.23 shows the correlations between the unfolded bins of the three jet shapes variables for R=0.2 and R=0.4 respectively. The X and Y axes in the figures represent the corresponding bin number for finding the correlation and Z axis represents the values of pearson coefficient.

It is clearly seen from the Fig 4.22 and 4.23 that, each bin is strongly correlated with itself only and it shows a very poor correlation with the other bins i.e. the pearson coefficient is nearly 1 for all the shapes. It signifies that the unfolding has been done properly. If a bin would show correlation with its neighbouring bin, it would mean that the unfolding was not properly done.

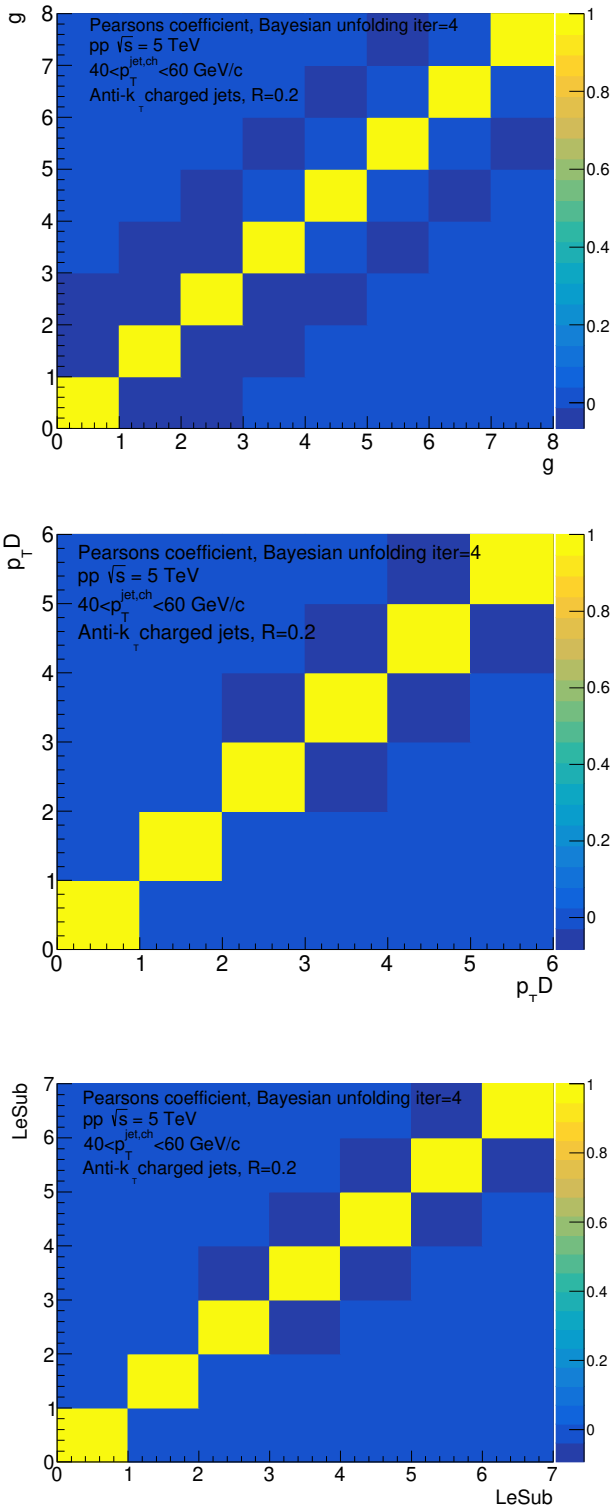

Figure 4.22: Correlation between the unfolded bins of g, $p_T D$ and LeSub in pp for R=0.2 and jet p_T of 40 GeV/c -60 GeV/c for default iteration = 4. The X and Y axes represent the bin numbers.

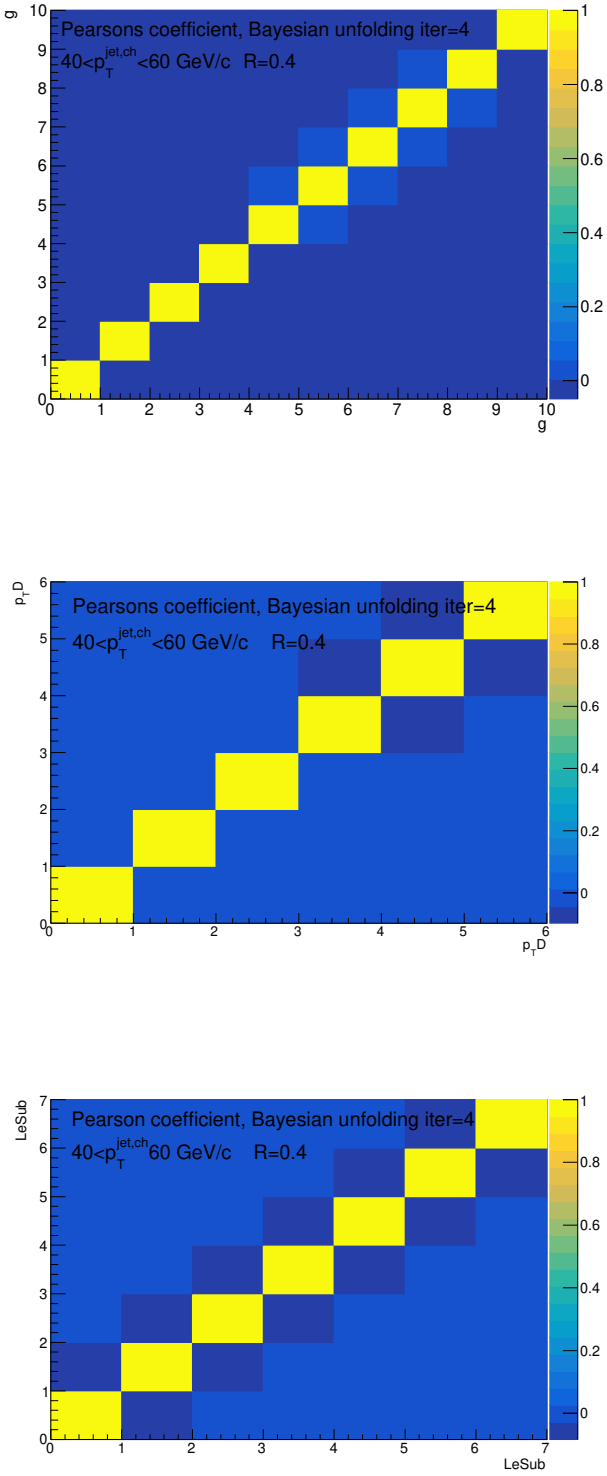

Figure 4.23: Correlation between the unfolded bins of g, $p_T D$ and LeSub in pp for R=0.4 and jet p_T of 40 GeV/c - 60 GeV/c for default iteration = 4. The X and Y axes represent the bin numbers.

4.11 Sources of systematic uncertainties in pp

Systematic uncertainty is estimated by varying the parameters used in the analysis within a reasonable value. The sources of uncertainty in determination of the shape observables in this analysis are discussed below.

(1) Tracking efficiency : The uncertainty in the tracking efficiency comes due to the limited detector acceptance resulting in varying number of space points in the work and other detector effects. Variation of 4% is considered in this dataset, the response matrix is modified accordingly and the shape observables are calculated. The difference between the modified result and the original result give the systematic uncertainty.

(2) Regularisation: It is given by the number of iterations after which the solution converges. The standard regularization parameter is such that the deviation between unfolded and true observable is smallest. It is seen that the difference is within 5% after 4 iterations. So the default number of iterations is considered as 4 and we vary it to 3 and 7 for estimation of the systematic uncertainty.

(3) Truncation: The minimum accepted jet p_T chosen in this analysis is 20 GeV/c. For systematic study, the lower limit has been trunctaed to 10 GeV/c. It checks how the results change with the contamination from combinatorial jets that are more in lower p_T.

(4) Prior: As mentioned in the unfolding section, a prior is a base distribution for the unfolding to start the iteration which should be similar to an expected true distribution. The prior in the 2D Bayesian implementation of RooUnfold was taken as the projection of the response matrix onto the true axes. Our default prior is Pythia-8. We consider the ratio between the default unfolded solution and default prior. This ratio is a 2D correction factor that we apply as a weight to the response prior to the unfolding such that the prior coincides with the unfolding solution. The systematic uncertainty we obtain by the difference between the unfolded solution with Pythia-8

and the corrected solution.

(5) Binning: We consider a variation of the binning in the measured input. For Angularity we consider the alternative binning: 0.022,0.032,0.042,0.052,0.062,0.072,0.081,0.12, for dispersion we consider the alternative binning: 0.32,0.42,0.52,0.62,0.72,0.81,1 For LeSub we consider the alternative binning: 0,5.25,10.25,15.25,20.5,30.5,40.

The components of the uncertainties are then added in qudrature. The different components of the systematic uncertainties, for the different shapes, measured in pp collisions are shown in Table .4.1. Fig 4.24 shows the relative systematic uncertainties from different sources in angularity(g),

Shape	g			p_TD			LeSub		
	0-0.02	0.05-0.06	0.08-0.12	0.3-0.4	0.5-0.6	0.8-1	0-5	20-30	40-60
Tracking(%)	10.59	3.61	7.93	11.98	1.54	5.99	2.69	2.93	11.49
Prior(%)	3.44	1.95	9.64	25.34	3.05	9.72	3.24	4.43	9.16
Reg.(%)	+1.48 -1.20	+0.81 -0.60	+0.03 -0.15	+3.12 -2.24	+0.06 -0.34	+0.71 -0.83	0.01 0.07	0.58 0.48	0.72 0.62
Truncation(%)	0.67	0.53	1.43	3.46	1.68	5.67	1.32	2.97	5.78
Binning(%)	0.78	2.25	2.69	1.94	0.75	0.11	3.40	3.14	14.23
Total(%)	+11.28 -11.25	+4.77 -4.74	+12.84 -12.85	+28.47 -28.39	+3.88 -3.89	+12.76 -12.77	+5.57 -5.57	+6.87 -6.86	21.26 -21.26

Table 4.1: Relative systematic uncertainties on the measured jet shape variables in pp collisions for three selected jet shape intervals in the jet $p_{T,jet}^{ch}$ range of 40-60 GeV/c

dispersion ($p_T D$) and LeSub for R=0.2. The largest contributions to the relative uncertainties in g, $p_T D$ and LeSub come from the tracking efficiency, prior and statistics respectively and the values are 10% , 25% and 15% respectively. The same is shown for R=0.4 in Fig 4.25 where it is seen that, the maximum uncertainty comes from the tracking efficiency in all three shapes with the values of about 20%, 18% and 10% respectively.

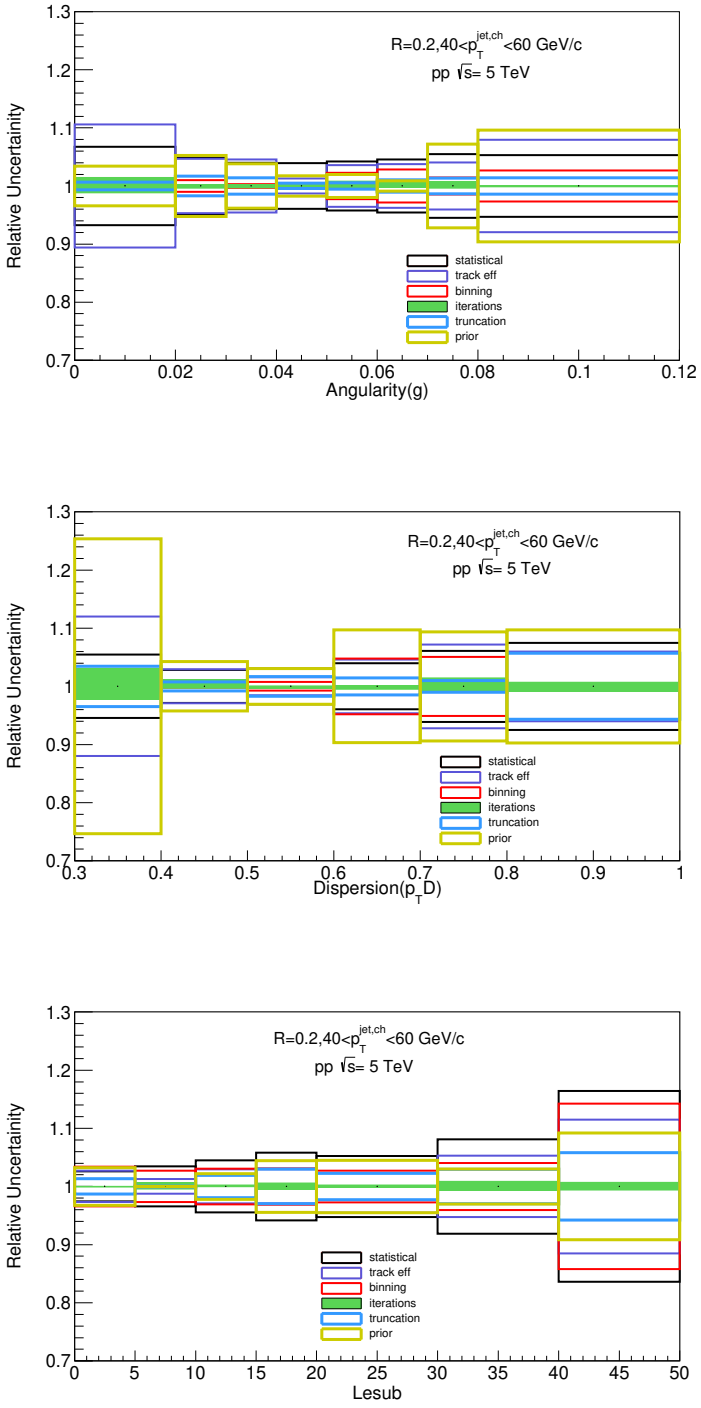

Figure 4.24: Relative systematic uncertainties from various sources in pp data for R=0.2 in jet p_T bin of 40 GeV/c - 60 GeV/c

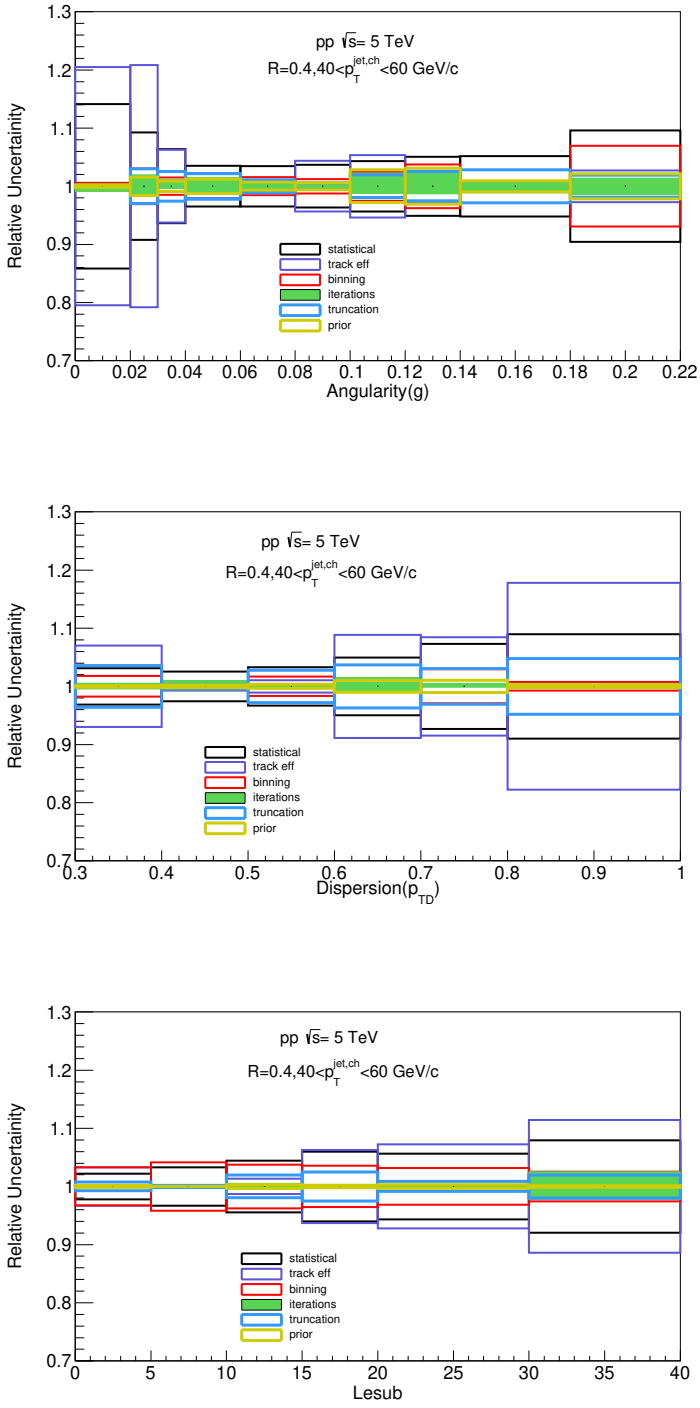

Figure 4.25: Relative systematic uncertainties from different sources in pp data for R=0.4 in jet p_T bin of 40 GeV/c - 60 GeV/c

4.12 Variation of jet shape with R and p_T^{jet}

Three jet shape observables have been plotted with R =0.2, 0.4 and 0.7 for $40 < p_T^{jet} < 60 GeV/c$. Fig 4.26 shows that the angularity shifts to the higher values and dispersion shifts to the lower values with increasing R. This indicates that at higher radius, jets are broadened as increasing radius means more constituents are included in the jet. In Fig 4.27, 4.28 and 4.29, three jet shape observables are plotted for different jet p_T ranges with R=0.2, 0.4 and 0.7 respectively. It is seen that, for each radius, the angularity corresponding to higher p_T jets shifts to lower value i.e. the jets are found to be more collimated. $p_T D$ also shows similar trend of broadening most prominently for R=0.2 & R=0.4.

Among the results presented in this section, only the results with R=0.2 and R=0.4 for jet p_T=40-60 GeV/c are the final results. The results for R=0.7 and those for jet p_T=20-40 GeV/c and 60-80 GeV/c need further investigations as the closure test is not valid in these cases.

4.12.1 Unfolded Jet shape variables with different R for 40< $p_{T,jet}$ <60 GeV/c

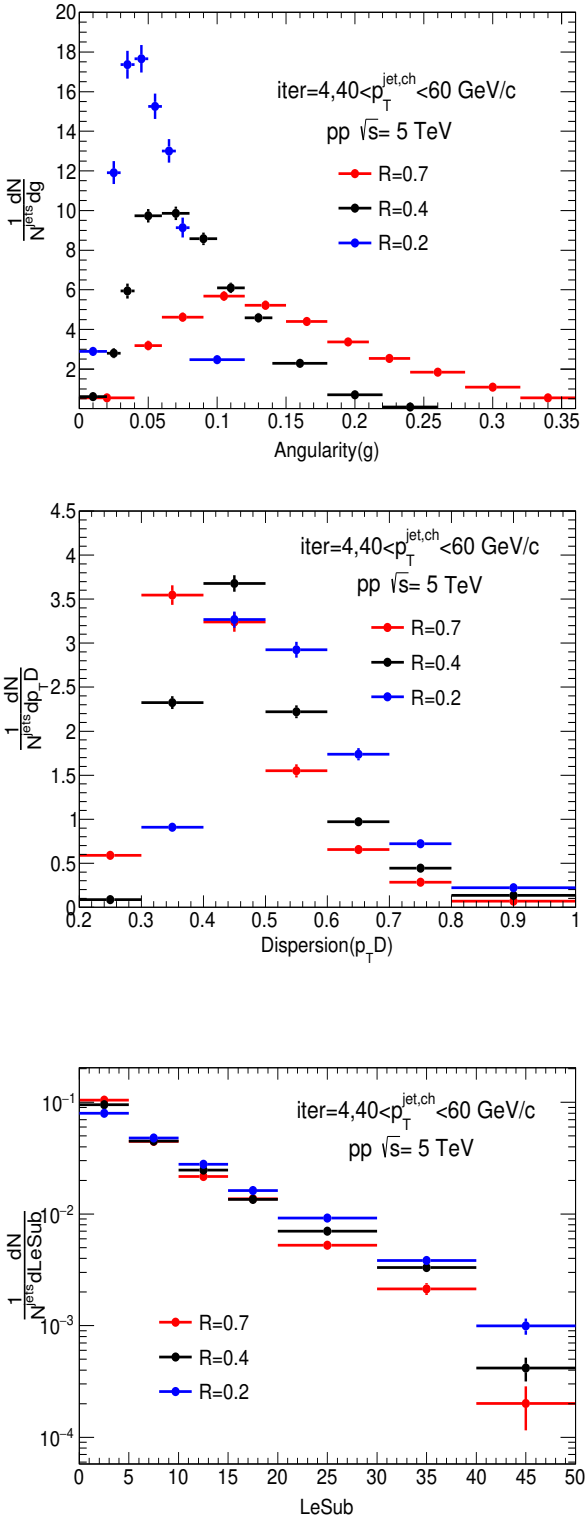

Figure 4.26: Unfolded shape distributions in pp data for R=0.2,0.4 and 0.7 in jet p_T 40-60 GeV/c

4.12.2 Unfolded jet shape variables with different jet p_T bin for R=0.2

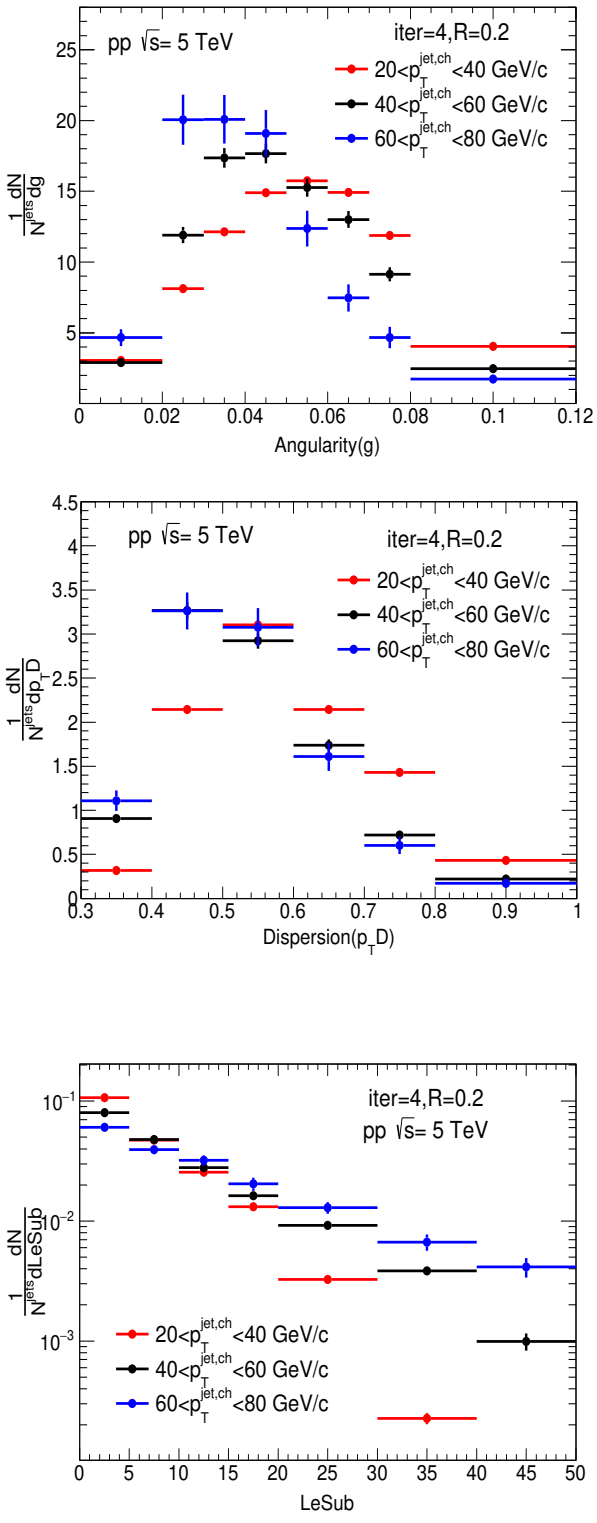

Figure 4.27: Unfolded shape distributions in pp data for R=0.2 in various jet p_T bin

4.12.3 Unfolded jet shape variables with different Jet p_T bin for R=0.4

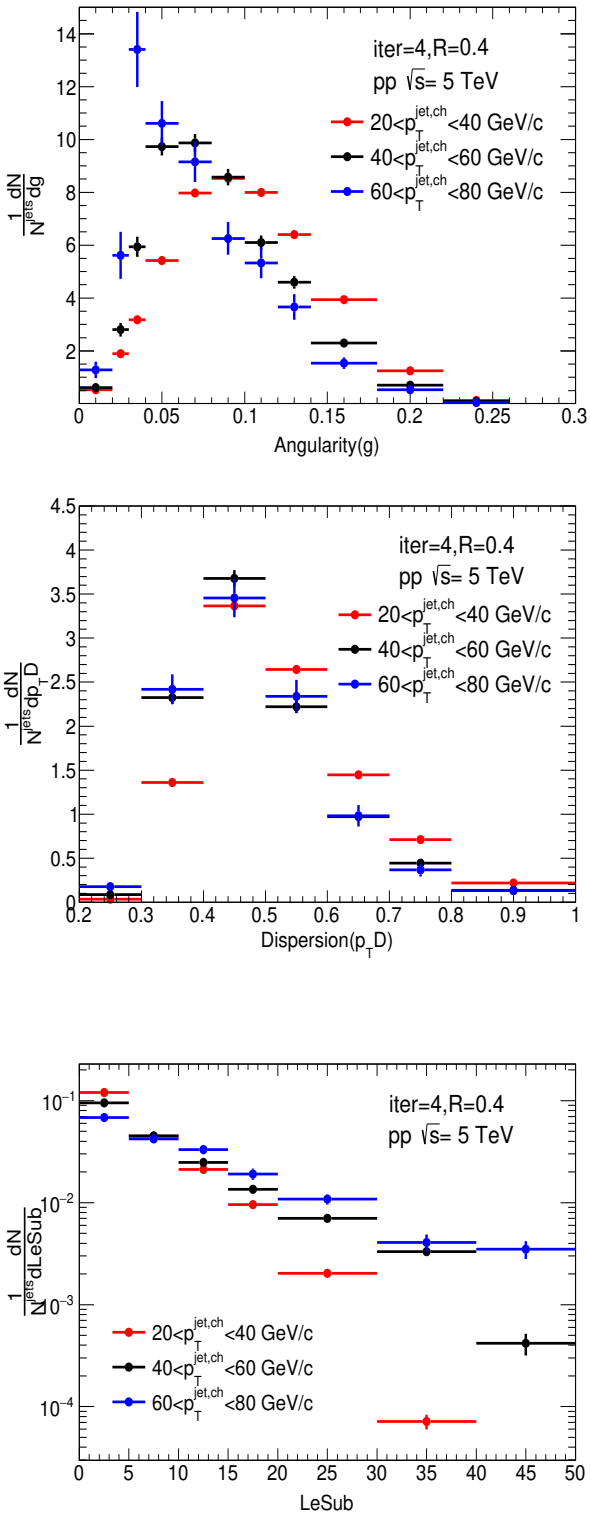

Figure 4.28: Unfolded shape distributions in pp data for R=0.4 in various jet p_T bin

4.12.4 Unfolded jet shape variables with different Jet p_T bin for R=0.7

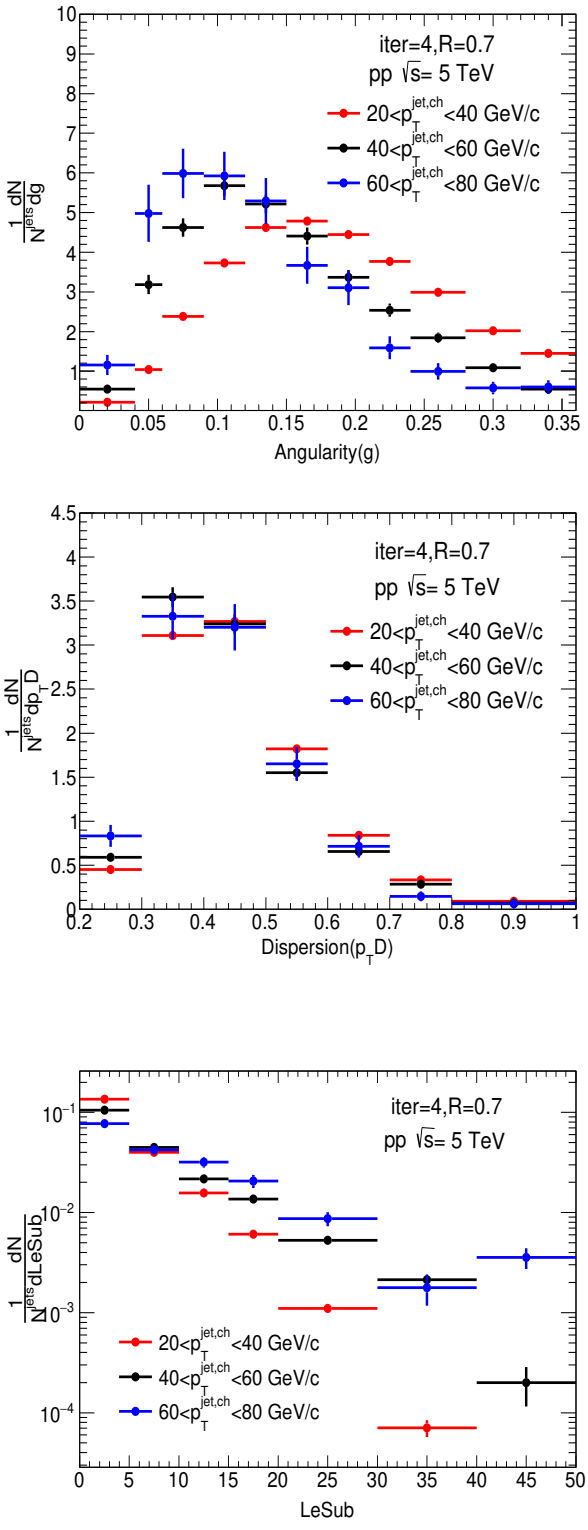

Figure 4.29: Unfolded shape distributions in pp data for R=0.7 in various jet p_T bin

4.13 Jet shape variables with and without implementation of the pileup rejection

There is a possibility of including the soft background particles in the jet when the radius is increased. For this, jet shapes have been studied with pile up rejection criteria to see if any change occurs. We do not observe any significant change in the jet shape(R=0.4) when the pileup cuts are applied. The pileup occurs mainly in pp collisions at high luminosity in which seperation between consecutive collisions is very low. In this work, selection has been applied based on the seperation of the collisions horizontal plane. It has been applied in such a way that the number of interaction per bunch crossing is restricted to 0.06. Residual pile up events are rejected based on multiple vertex finding algorithm using the information from SPD and proper physics selection criteria.

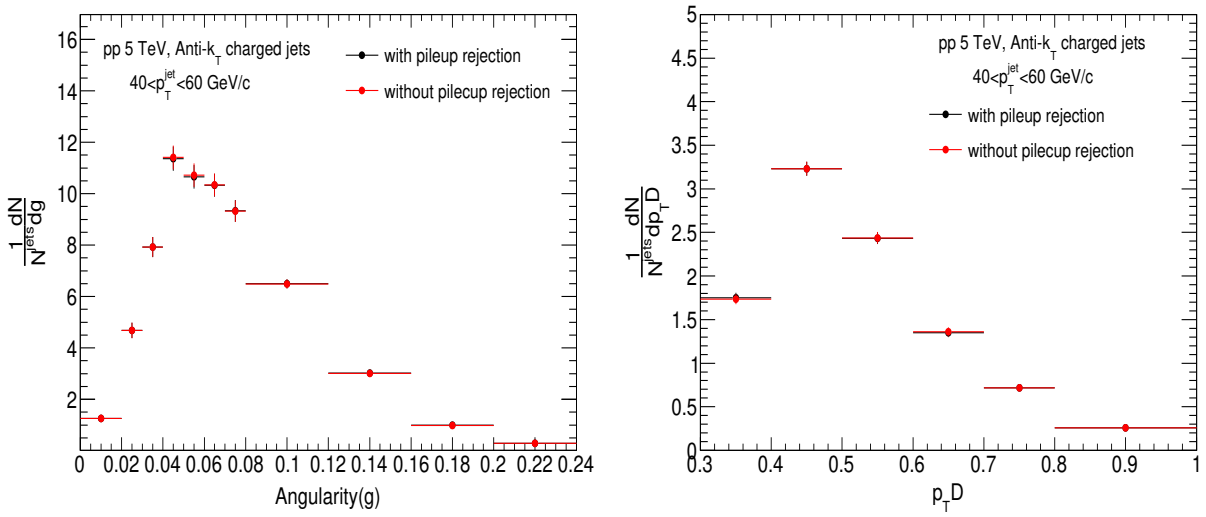

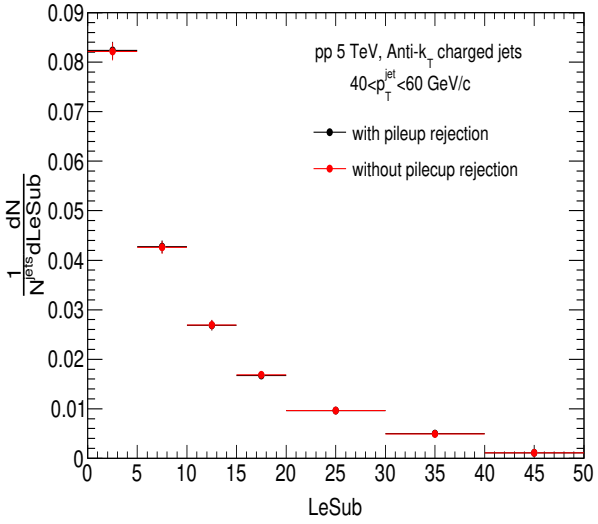

Figure 4.30: Study of pile up contribution for R=0.4 in jet p_T^{jet} bin of 40-60 GeV/c

4.14 Final Corrected results

4.14.1 Fully corrected results for the jet-shape variables in pp collisions at $\sqrt{s}$ = 5.02 TeV and compared with the results for pp collisions at $\sqrt{s}$ =7 TeV for R=0.2

Fig. 4.31 shows the fully corrected results for p+p collisions at $\sqrt{s}$ =5.02 TeV with a comparison to the previous results at $\sqrt{s}$ =7 TeV for R=0.2. We do not observe any significant change in the shape of the distributions.

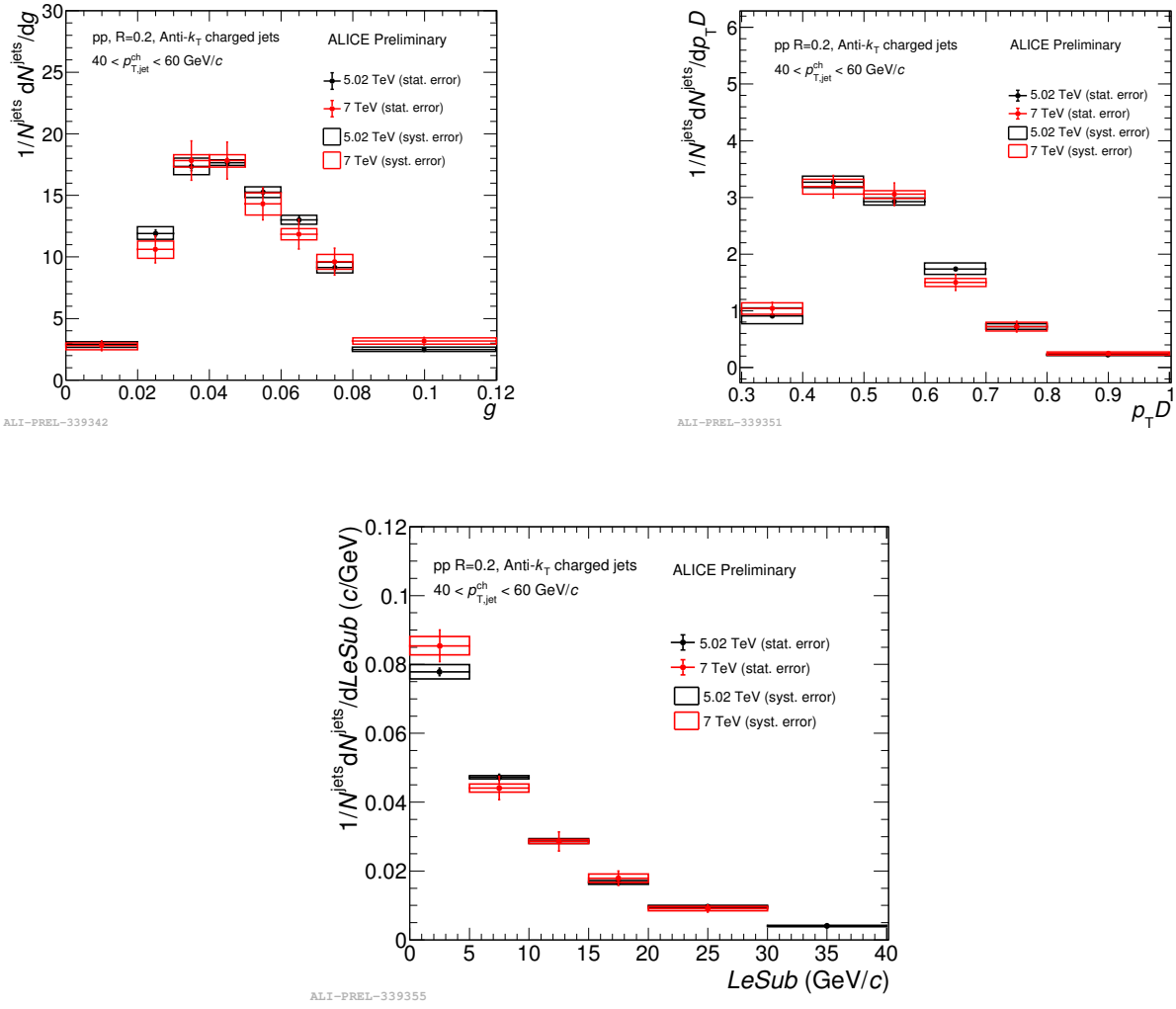

Figure 4.31: jet shape distributions in pp collisions at $\sqrt{s}$ =5.02 TeV for R=0.2 in jet p_T bin of 40 GeV/c - 60 GeV/c compared to the results at $\sqrt{s}$ =7 TeV pp collisions

4.14.2 Jet shape with resolution parameter R=0.2 and R=0.4 for jet p_T 40-60 GeV/c

Fig. 4.32 shows the fully corrected jet shape observables g, p_TD & LeSub in p+p collisions at $\sqrt{s}$ = 5.02 TeV for two resolution parameters R=0.2 and R=0.4. The angularity distribution gets broader for R=0.4 and the peak shifts towards higher value, whereas, the dispersion slightly shifts towards left for R=0.4 which indicates the jet-broadening at higher radius and the small radius jets are fragmented harder at particular jet p_T.

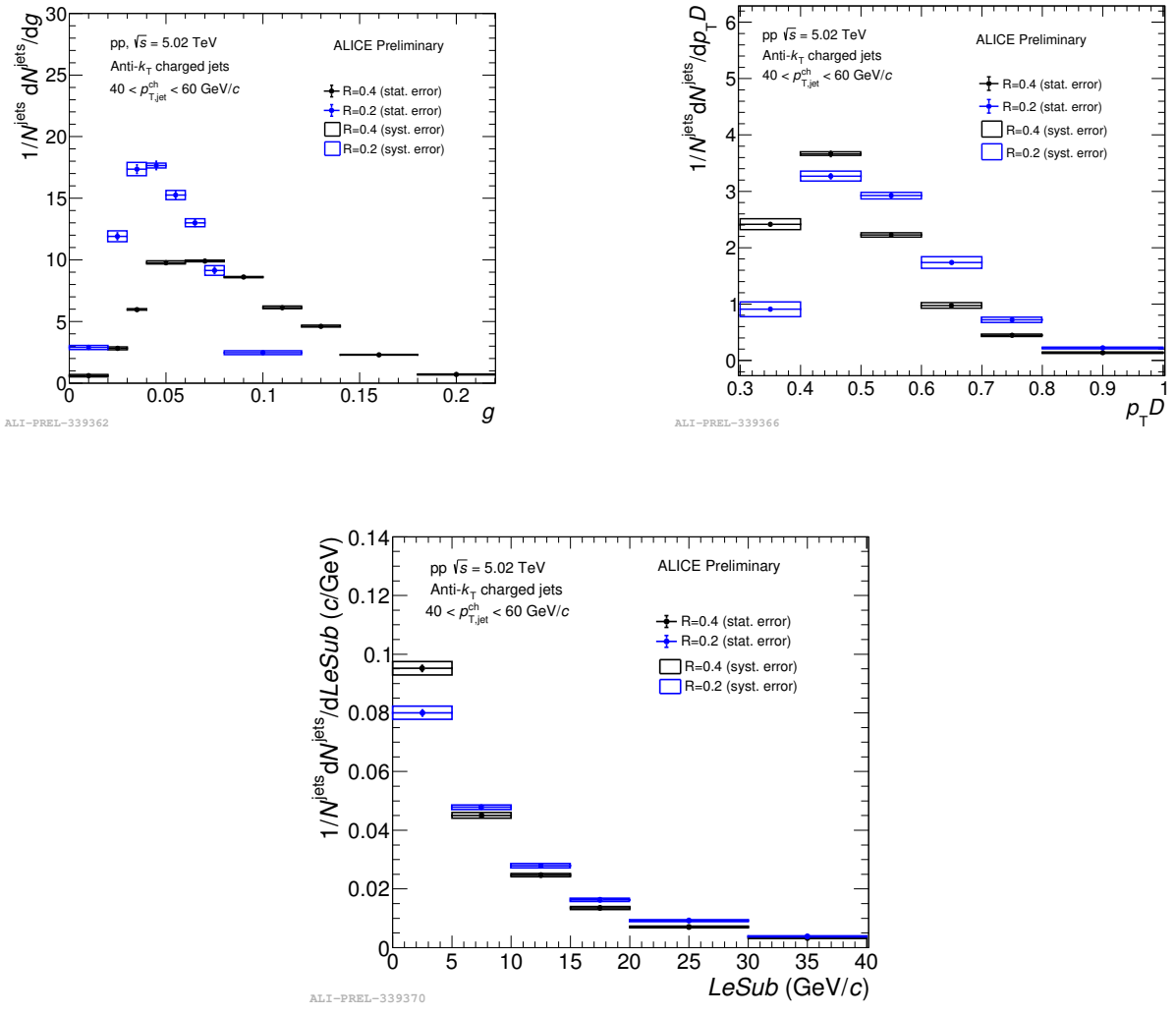

Figure 4.32: jet shape distributions in pp for R=0.2 and 0.4 in jet p_T 40-60 GeV/c

4.14.3 Comparison of Jet shape for R=0.2 and R=0.4 with model

The approved final distribution of g & $p_T D$ for pp collisions at $sqrt_s = 5.02TeV$ have been presented in Fig.4.33 for R=0.2 & R=0.4. The jet shapes for R=0.2 and R=0.4 are compared with the results from PYTHIA-8 [14] and the comparison along with the ratio is shown in Fig.4.33. PYTHIA-8 is widely used for generation of events in high-energy collisions implementing the multiparticle production in collisions between elementary particles via hard interactions in e^+e^-, pp and ep collisions. This model explains different aspects of the pp collision data quite well. The results show that the data are agreement with PYTHIA-8 except the lowest bins having large error bars & the deviation is upto 20% [3].

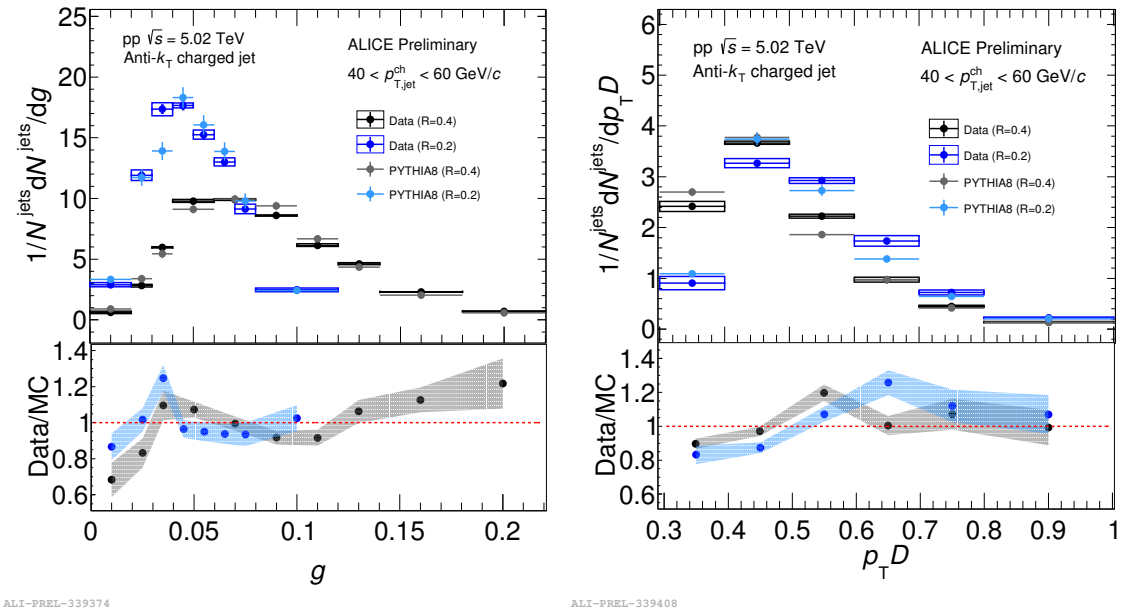

Figure 4.33: jet shape distributions in pp collisions for R=0.2 and 0.4 in jet p_T range of 40-60 GeV/c and comparison with Pythia-8 model

4.14.4 Summary

In this thesis, we have analyzed data collected by the ALICE collaboration in minimum bias pp collisions at $\sqrt{s}$= 5.02 TeV. Three jet-shape observables are studied in detail, namely, angularity(g), dispersion($p_T D$) and LeSub which describe the internal properties of jets. Measurements of jets in pp collisions provide baseline for the study of medium modifications of different jet observables in heavy ion collisions. The underlying events are assumed to have no significant contributions on the results, so UE subtraction has not been done. After suitable event and track selection, we have reconstructed charged-jets using $anti-k_T$ algorithm with various radius parameter i.e. R=0.2, 0.4 & 0.7. Increasing jet radius includes more jet constituents and would be more useful in AA collisions for studing energy loss. The raw shape distributions have been unfolded using Bayesian method to obtain the expected true shapes and the unfolded results are presented. The unfolding is checked by refolding the solutions back and comparing with the raw distributions. The stability of the unfolding process has been validated through Monte Carlo closure test where the ratio of the unfolded to true shapes are observed for all the shapes and p_T^{jet}. The difference is found to be within 5% for iteration 4 and for p_T^{jet} = 40-60 GeV/c with R=0.2 and 0.4. A significant deviation is observed for p_T^{jet} 20-40 GeV/c which needs further detailed investigation. Also the results for R=0.7 are to be checked in details. After unfolding, the bins may be correlated with each other. A strong correlation or anti-correlation among the neighbouring bins will result in a distribution far from the true one. Therefore it is necessary to ensure that there is mild or no correlation among the neighbouring bins. For this Pearson coefficients are estimated and it is found that the value is almost 0 for all bins except the diagonal ones which ensures a proper unfolding.

Statistical and systematic errors are then estimated. The variation in the shape variables with respect to the change in parameters like tracking efficiency, number of iterations, minimum jet p_T and others and the results are shown. The largest contribution to the systematic uncertainty

comes from the tracking efficiency in all three shapes. The results are also compared with the results from model PYTHIA-8 and the difference between data and model is found to be within 20% which is reasonable as obtained in previous studies. The final corrected distributions of the three shape variables have been studied at different R & p_T ranges. It is seen clearly that at higher R, the jets are formed to have broadened. No significant energy dependence has beeb observed when compared to the pp results at 7 TeV.

For future study, the results with p_T^{jet} 20-40 GeV/c and 60-80 GeV/c will be studied in detail and the results for R=0.7 will be checked with proper underlying events subtraction. Also, this study can be expanded to Pb-Pb collisions at same energy to see the changes in jet substructures due to medium modifications.

Bibliography

[1] S. Acharya *et al.* [ALICE], JHEP **04** (2020), 192 doi:10.1007/JHEP04(2020)192 [arXiv:1910.14400 [nucl-ex]].

[2] S. Acharya *et al.* [ALICE], Phys. Lett. B **802** (2020), 135227 doi:10.1016/j.physletb.2020.135227 [arXiv:1905.02512 [nucl-ex]].

[3] S. Acharya *et al.* [ALICE], JHEP **10** (2018), 139 doi:10.1007/JHEP10(2018)139 [arXiv:1807.06854 [nucl-ex]].

[4] Cacciari, M., J. Rojo, G. P. Salam, and G. Soyez (2011),Eur.Phys.J.C71, 1539.

[5] Cacciari, M., G. P. Salam, and G. Soyez (2008a), JHEP04,063.

[6] Cacciari, M., G. P. Salam, and G. Soyez (2008b), JHEP0804, 005.

[7] Cacciari, M., G. P. Salam, and G. Soyez (2012), Eur.Phys.J.C72, 1896.

[8] Salam, G. P. (2010), Eur.Phys.J.C67, 637.

[9] M. Connors, C. Nattrass, R. Reed and S. Salur, Rev. Mod. Phys. **90** (2018), 025005 doi:10.1103/RevModPhys.90.025005 [arXiv:1705.01974 [nucl-ex]].

[10] L. Cunqueiro [ALICE], Nucl. Phys. A **956** (2016), 593-596 doi:10.1016/j.nuclphysa.2016.02.060 [arXiv:1512.07882 [nucl-ex]].

[11] D'Agostini, G. (1995), Nucl. Instrum. Meth.A362, 487.

[12] https://gitlab.cern.ch/RooUnfold/RooUnfold

[13] http://cds.cern.ch/record/2670532/files/CERN-THESIS-2018-390.pdf?version=1

[14] T. Sjostrand, S. Mrenna and P. Z. Skands, Comput. Phys. Commun. **178** (2008), 852-867 doi:10.1016/j.cpc.2008.01.036 [arXiv:0710.3820 [hep-ph]].

Chapter 5

Summary and discussions

The Quark Gluon Plasma, the deconfined state of the strongly interacting matter is formed by creating regions of high energy density by colliding heavy nuclei. One of the signals of QGP formation is the modification of jet properties in heavy ion collision with respect to the properties in pp collisions. The high p_T partons fragment into a collimated shower of correlated particles in a conical volume called Jets. Jet-shapes or jet-substructures are the observables that probe the properties of the QGP medium and helps to understand the intra-jet broadening or collimation as a result of jet quenching. The substructures are expected to be modified in heavy ion collisions relative to the substructures in pp collisions. Measurement of jets in proton-proton collisions provides the baseline for the heavy-ion studies like the modification in jet structures and in the production rates in heavy-ion collisions through the medium interaction.

In this thesis, We have studied the substructure of charged jet in p+p collisions at $\sqrt{s_{NN}}$ = 5.02 TeV with the ALICE experiment at CERN. Charged particle components of jets have been measured using the Time Projection Chamber (TPC) and the Inner Tracking System (ITS). FastJet package has been used to use the the final state particles to obtain the inital parton information i.e jet finding. I have used $Anti - K_T$ algorithm to reconstruct jets with resolution parameter R=0.2,

0.4 & 0.7. Minimum track p_T of 0.15 GeV/c and $|\eta|$ <0.9 have been selected as constituents cut and jet acceptance is considered as $|\eta| < 0.7$ for R=0.2 and $|\eta| < 0.5$ for R=0.4. I have studied three jet shape observables viz Angularity (g), Dispersion ($p_T D$) and LeSub in this analysis. The angularity measures the radial energy profile of the jet i.e. it signifies whether jets are collimated or broadened. The dispersion tells how hard or soft the fragmentation is and LeSub describes the hardest splitting, therefore it should not be sensitive to the background.

The resolution parameter for a conical jet in a jet finding algorithm represents the radius of a jet and it is defined by, $R = \sqrt{\Delta\phi^2 + \Delta\eta^2}$, where $\Delta\phi$ and $\Delta\eta$ are the distances of the particle from the jet axis in ϕ and η. Raw distributions of the jet shape variables have been studied for R=0.2 and R=0.4. At higher jet p_T, jets are found to be collimated for $R = 0.2$. It has been seen that when the jet radius is increased, jets are broadened for a particular jet p_T. For a comparison to the theoretical calculations or other measurements, two dimensional Bayesian unfolding has been used to remove the detector effects on the jet shape variables and to get the corrected observables. To unfold the shape variables, a 4D response matrix has been constructed using input from PYTHIA-8. The correlation between the shape variables at the particle and the detector level has been studied. After that, the jet shape resolution has also been obtained for the three observables. When the unfolded solutions for different iterations are compared to the raw distribution, it has been seen that the unfolding changes the shape significantly and solution converges above four iterations. The stability of the unfolding is then checked by refolding the solution back and checking its agreement with the raw distribution. To test the stability of the unfolding procedure, a closure test has also been performed where, the unfolding input is filled with the Monte Carlo(MC) information. The MC which is used to fill the input is expected to be statistically independent from the sample that is used to fill the response (typically input contains 3% and response 97% of the MC sample). The performance is validated from the ratio of the

unfolded solution to the true MC. The systematic errors are then estimated for different sources and added in quadrature. Finally, the fully corrected results have been shown along with model comparison. The results have indicated that the angularity distribution gets broader for R=0.4 in comparison to that for R=0.2 and the peak shifts towards higher value, whereas, the dispersion slightly shifts towards left for R=0.4 which indicates jet-broadening at higher radius and the small radius jets are fragmented harder at particular jet p_t.

Next, I have studied the medium modified jet shape observables in Pb-Pb collisions at $\sqrt{s_{NN}}$=2.76 TeV using EPOS-3 and JEWEL event generators. I have investigated the in-medium modification to the two jet shape observables viz, the differential jet shape ($\rho(r)$) and the angularity (g) in the most central Pb-Pb collisions at 2.76 TeV using two commonly used event generators JEWEL (recoil OFF) and EPOS-3 in the jet-p_T range of 20-40 GeV/c. A comparison between the results from these models shows that while JEWEL (recoil OFF) does not explain the distribution of lost energy at higher radii with respect to the jet-axis, EPOS-3 explains the effect quite well. However, in EPOS-3, the implemented partonic energy loss mechanism and secondary hard-soft interactions during hadronization and hadronic cascade phase are different from the conventional jet energy loss models.

As an outlook, it is important the studies are made on these observables in heavy ion collisions where background plays a prominent role and innovative methods are to be applied to remove the background. These measurements if performed in heavy ion collisions will help to understand the energy loss mechanism in the medium, the modifications of the fragmentation functions and the energy flow inside the jet cone. This will also help to understand the medium properties in detail.